UCLA
UCLA Electronic Theses and Dissertations

Title
Characterization of Erythroferrone Structural Domains Relevant to Iron-Regulatory Function

Permalink
https://escholarship.org/uc/item/5m86964s

Author
Srole, Daniel Nathan

Publication Date
2023

Peer reviewed|Thesis/dissertation

eScholarship.org Powered by the California Digital Library
University of California

UNIVERSITY OF CALIFORNIA

Los Angeles

Characterization of Erythroferrone Structural Domains Relevant to Iron-Regulatory Function

A dissertation submitted in the partial satisfaction of the requirements

for the degree Doctor of Philosophy in Molecular and Medical Pharmacology

by

Daniel Nathan Srole

2023

© Copyright by

Daniel Nathan Srole

2023

ABSTRACT OF THE DISSERTATION

Characterization of Erythroferrone Structural Domains

Relevant to Iron-Regulatory Function

by

Daniel Nathan Srole

Doctor of Philosophy in Molecular and Medical Pharmacology

University of California, Los Angeles, 2023

Professor Tomas Ganz, Chair

Iron is an essential micronutrient required for hemoglobin synthesis and for the maturation of red blood cells in the bone marrow. Disorders of iron delivery cause both anemia and iron-overload toxicities, depending on the nature of the condition. Erythroferrone (ERFE) is a marrow-derived hormone that coordinates the availability of iron for developing erythrocytes. ERFE acts by suppressing hepatic production of the iron regulator hepcidin, thereby making iron from body stores and from the diet accessible for use by erythroblasts. Suppression of hepcidin by ERFE is thought to be mediated by the sequestration of bone morphogenetic proteins (BMPs) that function

through the SMAD pathway to activate hepcidin transcription, but further mechanistic details are poorly understood. Here, we present a systematic structure-function study of ERFE, elucidating how its structural domains enable its important biological function. We identify multiple conserved domains of the protein and use biophysical, biochemical, and computational modeling techniques to explain the interaction between ERFE and BMPs, thereby illuminating its noteworthy mechanism of action.

The dissertation of Daniel Nathan Srole is approved.

Harley I Kornblum

Nicolaos J Palaskas

Elizabeta Nemeth

Tomas Ganz, Committee Chair

University of California, Los Angeles

2023

DEDICATION

For my dad Russ Srole, who has read books, watched presentations, and spent many hours on Wikipedia all to have sincere, informed conversations with me about my work. Answering your questions has been a genuine highlight of my experience.

PREFACE

This dissertation was supported in part by NIH grant awards (R01) and a Predoctoral Fellowship (TL1 & U2C). Specific author contributions are indicated in each Chapter. The Chapters listed below are reprints or versions of published or submitted manuscripts, reproduced with permission:

Chapter 1 is a reprint of:

Srole DN, Ganz T. Erythroferrone structure, function, and physiology: Iron homeostasis and beyond. *J Cell Physiol* 2021;**236**:4888–901. https://doi.org/10.1002/jcp.30247.

Chapter 2 is a version of:

Srole DN, Jung G, Waring AJ, Nemeth E, and Ganz T. Characterization of erythroferrone structural domains relevant to its iron-regulatory function. *Journal of Biological Chemistry*. In revision.

Chapter 3 is a reprint of:

Fisher AL, **Srole DN**, Palaskas NJ, Meriwether D, Reddy ST, Ganz T, *et al.* Iron loading induces cholesterol synthesis and sensitizes endothelial cells to TNFα-mediated apoptosis. *Journal of Biological Chemistry* 2021:101156. https://doi.org/10.1016/j.jbc.2021.101156.

TABLE OF CONTENTS

LIST OF FIGURES AND TABLES

CHAPTER 1

CHAPTER 2

CHAPTER 3

ACKNOWLEDGEMENTS

I would like to thank my advisors Tomas Ganz and Elizabeta Nemeth for a truly uncountable number of kindnesses. I remember during our very first meeting while I was exploring rotation labs how you focused my interests and experiences at the center of our discussions. This consideration continued for years into the planning and execution of my projects, and it never wavered. I appreciate your support to explore science that was interesting to me even when that separated my work significantly from everyone else's in the lab. Whenever someone asks me for advice on how to pick a thesis lab, I tell them that the right one is where they feel comfortable and cared for. I chose the right lab, and I had so many experiences—big and small—that confirmed this for me over almost four years. Thank you.

In recognition of the people who helped set me up for success going into my PhD, I would like to thank my undergraduate lab mentors Jamie Cate, Elizabeth Montabana, and Mia Pulos-Holmes. To Jamie, thank you for taking a chance on a freshman who had only just completed his first semester of college. You allowed me to learn biology in a way that not everyone gets to: by doing it. I might not have continued in research if not for how you integrated me into so many exciting projects. I appreciate how you worked through their difficulties with me, and when all was said and done, how you never missed any of my poster presentations. Not all undergrads have such an involved, caring PI. To Liz, thank you for giving me a remarkably strong foundation in bench skills. My good precision and "wizard-like" cloning skills—a real thing someone said about me—are all thanks to your patient and thorough teaching. You fostered an emphasis in me on understanding the underlying principles of what we do, and it continues to serve

me every day. To Mia, I think that I have multiple eras to thank you for. First, thank you for helping me build on the underpinning that Liz gave me. You taught me, encouraged me, and trusted me to help you with your own work. You never micromanaged or condescended, but rather made me feel like a partner. It's hard to overstate the value of having a buddy. And that brings me to the second era—one of trading stories, jokes, advice, worries, dog toys, and memes. Doing a PhD is a unique and challenging time, and your friendship has been invaluable to me during mine. From what you tell me, this next stage is a thrilling one. I can't wait to keep joking through it with you. Thank you.

Although there are too many to name, I would like to thank my friends. It's no small ask to get excited about someone else's little corner of esoterica. I'd say you kept me motivated through the process quite well, because if you check the page count, you'll see this particular corner doesn't look so little anymore. Specifically, I'd like to recognize the members of my PhD cohort: for being friends from the very first day, for celebrating each other's accomplishments, for making all the other cohorts jealous of how well we click. Additionally, I would like to specifically acknowledge two more friends, Sylvie Dobrota and Johnson Khor, who have watched more of my presentations, read more of my writings, and talked me through more of my setbacks than anyone else during my PhD. It's been exciting to watch as you two go through your own doctoral journeys, and I hope we can always keep Thursday evenings open. Thank you.

Finally, I would like to thank my family. I can't adequately express how much your untiring support has meant to me. To Dad, thank you for always taking my calls to talk through problems, even when you didn't understand all the specifics in play. I will always appreciate your genuine interest in my work and your support as I made my way

through it. I hope that I was able to take something from obscurity and make it at least a little bit interesting. To Hilary, thank you for helping me keep my perspective. It's so easy to get tunnel vision here after years of working on niche projects and problems but talking with you has always helped pull me back out and see the bigger picture. And on a very practical level, I wouldn't know how to advocate for myself half as well as I do without you showing me how. Finally, I would like to acknowledge my mom Betty Srole who didn't get to see me in this chapter of my life, but who was nonetheless my most vocal supporter and would, without question, have continued to be. Thank you.

VITA

EDUCATION

University of California, Los Angeles ***2018-2023 (in progress)***

Doctor of Philosophy (PhD), Molecular and Medical Pharmacology

University of California, Berkeley **2014-2018**

Bachelor of Arts (BA), Molecular and Cell Biology

PUBLICATIONS

Srole DN, Jung G, Waring AJ, Nemeth E, Ganz T. Characterization of erythroferrone structural domains relevant to iron-regulatory function. *Journal of Biological Chemistry.* In revision.

Fisher AL, **Srole DN**, Palaskas NJ, Meriwether D, Reddy ST, Ganz T, *et al.* Iron loading induces cholesterol synthesis and sensitizes endothelial cells to TNFα-mediated apoptosis. *Journal of Biological Chemistry* 2021:101156. https://doi.org/10.1016/j.jbc.2021.101156.

Srole DN, Ganz T. Erythroferrone structure, function, and physiology: Iron homeostasis and beyond. *J Cell Physiol* 2021;**236**:4888–901. https://doi.org/10.1002/jcp.30247.

Pulos-Holmes MC, **Srole DN**, Juarez MG, Lee AS-Y, McSwiggen DT, Ingolia NT, *et al.* Repression of ferritin light chain translation by human eIF3. *ELife* 2019;**8**:e48193. https://doi.org/10.7554/eLife.48193.

SELECT PRESENTATIONS

Srole DN, Nemeth E, Ganz T. (2022). *Characterization of the Erythroferrone Structural Domains Relevant for Its Iron-Regulatory Function*. Oral presentation at the American Society of Hematology, New Orleans, LA. **Abstract Achievement Award winner. Best of ASH nominee.**

Srole DN, Nemeth E, Ganz T. (2022). *A Structure-Function Study of the Iron-Regulatory Hormone Erythroferrone*. UCLA Department of Pharmacology retreat, Santa Monica, CA. **First place oral presentation.**

HONORS, AWARDS, AND EXTRACURRICULAR ACTIVITIES

NIH NIDDK Pre-Doctoral Fellowship in Kidney, Urology, and Hematology **2022—2023**
(TL1 DK132768 and U2C DK129496)

American Society of Hematology Abstract Achievement Award. New Orleans, LA **2022**

First place oral presentation, UCLA Department of Molecular and Medical **2022**
Pharmacology Annual Retreat. Santa Monica, CA

Department of Molecular and Medical Pharmacology student representative **2021**

Chapter 1

Erythroferrone Structure, Function, and Physiology:

Iron Homeostasis and Beyond

The contents of this chapter were originally published in the Journal of Cellular Physiology on December 28, 2020.

Srole DN, Ganz T. Erythroferrone structure, function, and physiology: Iron homeostasis and beyond. *J Cell Physiol* 2021;**236**:4888–901. https://doi.org/10.1002/jcp.30247.

Abstract

Erythroferrone (ERFE) is the main erythroid regulator of hepcidin, the homeostatic hormone controlling plasma iron levels and total body iron. When the release of erythropoietin from the kidney stimulates the production of new red blood cells, it also increases the synthesis of ERFE in bone marrow erythroblasts. Increased ERFE then suppresses hepcidin synthesis, thereby mobilizing cellular iron stores for use in heme and hemoglobin synthesis. Recent mechanistic studies have shown that ERFE suppresses hepcidin transcription by inhibiting bone morphogenetic protein signaling in hepatocytes. In ineffective erythropoiesis, pathological overproduction of ERFE by an expanded population of erythroblasts suppresses hepcidin and causes iron overload, even in non-transfused patients. ERFE may be a useful biomarker of ineffective erythropoiesis and an attractive target for treating its systemic effects.

1. Erythropoiesis and iron homeostasis—an overview

1.1 Iron homeostasis

Iron is an essential micronutrient for nearly all living organisms because of its important role in catalyzing redox reactions and the transport and storage of oxygen. Many organisms with circulatory systems use myoglobin to store oxygen reserves in skeletal muscle and hemoglobin to deliver oxygen to all body tissues. In both myoglobin and hemoglobin, oxygen binds to an iron atom at the center of heme groups. Total iron content in healthy human adults is 3-4 g, of which more than half is found in hemoglobin of erythrocytes. Macrophages continuously recycle iron from old erythrocytes and other senescent cells, returning it to a dynamic plasma iron pool. Conservation effectively limits iron losses to a tiny fraction of the total content (~1 mg/day) in children, men, and post-menopausal women. Pregnant, lactating, and menstruating women experience increased iron loss due to the iron demands of these physiological processes. Non-heme iron is transported through plasma bound to transferrin protein which constrains the propensity of iron to catalyze the generation of reactive oxygen species. Once imported into cells through transferrin receptors, iron is stored within ferritin. Most cellular iron stores are located in the liver and spleen.

Tight regulation of iron flows ensures that iron is available to developing red blood cells while avoiding the potential toxicity of excess extracellular iron, and limiting its availability to infectious microorganisms. The body's iron traffic is controlled by hepcidin, the sole homeostatic hormone responsible for regulating both plasma iron levels and the total iron content of the body. The 25 amino acid peptide is produced in the liver in proportion to plasma iron concentrations and hepatic iron stores. When iron is abundant, high concentrations of hepcidin bind the cellular iron exporter ferroportin, causing its occlusion, internalization (Nemeth 2004), and degradation. Intestinal absorption of dietary iron and iron

release from cellular stores are thereby inhibited. When plasma iron is scarce, hepatic hepcidin secretion is low which allows ferroportin to export iron to plasma, thereby stimulating intestinal iron absorption and mobilization of cellular stores.

1.2 Erythropoiesis and its interaction with iron homeostasis

The intensely energy-consuming renal medulla effectively monitors oxygen delivery by blood, determines its hemoglobin content, the amount of oxygen bound to hemoglobin, and the dissociation of oxygen from hemoglobin. When oxygen delivery to this tissue does not meet demand, interstitial fibroblasts sense hypoxia and begin producing and excreting erythropoietin (EPO) whose synthesis is transcriptionally regulated by hypoxia-inducible factor 2 (HIF-2). Erythroid precursors in the bone marrow respond to EPO signaling by cell division and differentiation towards mature erythrocytes. Hemoglobin synthesis in the developing erythrocytes requires iron-containing heme. Iron-deficiency inhibits the production of heme and hemoglobin, as well as the production and maturation of erythrocytes.

Erythropoiesis even at baseline consumes most of the iron flowing into the plasma compartment. Stimulation of erythropoiesis, by blood loss, hypoxia, or injection of exogenous erythropoietin strongly suppresses the production of hepatic hepcidin in mice and humans, allowing more dietary iron and iron from stores to enter blood plasma for heme and hemoglobin synthesis by developing erythrocytes in the marrow (**Figure 1, A-B**). Arguing from clinical observations and experimental models, investigators in the last century proposed that an erythroid regulator strongly influences iron homeostasis. After the discovery of hepcidin as an iron-regulatory hormone, it became clear that the erythroid

regulator does not directly affect iron transport but rather acts by suppressing hepcidin. Although erythropoietin itself was a reasonable candidate for a hepcidin suppressor, *in vitro* studies showed that EPO does not directly suppress hepcidin in isolated liver cells (Gammella et al. 2015) implying the existence of an intermediary EPO-responsive suppressor of hepcidin.

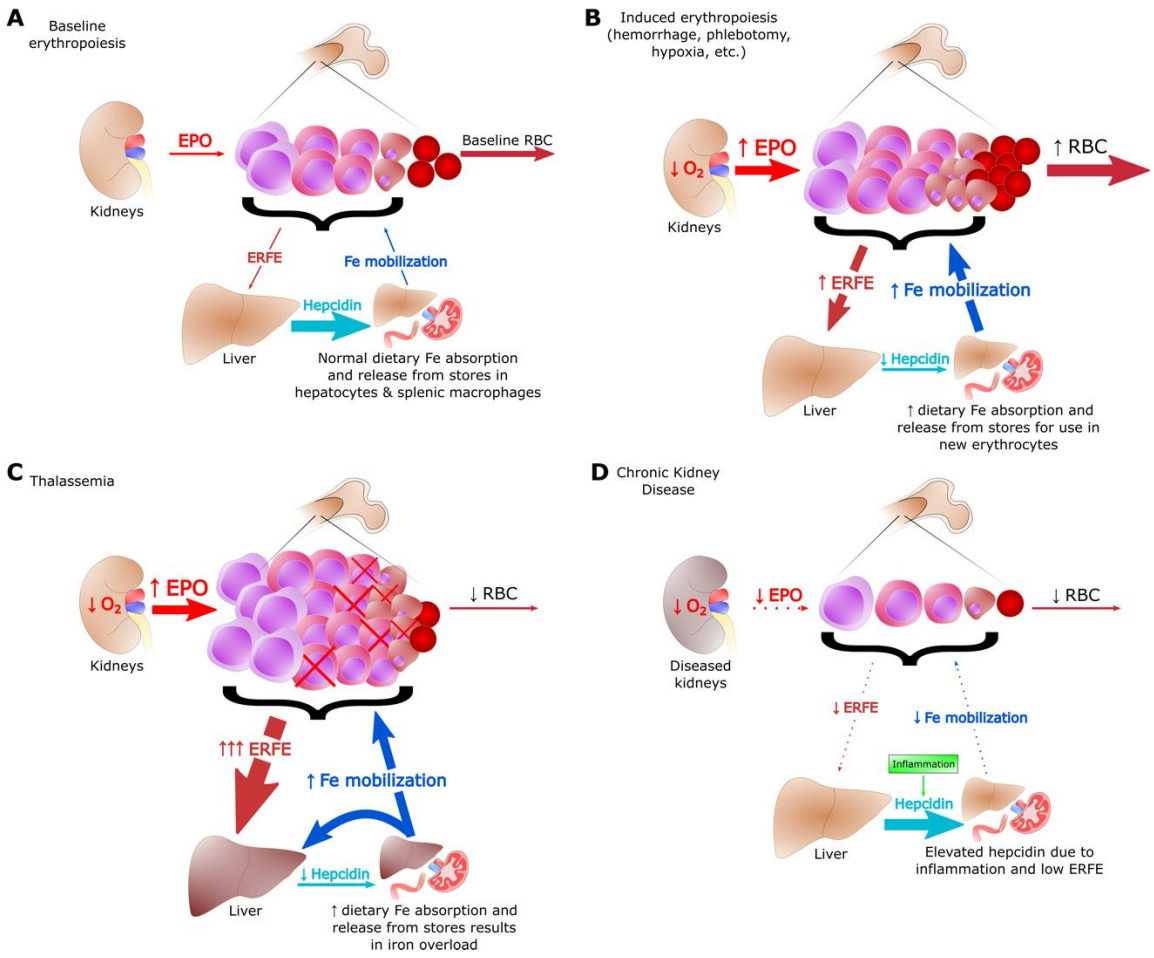

Figure 1. Effective and Ineffective Erythropoiesis

(A) Baseline erythropoiesis generates red blood cells to replace old and damaged cells. Physiological levels of ERFE and hepcidin at baseline provide sufficient iron for steady state production of erythrocytes. (B) When the kidneys sense cellular hypoxia, they secrete EPO which stimulates erythropoiesis and the production of ERFE. As ERFE suppresses hepcidin, iron is mobilized from stores for use by the expanded population of maturing red blood cells. (C) In β-thalassemia, most erythroblasts do not generate mature erythrocytes, causing anemia and tissue hypoxia. This results in high levels of EPO and ERFE, chronically low hepcidin, and iron overload. (D) In chronic kidney disease, low EPO production, low clearance of hepcidin by the kidney, and inflammation can lead to low iron availability in the erythroid system.

2. The Erythroferrone Molecule

2.1 Discovery of Erythroferrone

Motivated by evidence that hepcidin expression is influenced by erythropoietic activity (Pak et al. 2006; Vokurka et al. 2006), a search was performed for mRNAs encoding secreted proteins that were induced in mouse bone marrow within hours after blood loss (Kautz et al. 2014). A transcript identified at the time as *Fam132b* and since renamed *Erfe* was induced shortly before hepcidin suppression and sustained its high expression for 24-48 hours, mirroring serum EPO concentrations. EPO injections resulted in a similar but faster increase in *Erfe* expression indicating that its gene product may be directly EPO-inducible. qPCR analysis revealed EPO-stimulated bone marrow, and specifically erythroblasts, to be the highest ERFE-expressing cell type. Though the erythroferrone protein had been catalogued previously under the names CTRP15 and myonectin (Seldin, Tan, and Wong 2014), its prominent role in the regulation of hepcidin and iron homeostasis was a novel finding. ERFE met the criteria for the putative erythroid regulator of iron homeostasis that could explain the observed iron-regulatory responses to anemia, hemorrhage, hypoxia, and disorders of ineffective erythropoiesis including β-thalassemia and myelodysplastic syndromes (**Figure 1, C-D**). The development of an immunoassay for serum ERFE (Ganz et al. 2017) allowed for the analysis of ERFE in patients with these diseases, as discussed below. In a short time, the measurement of ERFE levels has become a common research tool for studies of the pathophysiology of anemias and other erythroid disorders.

2.1.1 Human Erythroferrone Immunoassay

In 2017, a rabbit monoclonal antibody-based sandwich immunoassay test was developed for the detection of serum ERFE from human clinical samples (Ganz et al. 2017). The immunoassay was validated using blood samples taken from three sets of human volunteers:

healthy adult males, EPO-treated geriatric patients with anemia, and β-thalassemic patients (both non-transfused and transfusion-dependent). ERFE levels detected by the assay rose in the healthy volunteers after phlebotomy with a matching decline in serum hepcidin levels as confirmation. The EPO-treated patients likewise manifested the expected changes in their ERFE and hepcidin values. ERFE concentrations in non-transfused and pre-transfused β-thalassemia patients were elevated relative to normal samples, as expected, and levels were much lower post-transfusion. These data recapitulated the expected trends for ERFE concentrations in each population and were validated by inverse correlations with serum hepcidin. A similar validated human ERFE immunoassay using mouse monoclonal antibodies targeted to the same antigen is available commercially (Intrinsic LifeSciences, La Jolla, CA).

2.1.2 Mouse Erythroferrone Immunoassay

Another ELISA using mouse monoclonal antibodies was developed by Silarus Therapeutics for the detection of murine ERFE. We modified the assay to increase its sensitivity by employing the DELFIA reporter system instead of the conventional horse-radish peroxidase-based colorimetric readout. Another ELISA for murine ERFE, making use of polyclonal antibodies against mouse ERFE, is commercially available (Intrinsic LifeSciences). Using this assay, ERFE levels are below the threshold of detection in healthy male C57BL/6 mice, but mice with the $Hbb^{th3/+}$ model of β-thalassemia have elevated and detectable ERFE levels (Gutschow et al. 2019). A number of other ERFE ELISA kits are also marketed but should be viewed with caution unless supported by peer-reviewed validation data.

A

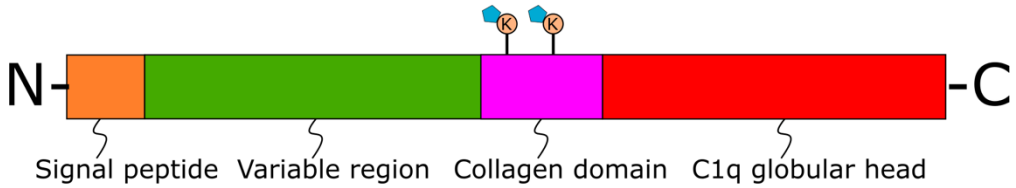
N-
-C
K
K
Signal peptide
Variable region
Collagen domain
C1q globular head

B

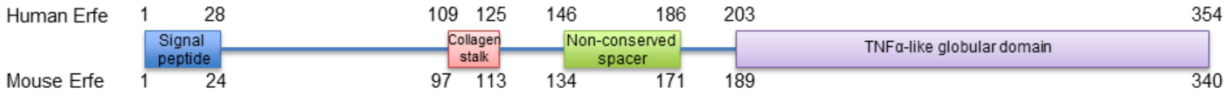
Human Erfe
1
28
109
125
146
186
203
354
Signal peptide
Collagen stalk
Non-conserved spacer
TNFα-like globular domain
Mouse Erfe
1
24
97
113
134
171
189
340

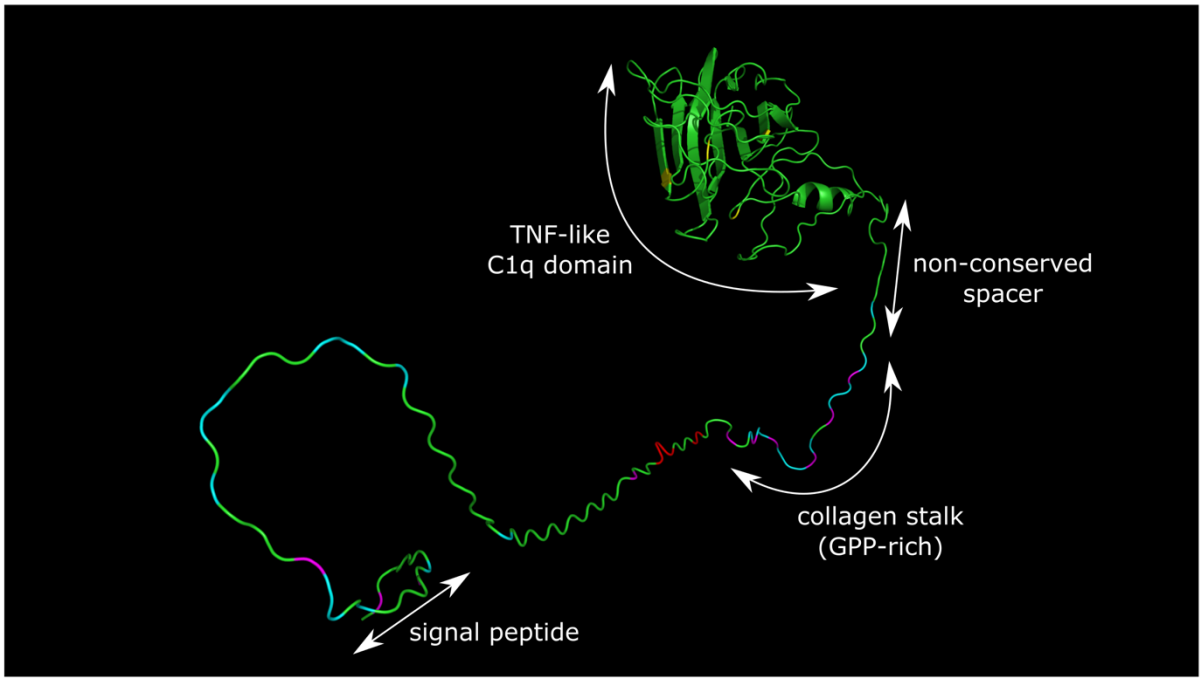
TNF-like C1q domain
non-conserved spacer
collagen stalk (GPP-rich)
signal peptide

C

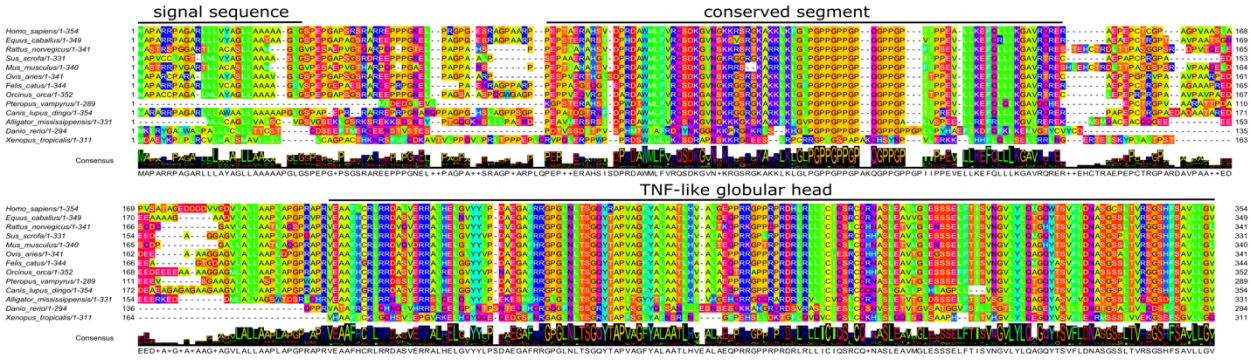
signal sequence
conserved segment
TNF-like globular head
Homo_sapiens/1-354
Equus_caballus/1-349
Rattus_norvegicus/1-341
Sus_scrofa/1-331
Mus_musculus/1-340
Ovis_aries/1-341
Felis_catus/1-344
Orcinus_orca/1-352
Pteropus_vampyrus/1-289
Canis_lupus_dingo/1-354
Alligator_mississippensis/1-331
Danio_rerio/1-294
Xenopus_tropicalis/1-311
Consensus

Figure 2. CTRP and ERFE Structure

(A) Generalized domain structure of CTRPs. The signal peptide directs the protein for secretion and is removed in the final form. The variable region is the least conserved domain between CTRP family members. The collagen domain is glycine- and proline-rich and may contain glycosylated lysine residues known to promote multimerization (e.g. adiponectin). The C1q globular head is predicted to be the most structured part of the protein and is highly conserved between CTRP family members. (B) Human and murine erythroferrone domains and prediction of folded structure. (C) Erythroferrone sequence alignment across vertebrate species highlighting the conserved segments.

2.2 The C1q/TNF-Related Protein (CTRP) Family

Erythroferrone belongs to the C1q/TNF-Related Protein (CTRP) family of structurally related, secreted hormones found in all vertebrate organisms. The 16 identified CTRP proteins share structural similarities and 4 distinct domains: an N-terminal signal peptide directing the protein for secretion, a variable region that differentiates each member, a collagenous linker with Gly-X-Y repeats, and finally a C-terminal globular head with homology to complement factor C1q and the TNFα family of cytokines (Wong et al. 2004) (**Figure 2A**). Gene expression profiling shows that some CTRPs are preferentially produced in certain tissue types. Adiponectin, the most extensively studied member of this family, is expressed highly and nearly exclusively in adipose tissues. CTRP6, CTRP12, and ERFE likewise have similarly restricted expression in the placenta, small intestine, and erythropoietic bone marrow, respectively. Early attempts to characterize the proteins of this large family have focused on their metabolic effects and potential to function as inter-organ communicators (Schäffler and Buechler 2012; Seldin et al. 2014). Adiponectin has held special interest for decades, with numerous studies that continue to elaborate its roles in insulin resistance, dyslipidemia, and atherosclerosis (Yadav et al. 2013). Some of adiponectin's metabolic functions are believed to be mediated by its various oligomerized forms. The protein can exist as a trimer, hexamer, and the high molecular weight 18-mer and 30-mer species in some organisms. Functional data show differing and sometimes opposing biological effects of adiponectin depending on the oligomer type, with the higher molecular weight species thought to be the most metabolically active (Wang et al. 2008). The ability of adiponectin to multimerize is dependent on interactions in the collagenous domain, specifically between conserved lysine residues, and their post-translational modifications (PTMs). Bacterially-derived adiponectin can form trimeric and hexameric structures, but the lack of PTMs prevents higher order oligomerization. The formation of these high molecular weight species from mammalian cells can be disrupted by de-glycosylation of the key lysine residues or mutation of these lysines to other amino acids. The presence and conservation of the

collagenous domain in all CTRPs suggests that multimerization is likely relevant for the native structures and biological functions of all family members. The varied expression patterns of CTRP members suggest that they mediate communication among distinct organ systems. Mechanisms for CTRP action are currently a topic of active research, and there are as of yet no known cell surface receptors that mediate their physiological functions, with the exception of adiponectin receptors AdipoR1 and AdipoR2 (Yamauchi et al. 2003).

2.3 Erythroferrone Structure and Properties

Like other CTRPs, ERFE has a 4-domain structure with a unique N-terminus and significant sequence homology to other family members at the C-terminus. The full-length human and mouse proteins are composed of 354 and 340 amino acids, respectively, and have predicted masses of 37.3 kDa and 36.3 kDa. The glycosylation of one (human) or two (mouse) asparagine residue(s) (Blom et al. 2004) coupled with co-translational removal of the signal peptides all contribute to an apparent weight of 35-40 kDa as determined by reducing SDS-PAGE electrophoresis. The globular C-terminal domain is predicted to fold into the highly structured TNF/C1q head while the N-terminus of the molecule is expected to have an extended and flexible secondary structure (**Figure 2B**). In addition to the globular head, the short proline-rich collagenous linker connecting the two larger domains is thought to promote multimerization of the protein as is seen in the native, oligomerized forms of adiponectin (Wang et al. 2008), but lacks the lysines that are thought to facilitate higher order multimer assembly. Because it contains two predicted PCSK3/furin recognition sites, ERFE may exist as multiple cleaved isoforms after protein processing. Little is currently understood about multimerization or the regulation and differential function of the cleaved forms.

2.4 Evolutionary Analysis of Erythroferrone

ERFE is encoded in the genomes of all vertebrates, indicating its importance to the physiology of so many forms of life. Amino acid sequence alignment reveals a striking conservation across species, down to and including *Xenopus tropicalis* (**Figure 2C**). Beyond the N-terminal signal sequence that directs each ERFE ortholog for secretion, there is a stretch of nearly 100 amino acid residues with high levels of conservation in both charge and polarity. These conserved regions include hydrophobic stretches, positively charged patches, and the remarkably preserved glycine/proline-rich collagen linker which could all be integral to ERFE's cellular function. The C-terminal TNF domain is the most highly conserved region across species but unexpectedly, functional evidence rules this region out as the primary mediator of ERFE's effect on hepcidin.

2.5 Erythroferrone Mechanism of Action

When plasma iron concentrations and liver iron stores are high, hepcidin synthesis is induced by bone morphogenetic protein activation of the Smad1/5/8 pathway, predominantly through binding of the BMP2/6 heterodimer to the heterotetrameric BMP receptor (Wang et al. 2020). Although technical limitations may interfere with the detection of the active phosphorylated forms of Smad1/5/8 *in vivo*, the weight of evidence indicates that erythroferrone potently suppresses this induction both *in vivo* and in Hep3B *in vitro* cell systems (Wang et al. 2017:5). Various molecular mechanisms for this suppression have been postulated including signaling by dedicated ERFE receptors and interaction with the negative BMP regulator matripase-2 (Arezes et al. 2018; Aschemeyer et al. 2017). Matripase-2, expressed from the *TMPRSS6* gene, is a serine protease that cleaves the membrane-bound form of the positive hepcidin regulator hemojuvelin—and likely also other proteins in the iron-regulatory complex—thereby suppressing hepcidin transcription. Matripase-2 was therefore a reasonable candidate to consider as part of

the ERFE mechanism of action, as *Tmprss6* KO mice did not suppress hepcidin in response to a single injection of EPO despite having an appropriate increase in *Erfe* mRNA after EPO administration (Nai et al. 2016). However, experiments with primary hepatocytes isolated from *Tmprss6* KO mice have demonstrated that erythroferrone and matripase-2 regulate hepcidin independently of one another (Aschemeyer et al. 2017). These results showed that while ablation of matripase-2 increases hepcidin expression overall, ERFE still suppresses hepcidin transcription by the same relative amount as in primary hepatocytes from WT mice.

Recent data have provided unexpected but well-founded evidence for ERFE's action as a novel BMP trap that diminishes hepcidin expression by sequestering BMP ligands away from their cell surface receptors (Arezes et al. 2018), specifically ALK3 (Wang et al. 2020:3) (**Figure 3**). Surface plasmon resonance (SPR) studies confirm the ability of ERFE to bind BMPs. The strongest interactions take place between ERFE and the homodimers of BMP2, BMP6, and the BMP2/6 heterodimer (Arezes et al. 2020; Wang et al. 2020). Other previously proposed erythroid regulators of hepcidin, such as the TGFβ-family ligand GDF15 (Kim and Nemeth 2015), lack any binding interaction (Arezes et al. 2020). Our unpublished data on the binding of other CTRPs to BMPs also show varied preference for BMP species between family members, suggesting a general model for how their physiological effects may be carried out. In studies of ERFE truncation mutants, the N-terminal variable region is sufficient to suppress hepcidin expression nearly to the same extent as the WT protein, and the C1q globular domain carries no suppressive activity (Arezes et al. 2020). Moreover, antibodies specifically targeted toward the N-terminus of the protein compete for binding with BMP6, unlike antibodies that target the C-terminus. SPR analysis of ERFE truncation mutants has confirmed the specific binding of BMPs to the N-terminus only. Nevertheless, it is likely that the globular head facilitates the

function of ERFE *in vivo*, perhaps by promoting multimerization, enhancing stability, or in some other manner yet to be elucidated.

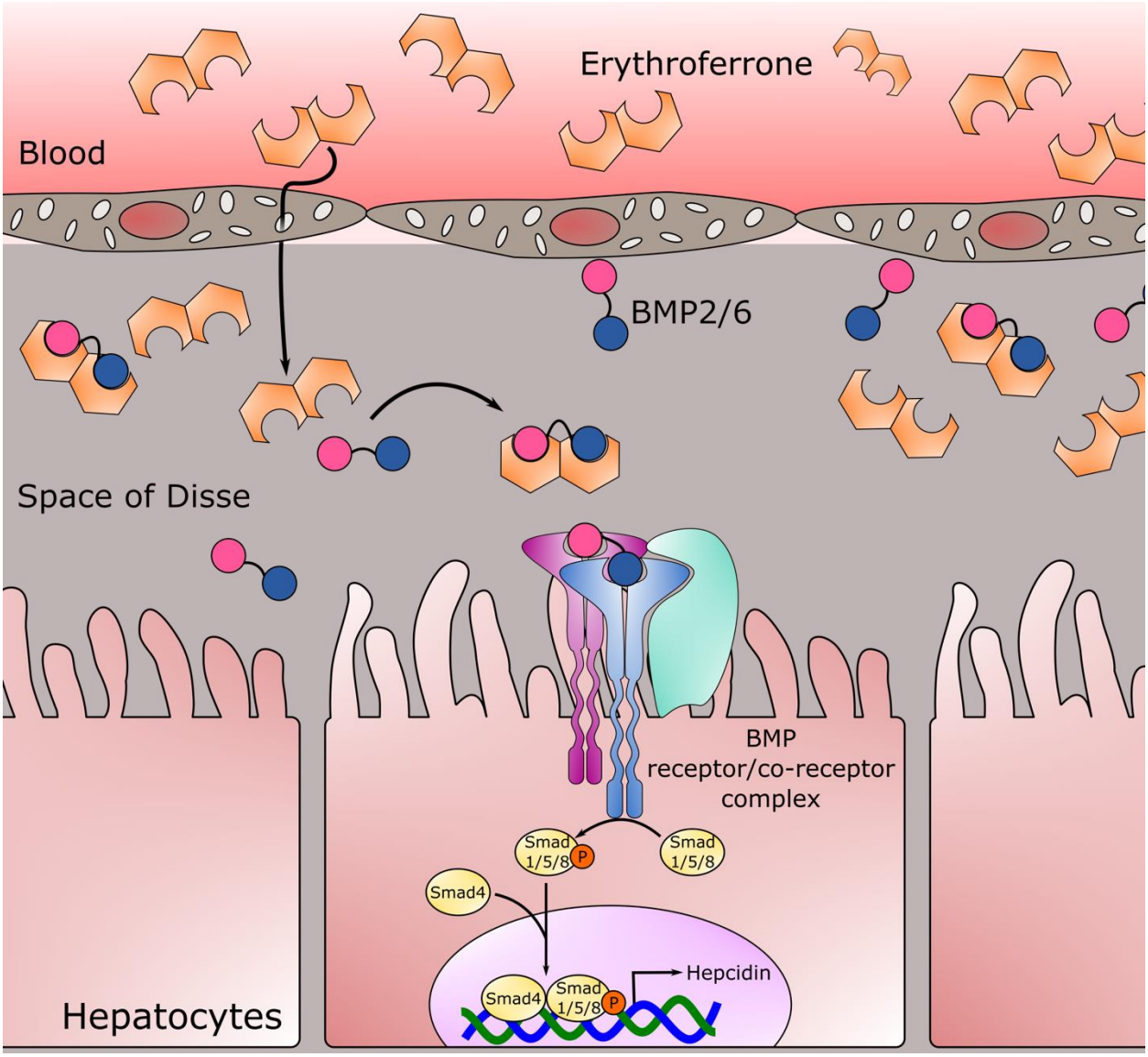

Figure 3. Erythroferrone Mechanism of Action

Erythroferrone molecules secreted into blood by erythroblasts in the marrow reach the liver where they permeate through fenestrations in sinusoidal endothelial cells into the Space of Disse, a perisinusoidal space separating hepatocytes from sinusoidal endothelial cells. Sinusoidal endothelial cells secrete BMP2/6 heterodimers, but ERFE sequesters these before they engage the BMP receptor complex on hepatocytes, lowering activation of the Smad1/5/8 signal transduction pathway, and reducing hepcidin transcription.

3. Erythroferrone Pathophysiology

3.1 Erythroferrone in Baseline and Stress Erythropoiesis

Basal erythropoiesis in the marrow produces red cells at a relatively constant rate to replace old and damaged ones whose iron content is recycled mostly by splenic and hepatic macrophages (**Figure 1A**). Anemia or hypoxia decrease oxygen delivery to tissues, a change sensed as cellular hypoxia by interstitial fibroblasts in the intensely energy-consuming regions of the kidney, and these cells respond by HIF-2 mediated increases in the production of EPO (Haase 2013; Hodges et al. 2007). Elevated plasma EPO concentrations enhance the survival of erythroid precursors, increase the number of erythroblasts, and stimulate those erythroblasts to produce and secrete ERFE, thereby suppressing hepcidin synthesis in the liver. With less hepcidin available to inhibit ferroportin function, iron-exporting cells deliver more cellular iron into plasma. Dietary iron absorption increases, and cellular iron stores are mobilized from macrophages and hepatocytes for heme and hemoglobin synthesis in newly produced red blood cells (**Figure 1B**). Erythroferrone is most important early in the response to erythropoietic stimuli, as *Erfe* knockout mice fail to rapidly suppress hepcidin after acute blood loss or EPO injection. This leads to a delay of several days in their recovery from anemia compared to WT animals (Kautz et al. 2014).

The increased ERFE production in response to anemia has two components: when erythropoietic tissues are stimulated by EPO, the population of erythroid precursor cells expands. Secondly, within this population, each individual cell produces more ERFE. In anemias with ineffective erythropoiesis, the erythroid precursor population is greatly expanded and stimulated by EPO, but most of these cells do not generate mature erythrocytes. These dead-end erythroid precursors secrete high levels of ERFE that chronically suppress hepcidin and thereby cause iron overload. High concentrations of non-transferrin bound iron in these

iron-loading anemias are known to cause tissue injury by catalyzing the formation of reactive oxygen species (**Figure 1C**). Iron toxicity is manifested as cellular damage in hepatocytes, cardiomyocytes, and endocrine glands as well as an increased risk of infection (Vento, Cainelli, and Cesario 2006). To prevent these potentially lethal complications of iron overload, treatment with iron chelators is required to trap and eliminate excess iron through the urinary and gastrointestinal routes.

3.2 Effects of Erythroferrone Loss-of-Function and Over-Expression

Erfe knockout mice that are allowed to develop without external erythropoietic stresses have normal iron and blood parameter phenotypes with the exception of a transient iron-restrictive anemia at around 6 weeks of age (Kautz et al. 2014). This is a period of rapid growth in mice, with expansion of erythrocyte mass and increased iron demand. Lower hemoglobin levels in *Erfe* knockout mice catch up to their WT counterparts by 12 weeks. While ERFE ablation prevents knockout animals from quickly suppressing hepcidin after an acute erythropoietic stimulus as previously mentioned, an appropriate, if delayed, hepcidin response is seen after a prolonged erythropoietic stimulus such as multiple EPO injections (Coffey et al. 2018). The delayed but complete compensation for the lack of ERFE may be due, at least in part, to the depletion of iron stores which itself is a strong negative regulator of hepcidin expression (**Figure 4**). Because differic transferrin is a strong inducer of hepcidin transcription, the transient decrease of diferric transferrin concentrations caused by EPO-inducible expression of transferrin receptor-1 on erythroblasts may contribute to the small initial drop in hepcidin (Mirciov et al. 2018) that is seen even in *Erfe* KO mice, and could synergize with the suppressive effect of ERFE on hepcidin.

In unpublished data, our lab has developed mice that over-express ERFE under control of the β-globin promoter, restricting the secretion of ERFE to erythroid cells. Highly over-expressing strains—with *Erfe* mRNA levels that are 10-fold higher than WT—have suppressed hepcidin levels and thereby develop pathological iron overload. Interestingly, these animals manifest lower body weights and a number of other systemic abnormalities, some of which are also seen in human anemias with ineffective erythropoiesis. We hypothesize that these effects are mediated by the interference of ERFE with BMP signaling during development and growth.

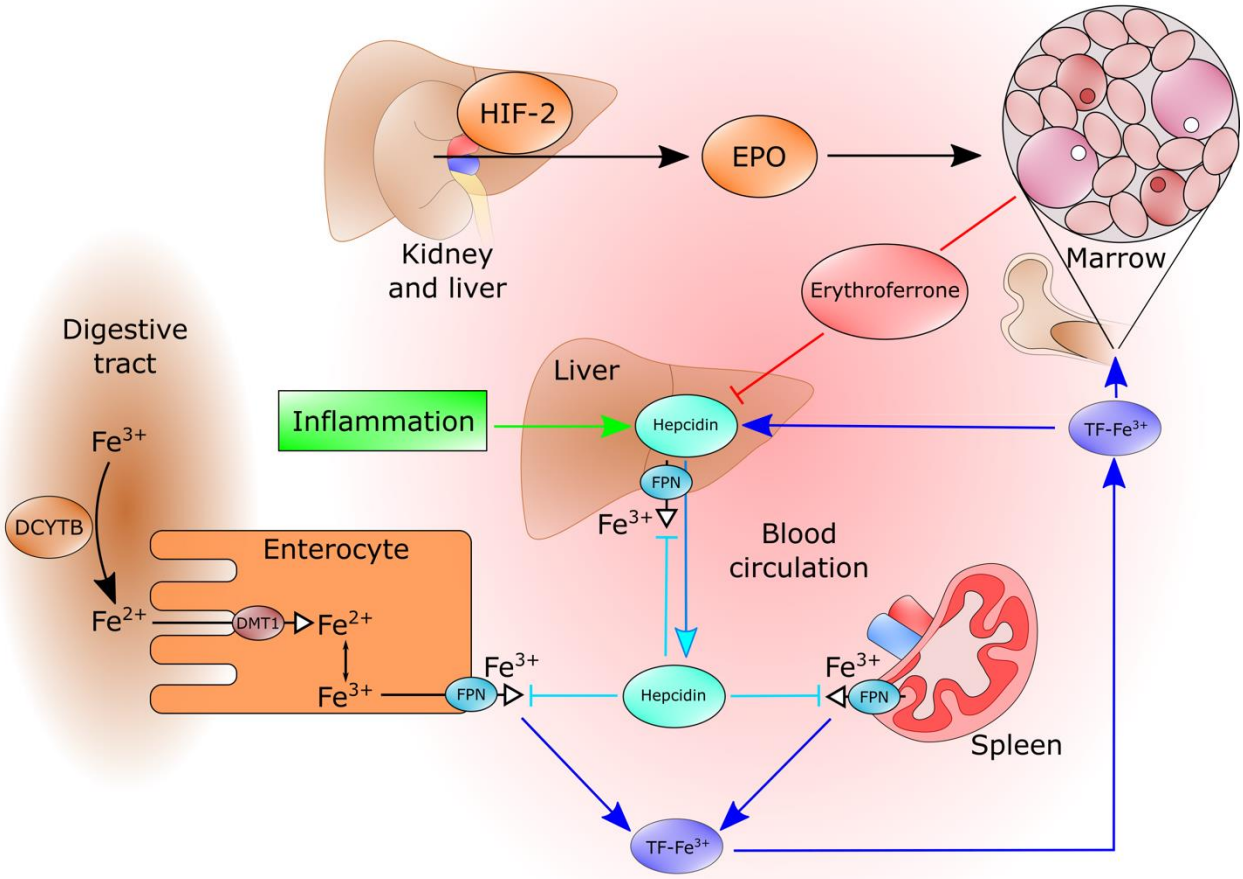

Figure 4. ERFE-Hepcidin-Ferroportin Axis

Interstitial fibroblasts in the kidney and hepatocytes in the liver respond to cellular hypoxia by HIF-2 induced transcription and production of EPO. EPO stimulates the expansion of erythroblasts as well as increasing production of ERFE. ERFE inhibits the transcription of hepatic hepcidin thereby stabilizing the cellular iron exporter ferroportin on the surfaces of hepatocytes and macrophages. Cellular iron stores are then mobilized into plasma to be used for hemoglobin synthesis by the expanded population of maturing erythrocytes.

3.3 The Pathological Role of ERFE in Diseases of Altered Erythropoiesis

The inherited blood disorder β-thalassemia results from mutations in β-globin genes that limit the production of β-globin relative to α-globin, causing an imbalance that decreases erythroblast survival in the marrow and erythrocyte lifespan in blood circulation. Ineffective erythropoiesis is characteristic of β-thalassemia because the erythroblast population becomes greatly expanded but generates relatively few mature erythrocytes. In the most severe cases known as β-thalassemia major, patients require regular blood transfusions in order to survive or to prevent severe systemic complications. Each transfused unit of packed erythrocytes delivers the equivalent of 200-250 mg of iron. With transfusions needed every two to five weeks and physiological iron losses limited to a few mg/day, total body iron will quickly exceed the normal adult endowment of 3-4 g by many-fold. Iron chelation is therefore necessary to prevent the overload that results from transfusion. In the less severe form termed β-thalassemia intermedia, red blood cell production is usually sufficient to avoid regular transfusions, but ineffective erythropoiesis may be as or more severe. This is the case because transfusion therapy for thalassemia major increases oxygenation by increasing the number of functional red blood cells. This lowers erythropoietin production by the kidneys and relieves the stimulus for erythropoiesis (**Figure 1C**).

Several mouse models of anemias—induced genetically, by administration of a hemolytic agent, or through dietary iron deprivation—show increased *Erfe* expression relative to control littermates (Mirciov et al. 2017). Mouse models of anemias with ineffective erythropoiesis would be expected to show particularly high ERFE levels, because in these anemias the erythroblast population, which secretes ERFE, is expanded out of proportion to the severity of anemia. One such model, the $Hbb^{th3/+}$ mouse recapitulates a non-transfusion dependent β-thalassemia with moderately decreased hemoglobin concentrations, markedly lower hepcidin during growth

compared to WT, and increased plasma and hepatic iron concentrations. The model is haploinsufficient for β-globin leading to the precipitation of excess unpaired α-globin chains. ERFE production in the bone marrow and spleens of these mice is increased relative to WT consistently throughout their lives, between 8-fold and 32-fold depending on age (Kautz et al. 2015). The beneficial effect of anti-ERFE-neutralizing antibodies on anemia in this model suggests that excess ERFE contributes not only to iron overload (Kautz et al. 2015) but also to the pathogenesis of anemia in this model (Arezes et al. 2020). Importantly, reticulocyte percentage is decreased with antibody treatment, indicative of increased quality and lifespan of erythrocytes. It remains to be seen if ERFE inhibition for the treatment of human β-thalassemia can decrease iron absorption and iron deposition in organs sufficiently to avoid chelation therapies—the current standard of care.

Myelodysplastic syndromes (MDS) represent another class of hematopoietic disorders where ERFE pathology could be therapeutically targeted. MDS is a group of malignancies characterized by impairment in the differentiation of blood cell precursors. Many of these undifferentiated cells undergo apoptosis in the bone marrow, but mutation and clonal expansion of surviving abnormal cells eventually selects for more malignant clones that progress to leukemia. Patients with the ring sideroblasts subtype (MDS-RS) develop nucleated erythroblasts containing excess iron that accumulates in mitochondria. These cells fail to mature or enter circulation. MDS is accompanied by mutations in splicing factor genes in 40-80% of patients, particularly in those with MDS-RS (Rozovski, Keating, and Estrov 2013). Mutations in the splicing factor *SF3B1* are especially relevant, as patients with MDS-RS and *SF3B1* mutations present with systemic iron overload even in the absence of blood transfusions. Bone marrow transcriptome analysis in a cohort of human MDS subjects revealed a mutated *ERFE* transcript in $SF3B1^{MUT}$ cells attributable to dysregulated splicing. The mutation adds four amino acids to

the translated protein, and the final product is still able to suppress hepcidin with efficacy comparable to the WT variant. Furthermore, *ERFE* mRNA abundance was significantly higher in these mutated cells relative to the $SF3B1^{WT}$ cells that were profiled (Bondu et al. 2019). Importantly, increased expression of this mutant ERFE was associated with longer survival of $SF3B1^{MUT}$ MDS patients. Since ERFE expression is induced in erythroblasts, it may be useful for these patients as an indicator that the abnormal clones are capable of differentiation and therefore less likely to become frankly malignant.

Chronic kidney disease (CKD) is associated with a characteristic anemia caused by a combination of relative erythropoietin deficiency and iron-restriction (Hanudel et al. 2017) (**Figure 1D**). The pathogenesis of anemia in CKD is multifactorial, including systemic inflammation, relative deficiency of EPO production, and low clearance of hepcidin by the diseased kidney. Current treatment guidelines suggest the monitoring of erythrocyte and iron parameters and the administration of iron and EPO to patients who become iron-deficient and anemic (Anemia Work Group 2012). A study of hepcidin knockout mice with an adenine diet-induced CKD showed that ablation of hepcidin improved the associated anemias (Hanudel et al. 2017). For those CKD patients whose anemia is mainly caused by increased hepcidin, future ERFE mimetics and activators could prove useful for the treatment of anemia. While the EPO administration currently used as therapy does induce endogenous ERFE, a mouse study revealed that serum ERFE levels have a delayed response in CKD mice relative to WT (Hanudel et al. 2018). The resulting delay in iron mobilization could make EPO less effective as an erythropoiesis-stimulating agent, raising the possibility that administration of bioengineered ERFE may have therapeutic utility in helping to mobilize iron in anemia of CKD.

3.4 Erythroferrone Variants

Another consideration of ERFE pathophysiology is the effect of excessive concentrations of the protein on iron-loading anemias. ERFE variants could change the bioactivity of the protein or modify the stability of mRNA transcripts or proteins, or a combination of all three. An example is the A260S substitution caused by a point mutation in the C1q domain. Healthy people with this mutation express higher levels of ERFE at the RNA and protein levels compared to their WT equivalents. The same increased expression is seen in patients with congenital dyserythropoietic anemia type II (CDAII) who also have the ERFE mutation (Andolfo et al. 2019). These patients have very high circulating ERFE protein levels at baseline because of ineffective erythropoiesis. The $ERFE^{A260S}$ mutation found in only a subset of CDAII patients drives RNA and protein expression up even higher. Remarkably, $ERFE^{A260S}$ is associated with severe anemia (Andolfo et al. 2019), possibly by making more iron available for erythropoiesis and increasing oxidative stress in the already impaired erythroblasts.

4. Erythroferrone as a Biomarker in Competitive Sports

4.1 Blood Doping

Monitoring the use of performance-enhancing drugs is a cat-and-mouse game between hypercompetitive athletes who try to skirt the rules and the organizations responsible for upholding the integrity of their sports competitions. Historically, anabolic steroids were commonly used to boost performance, but these drugs can be readily detected by the presence their metabolites in urine. Blood doping is the use of techniques or substances that increases the number of circulating red blood cells. The boosted oxygen carrying capacity from blood doping brings increased stamina and performance, and the artificial enhancement is more difficult to detect than steroids. Two common blood doping methods are erythrocyte transfusions and the administration of erythropoiesis-stimulating agents (ESAs) such as EPO. Unlike

steroids, enhanced red cell mass may be unsurprising—especially in athletes—and challenging to detect. In particular, the transfusion of blood shortly before a competition, especially if it is the athlete's own blood, is difficult to detect. The World Anti-Doping Agency has therefore recognized the need to monitor athletes' biological parameters over time to reveal the time-dependent alterations caused by doping rather than testing for the agents, substances, or methods themselves. They refer to these profiles as Athlete Biological Passports, and they are currently the most effective deterrent to the use of blood doping (Schumacher et al. 2012).

Hematological parameters that have been proposed for the detection of blood doping include reticulocyte percentage, hemoglobin concentration, plasma iron, ferritin, and hepcidin. A study in healthy, male athletes showed a positive correlation between hepcidin, hemoglobin, iron, and ferritin (Leuenberger et al. 2017). The same study went on to measure the direct effects of multiple recombinant EPO injections on these hematological values in healthy, male volunteers finding the expected increase in reticulocyte percentage and decrease in hepcidin. The drop in hepcidin came more quickly than the rise in reticulocytes for most participants: 2 days versus 4 days after the beginning of treatment. Hepcidin is a useful biomarker in this context because of its rapid and dramatic response to erythropoietic stimuli. It is important to note that hepcidin is also negatively regulated by plasma iron concentrations and positively regulated by inflammation (Nemeth et al. 2003) (**Figure 4**). Since intense exercise has the potential to induce both inflammation and erythropoiesis, this could lead to the generation of both positive and negative signals for hepcidin transcription. A review of the hepcidin response to exercise found an observed increase in serum levels in a vast majority of studies, largely regardless of exercise duration or intensity (Domínguez et al. 2018). This indicates that elevation of hepcidin by inflammation could mask the expected suppression of hepcidin by erythropoietic stimulants.

While hepcidin is regulated by multiple distinct pathways, marrow-derived ERFE is only known to be responsive to erythropoietic stimulation by EPO in the context of iron regulation. (For contexts where ERFE is produced in other tissues in response to non-erythropoietic stimuli, see the sections on myonectin and Xenopus.) Strict EPO regulation creates the potential for ERFE to serve as a blood doping biomarker with as much sensitivity as hepcidin and fewer confounders. As discussed in the myonectin section below, the stimuli for ERFE in non-erythropoietic contexts are not fully understood, but the contributions of non-erythroid sources to the systemic ERFE concentrations appear to be small. The following studies are part of a new and important effort to characterize the usefulness of ERFE in the detection of blood doping.

A small study in healthy males compared the effects of several EPO micro-doses (20 IU/kg) and small doses (50 IU/kg) on hepcidin and ERFE (Robach et al. 2020). As expected, serum hepcidin levels were quickly reduced in both dosing groups. Serum ERFE levels rose in response to the EPO injections, and unlike hepcidin, the response was dose-dependent rather than all-or-nothing. Another study compared the effects of EPO and two other common ESAs on serum ERFE levels. All three agents significantly increased ERFE levels starting from one day after administration (Ramirez Cuevas et al. 2020). The associated increase from a single dose was sustained for 6-13 days, with the duration depending on the ESA used. Iron supplementation and exercise-induced muscle damage did not affect the ERFE readings. If these findings hold true in larger studies, a sensitive and standardized human ERFE assay could be a useful addition to an athlete's hematological profile.

4.2 Altitude Training

Altitude training is a method of inducing erythropoiesis without the use of exogenous substances. Living at high altitude exposes the body to relative hypoxia which induces EPO production and increases erythropoiesis. The increased red cell mass and oxygen carrying capacity become advantageous when the athlete returns to sea level for training and competitions. Studies in athletes and healthy adults have shown that repetitive altitude training, or the use of normobaric hypoxia chambers to simulate the low-oxygen effects of high altitude, results in elevated EPO production (Frese and Friedmann-Bette 2010; Mackenzie, Watt, and Maxwell 2008), and an estimated 3.3% increase in hemoglobin mass after 20 days of altitude training compared to baseline (Gore et al. 2013). Normobaric hypoxia caused a decrease in plasma hepcidin within 2 days that lasted 2 weeks (Govus et al. 2017), and 15 hours of high altitude exposure was enough to increase serum ERFE concentrations (Robach et al. 2020). Altitude training is considered a legal form of blood doping, and as such, the practice is widely used in preparation for competitions. It remains to be determined whether ERFE measurement would enhance existing methodologies that distinguish between legal and illegal blood doping.

5. Erythroferrone beyond erythropoiesis and iron homeostasis

5.1 Myonectin

In 2012, a novel skeletal muscle-derived member of the CTRP family was characterized in mice and named myonectin (Seldin et al. 2012:15). Circulating levels of this new myokine were increased after exercise, and transcription of its RNA in cultured myotubes was induced by a rise in cellular cAMP or calcium levels. Based on these results, the authors proposed that the protein may be a marker or regulator of metabolism in muscle. It was later found to be expressed from the same gene and transcript as ERFE, but for the purposes of its metabolic roles and expression in muscle tissues, the name *myonectin* will continue to be used here. As

part of their characterization of myonectin, the authors described various ways the protein could be induced in mice including fasting followed by refeeding with normal chow, glucose, or emulsified lipids. C2C12 myotubes cultured *in vitro* with glucose or palmitate also increased expression of myonectin 4-fold compared to serum-starved conditions. Injection of recombinant myonectin in mice caused a reduction in non-esterified fatty acid levels that was believed to be the result of increased fatty acid uptake into cells. Isolated adipocytes and hepatocytes cultured with recombinant myonectin showed increased expression of a number of fatty acid binding and transport proteins as well as dose-dependent augmented palmitate uptake. After the initial characterization, several groups investigated the new myokine in various contexts.

5.1.1 Myonectin in glucose and fat metabolism

Whole body myonectin deletion in mice fed a high-fat diet led to increased fat storage in adipose lipid droplets (Little et al. 2019). This suggests the possibility that myonectin may be protective against insulin resistance. In order to test for associations in relevant populations, a study of circulating myonectin levels was performed in humans with type 2 diabetes and healthy control subjects (Li et al. 2019). Both groups were further stratified into lean, overweight, and obese subcategories. Serum myonectin was found to be significantly decreased in diabetes patients. Within both healthy and diabetic groups, increasing BMI was associated with lower levels of myonectin. Moreover, patients with higher BMI had lower circulating levels regardless of disease state, but the effect sizes in both analyses were small. A multivariate stepwise regression analysis of multiple parameters confirmed that high BMI was a main independent predictor of low myonectin in their study (Li et al. 2019). A similar study comparing type 2 diabetics to people with impaired and normal glucose tolerance found the exact opposite: metabolic disease parameters and obesity associated with higher circulating myonectin levels (Li et al. 2018). It should be noted that measurements of circulating myonectin in these studies

differed by a factor of 10 despite using the same ELISA assay system for detection. Authors of both studies agreed on myonectin's potential as a biomarker in predicting the development of obesity and type 2 diabetes, but the questions of cause, effect, and directionality remain open. Adding to the uncertainty, a calorie restriction experiment in rats showed no change in plasma myonectin levels between animals fed *ad libitum* and those restricted to 60% of standard. This is despite a drop in plasma levels of insulin and a rise in adiponectin in the calorie restricted group (Sharma, Castorena, and Cartee 2012). It is possible that myonectin is affected only during extreme stresses, whereas insulin sensitivity and other modes of fat regulation respond in a more sensitive manner, and possibly more consistently. As with all ERFE/myonectin detection systems, it is important to validate the assays using appropriate controls before the results can be reliably interpreted.

Experiments *in vitro* and *in vivo* were reported as showing that myonectin suppressed starvation-induced autophagy. Administration of recombinant myonectin to fasted animals and serum-starved hepatocytes reduced the expression of autophagy genes and prevented formation of autophagosomes (Seldin et al. 2013). Mechanistic studies using various pathway inhibitors revealed that this activity is accomplished through mTOR/Akt/PI3K. *In vitro* time course experiments in rat cardiomyocytes confirmed these findings by demonstrating an induction of pAkt, pCREB, and pGSK-3β within 15 minutes of treatment with recombinant myonectin (Otaka et al. 2018), though no cell surface receptors have been described to mediate this signaling. It was not reported if or how the recombinant myonectin protein was validated for their experiments.

In addition to refeeding, myonectin can be induced by exercise. A study in rats confirmed the original reports that myonectin protein levels increase in muscle after chronic exercise. Confusingly, RNA abundance of the myonectin transcript in diaphragm muscle was lower in the exercised group than in the control. This suppression of RNA but not protein was observed in both lean rats and in a genetic model of obesity where caloric intake from a normal diet is increased due to knockout of the leptin receptor (Peterson, Mart, and Bond 2014). A study in overweight human subjects found that chronic exercise significantly increased serum myonectin levels (Pourranjbar et al. 2018), but these results can be difficult to interpret. Since exercise can induce erythropoiesis, the change they observed may have been circulating ERFE that originated in the bone marrow. Pairing this with the contradictory RNA data highlights the need for a more complete analysis of the metabolic landscape. This analysis must include the effects on renal EPO production and marrow ERFE secretion in order to document the predominant tissue sources of ERFE/myonectin and the specific pathways that stimulate the increase in ERFE/myonectin plasma concentrations. More extensive assay validation is also needed to assure that the measurements are sufficiently sensitive and specific, and the consistent use of knockout animals as controls is required for appropriate attribution of myonectin effects.

Just upstream of ERFE/myonectin induction, erythropoietin has also been implicated in the regulation of cellular metabolism including glucose tolerance and fatty acid metabolism. Knockout of the mouse EPO receptor in all non-hematopoietic tissues resulted in increased body mass compared to WT animals with differences appearing as early as one week after birth (Teng et al. 2011). Transgenic mice that over-express EPO, or WT mice that are administered exogenous EPO, show a reduction in body mass and increase in glucose tolerance compared to untreated WT controls. Notably, these changes are not mediated by an EPO-related increase in erythropoiesis (Foskett et al. 2011; Teng et al. 2011). Indeed, experiments in erythroferrone

knockout mice demonstrated that a lack of the ERFE protein did not impair either glucose tolerance or clearance of non-esterified fatty acids after chronic or acute EPO treatment (Coffey et al. 2018). Taken together, these results demonstrate that the effects of erythropoietin on cellular metabolism are independent of its role in stimulating erythropoiesis.

5.1.2 Myonectin as a cardioprotective hormone

A comprehensive study on cardiac ischemia-reperfusion injury (IRI) in myonectin knockout and over-expressing mice found that myonectin was protective of heart muscle subjected to IRI, with knockouts experiencing more apoptosis in the heart than WT, and over-expressers suffering less cardiac damage. Specifically, pro-inflammatory gene expression levels and myocardial infarct size were both increased in myonectin KO mice subjected to IRI. Over-expression of myonectin in skeletal muscle resulted in reduced cardiac injury after IRI via an attenuation of cardiomyocyte apoptosis (Otaka et al. 2018). The mechanisms of cardio-protection seen in these experiments are unclear. It is also unknown how the various reported effects of myonectin—ranging from metabolic modulation in the contexts of feeding and exercise to this report of apoptosis mitigation in the heart—fit together in the big picture. Further complicating the matter are the known effects of ERFE in the erythroid system and its mechanism of action. While a BMP trapping mechanism is proving very important for hepcidin suppression by ERFE, its relevance is still unclear in the context of myonectin. Little progress has been made regarding research into the mechanism(s) of action of myonectin.

5.2 Erythroferrone in Xenopus development

Erythroferrone ortholog genes are present in all vertebrates. In a *Xenopus tropicalis* cDNA library developmental gain-of-function screen, transgenic *erfe* over-expression caused axis

duplication in the embryo (Melchert et al. 2020). This effect is known in other settings to be induced by either stimulation of Wnt/β-Catenin or inhibition of BMP signaling. Consistent with mammalian data, RT-qPCR analysis showed *Xenopus erfe* to be a potent inhibitor of BMP target genes. As in mammals, the active domain was found to be the N-terminal region and not the C1q globular head. Importantly, *Xenopus erfe* inhibited BMP4 signaling while murine ERFE did not. Consistent with this finding, injection of murine *Erfe* RNA did not cause secondary axis duplication unlike the *Xenopus* version, however over-expression of the murine variant did cause a mild dorsalization phenotype. The difference may be attributable to murine ERFE's relatively weaker binding to BMP4 than to BMP2 or BMP6 (Arezes et al. 2020), as primary axis formation during *Xenopus* development is mainly controlled by BMP4 (De Robertis 2009; De Robertis and Kuroda 2004). These data raise two possibilities for why our ERFE transgenic mice are less affected during development than the *Xenopus* embryos. One explanation is that divergent evolution in erythroferrone proteins leading to differential BMP4 binding may explain the difference in developmental abnormalities. Alternatively, overexpression of ERFE in our transgenic mice is driven by the β-globin promoter-enhancer, so ERFE synthesis in the mouse model begins in mid-gestation when β-globin synthesis starts in the mouse, perhaps too late for more dramatic developmental defects to appear. *Xenopus erfe* loss-of-function resulted in severely impaired blood circulation and edema at the tadpole stage. Together, these data demonstrate that *erfe* activity is required for normal morphological development and vascularization in *Xenopus,* raising the possibility that ERFE may have additional as of yet undescribed roles in mammals.

Conclusion

Since its discovery in 2014, erythroferrone has become recognized as a key erythroid regulator of iron homeostasis. In response to erythropoietic stimuli, increased ERFE levels suppress

hepcidin production, and the consequent stabilization of ferroportin mobilizes cellular iron stores into plasma for use by maturing erythroblasts. This important regulatory axis allows vertebrate species to respond to and rapidly recover from blood loss. It also allows for quick adaptation to low oxygen concentrations found at high altitudes—a physiological feature that some athletes use to gain advantages when competing at sea level. The potential of ERFE to serve as a biomarker of blood doping could have a beneficial impact on the fairness and safety of sports competitions. In hematological diseases with ineffective erythropoiesis like β-thalassemia and some subclasses of myelodysplastic syndrome, dysregulated ERFE leads to iron overload. Iron chelation is currently used as the standard-of-care therapy, but recent studies of anti-ERFE antibodies show potential utility in preventing iron overload in these disorders. Patients with chronic kidney disease have the opposite problem: high circulating levels of hepcidin and iron-restricted anemia. In these cases, the therapeutic administration of ERFE or ERFE mimetics could become a useful modality in the management of anemia. Despite the rapid progress made in understanding the role of erythroferrone in baseline, stress, and disease-state erythropoiesis, there is much about the hormone that remains to be explained. We are only beginning to understand how ERFE suppresses hepcidin, with the best-supported mechanism dependent on the ability of ERFE to trap BMPs and prevent their interactions with the BMP receptor complex that regulates hepcidin transcription. Furthermore, the effects of multimerization on the regulation and potency of ERFE remain unknown. Much remains to be discovered about the role of erythroferrone in embryonic development and its roles in muscle biology and systemic metabolism. Discoveries in these areas may have important implications for understanding the entire CTRP family whose biological functions remain largely unknown.

Acknowledgments

The authors would like to thank Elizabeta Nemeth for reviewing the manuscript and acknowledge Richard Coffey for sharing prepublication data on ERFE transgenic mice. Funding for work related to this article was provided by NIH R01DK126680 (TG).

Conflict of Interests

Tomas Ganz is a scientific cofounder of Intrinsic LifeSciences and Silarus Pharma and has been consulted for ADARx, Akebia, Pharmacosmos, Ionis, Gossamer Bio, Global Blood Therapeutics, American Regent, Disc Medicine, and Rockwell Scientific. Tomas Ganz is also listed as an inventor on patents related to erythroferrone. While Daniel N Srole declares no conflict of interest.

Author Contributions

Daniel N. Srole and Tomas Ganz drafted and edited the manuscript. Figures were created with contributions from both authors.

References

Andolfo, Immacolata, Barbara Eleni Rosato, Roberta Marra, Gianluca De Rosa, Francesco Manna, Antonella Gambale, Achille Iolascon, and Roberta Russo. 2019. “The BMP-SMAD Pathway Mediates the Impaired Hepatic Iron Metabolism Associated with the ERFE-A260S Variant.” *American Journal of Hematology* 94(11):1227–35. doi: 10.1002/ajh.25613.

Anemia Work Group. 2012. “KDIGO Clinical Practice Guideline for Anemia in Chronic Kidney Disease.” *Kidney International Supplements* 2(4):279–335. doi: 10.1038/kisup.2012.40.

Arezes, João, Niall Foy, Kirsty McHugh, Doris Quinkert, Susan Benard, Anagha Sawant, Joe N. Frost, Andrew E. Armitage, Sant-Rayn Pasricha, Pei Jin Lim, May S. Tam, Edward Lavallie, Debra D. Pittman, Orla Cunningham, Matthew Lambert, John E. Murphy, Simon J. Draper, Reema Jasuja, and Hal Drakesmith. 2020. “Antibodies against the Erythroferrone N-Terminal Domain Prevent Hepcidin Suppression and Ameliorate Murine Thalassemia.” *Blood* 135(8):547–57. doi: 10.1182/blood.2019003140.

Arezes, João, Niall Foy, Kirsty McHugh, Anagha Sawant, Doris Quinkert, Virginie Terraube, Alette Brinth, May Tam, Edward R. LaVallie, Stephen Taylor, Andrew E. Armitage, Sant-Rayn Pasricha, Orla Cunningham, Matthew Lambert, Simon J. Draper, Reema Jasuja, and Hal Drakesmith. 2018. “Erythroferrone Inhibits the Induction of Hepcidin by BMP6.” *Blood* 132(14):1473–77. doi: 10.1182/blood-2018-06-857995.

Aschemeyer, Sharraya, Victoria Gabayan, Tomas Ganz, Elizabeta Nemeth, and Léon Kautz. 2017. “Erythroferrone and Matriptase-2 Independently Regulate Hepcidin Expression.” *American Journal of Hematology* 92(5):E61–63. doi: 10.1002/ajh.24672.

Blom, Nikolaj, Thomas Sicheritz-Pontén, Ramneek Gupta, Steen Gammeltoft, and Søren Brunak. 2004. “Prediction of Post-Translational Glycosylation and Phosphorylation of Proteins from the Amino Acid Sequence.” *PROTEOMICS* 4(6):1633–49. doi: 10.1002/pmic.200300771.

Bondu, Sabrina, Anne-Sophie Alary, Carine Lefèvre, Alexandre Houy, Grace Jung, Thibaud Lefebvre, David Rombaut, Ismael Boussaid, Abderrahmane Bousta, François Guillonneau, Prunelle Perrier, Samar Alsafadi, Michel Wassef, Raphaël Margueron, Alice Rousseau, Nathalie Droin, Nicolas Cagnard, Sophie Kaltenbach, Susann Winter, Anne-Sophie Kubasch, Didier Bouscary, Valeria Santini, Andrea Toma, Mathilde Hunault, Aspasia Stamatoullas, Emmanuel Gyan, Thomas Cluzeau, Uwe Platzbecker, Lionel Adès, Hervé Puy, Marc-Henri Stern, Zoubida Karim, Patrick Mayeux, Elizabeta Nemeth, Sophie Park, Tomas Ganz, Léon Kautz, Olivier Kosmider, and Michaëla Fontenay. 2019. “A Variant Erythroferrone Disrupts Iron Homeostasis in *SF3B1* -Mutated Myelodysplastic Syndrome.” *Science Translational Medicine* 11(500):eaav5467. doi: 10.1126/scitranslmed.aav5467.

Coffey, Richard, Ugo Sardo, Léon Kautz, Victoria Gabayan, Elizabeta Nemeth, and Tomas Ganz. 2018. “Erythroferrone Is Not Required for the Glucoregulatory and Hematologic Effects of Chronic Erythropoietin Treatment in Mice.” *Physiological Reports* 6(19):e13890. doi: 10.14814/phy2.13890.

De Robertis, E. M. 2009. “Spemann’s Organizer and the Self-Regulation of Embryonic Fields.” *Mechanisms of Development* 126(11–12):925–41. doi: 10.1016/j.mod.2009.08.004.

De Robertis, Edward M., and Hiroki Kuroda. 2004. “DORSAL-VENTRAL PATTERNING AND NEURAL INDUCTION IN *XENOPUS* EMBRYOS.” *Annual Review of Cell and Developmental Biology* 20(1):285–308. doi: 10.1146/annurev.cellbio.20.011403.154124.

Domínguez, Raúl, Antonio Sánchez-Oliver, Fernando Mata-Ordoñez, Adrián Feria-Madueño, Moisés Grimaldi-Puyana, Álvaro López-Samanes, and Alberto Pérez-López. 2018. “Effects of an Acute Exercise Bout on Serum Hepcidin Levels.” *Nutrients* 10(2):209. doi: 10.3390/nu10020209.

Foskett, Amanda, Mawadda Alnaeeli, Li Wang, Ruifeng Teng, and Constance T. Noguchi. 2011. “The Effects of Erythropoietin Dose Titration during High-Fat Diet-Induced Obesity.” *Journal of Biomedicine and Biotechnology* 2011:1–8. doi: 10.1155/2011/373781.

Frese, F., and B. Friedmann-Bette. 2010. “Effects of Repetitive Training at Low Altitude on Erythropoiesis in 400 and 800 m Runners.” *International Journal of Sports Medicine* 31(06):382–88. doi: 10.1055/s-0030-1248328.

Gammella, Elena, Victor Diaz, Stefania Recalcati, Paolo Buratti, Michele Samaja, Soumyadeep Dey, Constance Tom Noguchi, Max Gassmann, and Gaetano Cairo. 2015. “Erythropoietin’s Inhibiting Impact on Hepcidin Expression Occurs Indirectly.” *American Journal of Physiology-Regulatory, Integrative and Comparative Physiology* 308(4):R330–35. doi: 10.1152/ajpregu.00410.2014.

Ganz, Tomas, Grace Jung, Arash Naeim, Yelena Ginzburg, Zahra Pakbaz, Patrick B. Walter, Léon Kautz, and Elizabeta Nemeth. 2017. “Immunoassay for Human Serum Erythroferrone.” *Blood* 130(10):1243–46. doi: 10.1182/blood-2017-04-777987.

Gore, Christopher J., Ken Sharpe, Laura A. Garvican-Lewis, Philo U. Saunders, Clare E. Humberstone, Eileen Y. Robertson, Nadine B. Wachsmuth, Sally A. Clark, Blake D. McLean, Birgit Friedmann-Bette, Mitsuo Neya, Torben Pottgiesser, Yorck O. Schumacher, and Walter F. Schmidt. 2013. “Altitude Training and Haemoglobin Mass from the Optimised Carbon Monoxide Rebreathing Method Determined by a Meta-Analysis.” *British Journal of Sports Medicine* 47(Suppl 1):i31–39. doi: 10.1136/bjsports-2013-092840.

Govus, A. D., P. Peeling, C. R. Abbiss, N. G. Lawler, D. W. Swinkels, C. M. Laarakkers, K. G. Thompson, J. J. Peiffer, C. J. Gore, and L. A. Garvican-Lewis. 2017. “Live High, Train Low - Influence on Resting and Post-Exercise Hepcidin Levels.” *Scandinavian Journal of Medicine & Science in Sports* 27(7):704–13. doi: 10.1111/sms.12685.

Gutschow, Patrick, Huiling Han, Gordana Olbina, Keith Westerman, Eileen Westerman, Marc Ruiz Martinez, Yelena Ginzburg, Elizabeta Nemeth, Tomas Ganz, and Vaughn Ostland. 2019. “A Novel Sandwich ELISA to Quantify Erythroferrone in Mouse Serum.” *Blood* 134(Supplement_1):2237–2237. doi: 10.1182/blood-2019-130947.

Haase, Volker H. 2013. “Regulation of Erythropoiesis by Hypoxia-Inducible Factors.” *Blood Reviews* 27(1):41–53. doi: 10.1016/j.blre.2012.12.003.

Hanudel, Mark R., Maxime Rappaport, Kristine Chua, Victoria Gabayan, Bo Qiao, Grace Jung, Isidro B. Salusky, Tomas Ganz, and Elizabeta Nemeth. 2018. “Levels of the Erythropoietin-Responsive Hormone Erythroferrone in Mice and Humans with Chronic Kidney Disease.” *Haematologica* 103(4):e141–42. doi: 10.3324/haematol.2017.181743.

Hanudel, Mark R., Maxime Rappaport, Victoria Gabayan, Grace Jung, Isidro B. Salusky, Elizabeta Nemeth, Tomas Ganz, and Joshua Zaritsky. 2017. “Increased Serum Hepcidin Contributes to the Anemia of Chronic Kidney Disease in a Murine Model.” *Haematologica* 102(3):e85–88. doi: 10.3324/haematol.2016.150433.

Hodges, Vivien M., Susan Rainey, Terence R. Lappin, and A. Peter Maxwell. 2007. “Pathophysiology of Anemia and Erythrocytosis.” *Critical Reviews in Oncology/Hematology* 64(2):139–58. doi: 10.1016/j.critrevonc.2007.06.006.

Kautz, Léon, Grace Jung, Xin Du, Victoria Gabayan, Justin Chapman, Marc Nasoff, Elizabeta Nemeth, and Tomas Ganz. 2015. “Erythroferrone Contributes to Hepcidin Suppression and Iron Overload in a Mouse Model of β-Thalassemia.” *Blood* 126(17):2031–37. doi: 10.1182/blood-2015-07-658419.

Kautz, Léon, Grace Jung, Erika V. Valore, Stefano Rivella, Elizabeta Nemeth, and Tomas Ganz. 2014. “Identification of Erythroferrone as an Erythroid Regulator of Iron Metabolism.” *Nature Genetics* 46(7):678–84. doi: 10.1038/ng.2996.

Kim, Airie, and Elizabeta Nemeth. 2015. “New Insights into Iron Regulation and Erythropoiesis:” *Current Opinion in Hematology* 22(3):199–205. doi: 10.1097/MOH.0000000000000132.

Leuenberger, Nicolas, Emanuele Bulla, Olivier Salamin, Raul Nicoli, Neil Robinson, Norbert Baume, and Martial Saugy. 2017. “Hepcidin as a Potential Biomarker for Blood Doping: Hepcidin and Blood Doping.” *Drug Testing and Analysis* 9(7):1093–97. doi: 10.1002/dta.2122.

Li, Kejia, Xin Liao, Kuan Wang, Qiao Mi, Tingran Zhang, Yanjun Jia, Xiaohuei Xu, Xiaoheu Luo, Cheng Zhang, Hua Liu, Hongting Zhen, Ling Li, and Gangyi Yang. 2018. “Myonectin Predicts the Development of Type 2 Diabetes.” *The Journal of Clinical Endocrinology & Metabolism* 103(1):139–47. doi: 10.1210/jc.2017-01604.

Li, Zhu, Yan-Ling Yang, Yan-Juan Zhu, Chen-Guang Li, Yun-Zhao Tang, Chang-Lin Ni, Li-Ming Chen, and Wen-Yan Niu. 2019. “Circulating Serum Myonectin Levels in Obesity and Type 2 Diabetes Mellitus.” *Experimental and Clinical Endocrinology & Diabetes* a-0896-8548. doi: 10.1055/a-0896-8548.

Little, Hannah C., Susana Rodriguez, Xia Lei, Stefanie Y. Tan, Ashley N. Stewart, Ageline Sahagun, Dylan C. Sarver, and G. William Wong. 2019. “Myonectin Deletion Promotes Adipose Fat Storage and Reduces Liver Steatosis.” *The FASEB Journal* 33(7):8666–87. doi: 10.1096/fj.201900520R.

Mackenzie, Richard W. A., Peter W. Watt, and Neil S. Maxwell. 2008. “Acute Normobaric Hypoxia Stimulates Erythropoietin Release.” *High Altitude Medicine & Biology* 9(1):28–37. doi: 10.1089/ham.2007.1043.

Melchert, Juliane, Kristine A. Henningfeld, Sven Richts, Thomas Lingner, Danny Jonigk, and Tomas Pieler. 2020. “The Secreted BMP Antagonist ERFE Is Required for the Development of a Functional Circulatory System in Xenopus.” *Developmental Biology* 459(2):138–48. doi: 10.1016/j.ydbio.2019.12.007.

Mirciov, Cornel S. G., Sarah J. Wilkins, Linda A. Dunn, Gregory J. Anderson, and David M. Frazer. 2017. “Characterization of Putative Erythroid Regulators of Hepcidin in Mouse Models of Anemia” edited by K. Pantopoulos. *PLOS ONE* 12(1):e0171054. doi: 10.1371/journal.pone.0171054.

Mirciov, Cornel S. G., Sarah J. Wilkins, Grace C. C. Hung, Sheridan L. Helman, Gregory J. Anderson, and David M. Frazer. 2018. “Circulating Iron Levels Influence the Regulation of Hepcidin Following Stimulated Erythropoiesis.” *Haematologica* 103(10):1616–26. doi: 10.3324/haematol.2017.187245.

Nai, Antonella, Aude Rubio, Alessandro Campanella, Ophélie Gourbeyre, Irene Artuso, Jessica Bordini, Aurélie Gineste, Chloé Latour, Céline Besson-Fournier, Herbert Y. Lin, Hélène Coppin, Marie-Paule Roth, Clara Camaschella, Laura Silvestri, and Delphine Meynard. 2016. “Limiting Hepatic Bmp-Smad Signaling by Matriptase-2 Is Required for Erythropoietin-Mediated Hepcidin Suppression in Mice.” *Blood* 127(19):2327–36. doi: 10.1182/blood-2015-11-681494.

Nemeth, E. 2004. “Hepcidin Regulates Cellular Iron Efflux by Binding to Ferroportin and Inducing Its Internalization.” *Science* 306(5704):2090–93. doi: 10.1126/science.1104742.

Nemeth, Elizabeta, Erika V. Valore, Mary Territo, Gary Schiller, Alan Lichtenstein, and Tomas Ganz. 2003. “Hepcidin, a Putative Mediator of Anemia of Inflammation, Is a Type II Acute-Phase Protein.” *Blood* 101(7):2461–63. doi: 10.1182/blood-2002-10-3235.

Otaka, Naoya, Rei Shibata, Koji Ohashi, Yusuke Uemura, Takahiro Kambara, Takashi Enomoto, Hayato Ogawa, Masanori Ito, Hiroshi Kawanishi, Sonomi Maruyama, Yusuke Joki, Yusuke Fujikawa, Shingo Narita, Kazumasa Unno, Yoshiyuki Kawamoto, Takashi Murate, Toyoaki Murohara, and Noriyuki Ouchi. 2018. “Myonectin Is an Exercise-Induced Myokine That Protects the Heart From Ischemia-Reperfusion Injury.” *Circulation Research* 123(12):1326–38. doi: 10.1161/CIRCRESAHA.118.313777.

Pak, Mihwa, Miguel A. Lopez, Victroia Gabayan, Tomas Ganz, and Seth Rivera. 2006. “Suppression of Hepcidin during Anemia Requires Erythropoietic Activity.” *Blood* 108(12):3730–35. doi: 10.1182/blood-2006-06-028787.

Peterson, Jonathan M., Ryan Mart, and Cherie E. Bond. 2014. “Effect of Obesity and Exercise on the Expression of the Novel Myokines, Myonectin and Fibronectin Type III Domain Containing 5.” *PeerJ* 2:e605. doi: 10.7717/peerj.605.

Pourranjbar, Mohammad, Najmeh Arabnejad, Khatereh Naderipour, and Forouzan Rafie. 2018. “Effects of Aerobic Exercises on Serum Levels of Myonectin and Insulin Resistance in Obese and Overweight Women.” *Journal of Medicine and Life* 11(4):381–86. doi: 10.25122/jml-2018-0033.

Ramirez Cuevas, Kelvin, Céline Schobinger, Emeric Gottardo, Sven Christian Voss, Tiia Kuuranne, Jean-Daniel Tissot, Bernard Favrat, Nathan Townsend, and Nicolas

Leuenberger. 2020. “Erythroferrone as a Sensitive Biomarker to Detect Stimulation of Erythropoiesis.” *Drug Testing and Analysis* 12(2):261–67. doi: 10.1002/dta.2720.

Robach, Paul, Elena Gammella, Stefania Recalcati, Domenico Girelli, Annalisa Castagna, Matthieu Roustit, Carsten Lundby, Anne-Kristine Lundby, Pierre Bouzat, Samuel Vergès, Guillaume Séchaud, Pierluigi Banco, Mario Uhr, Catherine Cornu, Pierre Sallet, and Gaetano Cairo. 2020. “Induction of Erythroferrone in Healthy Humans by Micro-Dose Recombinant Erythropoietin or High-Altitude Exposure.” *Haematologica* haematol.2019.233874. doi: 10.3324/haematol.2019.233874.

Rozovski, Uri, Michael Keating, and Zeev Estrov. 2013. “The Significance of Spliceosome Mutations in Chronic Lymphocytic Leukemia.” *Leukemia & Lymphoma* 54(7):1364–66. doi: 10.3109/10428194.2012.742528.

Schäffler, Andreas, and Christa Buechler. 2012. “CTRP Family: Linking Immunity to Metabolism.” *Trends in Endocrinology & Metabolism* 23(4):194–204. doi: 10.1016/j.tem.2011.12.003.

Schumacher, Yorck Olaf, Martial Saugy, Torben Pottgiesser, and Neil Robinson. 2012. “Detection of EPO Doping and Blood Doping: The Haematological Module of the Athlete Biological Passport: The Haematological Module of the Athlete Biological Passport.” *Drug Testing and Analysis* 4(11):846–53. doi: 10.1002/dta.406.

Seldin, Marcus M., Xia Lei, Stefanie Y. Tan, Kevin P. Stanson, Zhikui Wei, and G. William Wong. 2013. “Skeletal Muscle-Derived Myonectin Activates the Mammalian Target of Rapamycin (MTOR) Pathway to Suppress Autophagy in Liver.” *Journal of Biological Chemistry* 288(50):36073–82. doi: 10.1074/jbc.M113.500736.

Seldin, Marcus M., Jonathan M. Peterson, Mardi S. Byerly, Zhikui Wei, and G. William Wong. 2012. “Myonectin (CTRP15), a Novel Myokine That Links Skeletal Muscle to Systemic Lipid Homeostasis.” *Journal of Biological Chemistry* 287(15):11968–80. doi: 10.1074/jbc.M111.336834.

Seldin, Marcus M., Stefanie Y. Tan, and G. William Wong. 2014. “Metabolic Function of the CTRP Family of Hormones.” *Reviews in Endocrine and Metabolic Disorders* 15(2):111–23. doi: 10.1007/s11154-013-9255-7.

Sharma, Naveen, Carlos M. Castorena, and Gregory D. Cartee. 2012. “Greater Insulin Sensitivity in Calorie Restricted Rats Occurs with Unaltered Circulating Levels of Several Important Myokines and Cytokines.” *Nutrition & Metabolism* 9(1):90. doi: 10.1186/1743-7075-9-90.

Teng, Ruifeng, Oksana Gavrilova, Norio Suzuki, Tatyana Chanturiya, Daniel Schimel, Lynne Hugendubler, Selin Mammen, Dena R. Yver, Samuel W. Cushman, Elisabetta Mueller, Masayuki Yamamoto, Lewis L. Hsu, and Constance Tom Noguchi. 2011. “Disrupted Erythropoietin Signalling Promotes Obesity and Alters Hypothalamus Proopiomelanocortin Production.” *Nature Communications* 2(1):520. doi: 10.1038/ncomms1526.

Vento, Sandro, Francesca Cainelli, and Francesco Cesario. 2006. “Infections and Thalassaemia.” *The Lancet Infectious Diseases* 6(4):226–33. doi: 10.1016/S1473-3099(06)70437-6.

Vokurka, M., J. Krijt, K. Sulc, and E. Necas. 2006. “Hepcidin MRNA Levels in Mouse Liver Respond to Inhibition of Erythropoiesis.” *Physiological Research* 55(6):667–74.

Wang, Chia-Yu, Amanda B. Core, Susanna Canali, Kimberly B. Zumbrennen-Bullough, Sinan Ozer, Lieve Umans, An Zwijsen, and Jodie L. Babitt. 2017. “Smad1/5 Is Required for Erythropoietin-Mediated Suppression of Hepcidin in Mice.” *Blood* 130(1):73–83. doi: 10.1182/blood-2016-12-759423.

Wang, Chia-Yu, Yang Xu, Lisa Traeger, Deniz Y. Dogan, Xia Xiao, Andrea U. Steinbicker, and Jodie L. Babitt. 2020. “Erythroferrone Lowers Hepcidin by Sequestering BMP2/6 Heterodimer from Binding to the BMP Type I Receptor ALK3.” *Blood* 135(6):453–56. doi: 10.1182/blood.2019002620.

Wang, Yu, Karen S. L. Lam, Ming-hon Yau, and Aimin Xu. 2008. “Post-Translational Modifications of Adiponectin: Mechanisms and Functional Implications.” *Biochemical Journal* 409(3):623–33. doi: 10.1042/BJ20071492.

Wong, G. W., J. Wang, C. Hug, T. S. Tsao, and H. F. Lodish. 2004. “A Family of Acrp30/Adiponectin Structural and Functional Paralogs.” *Proceedings of the National Academy of Sciences* 101(28):10302–7. doi: 10.1073/pnas.0403760101.

Yadav, Amita, Megha A. Kataria, Vandana Saini, and Anil Yadav. 2013. “Role of Leptin and Adiponectin in Insulin Resistance.” *Clinica Chimica Acta* 417:80–84. doi: 10.1016/j.cca.2012.12.007.

Yamauchi, Toshimasa, Junji Kamon, Yusuke Ito, Atsushi Tsuchida, Takehiko Yokomizo, Shunbun Kita, Takuya Sugiyama, Makoto Miyagishi, Kazuo Hara, Masaki Tsunoda, Koji Murakami, Toshiaki Ohteki, Shoko Uchida, Sato Takekawa, Hironori Waki, Nelson H. Tsuno, Yoichi Shibata, Yasuo Terauchi, Philippe Froguel, Kazuyuki Tobe, Shigeo Koyasu, Kazunari Taira, Toshio Kitamura, Takao Shimizu, Ryozo Nagai, and Takashi Kadowaki. 2003. “Cloning of Adiponectin Receptors That Mediate Antidiabetic Metabolic Effects.” *Nature* 423(6941):762–69. doi: 10.1038/nature01705.

Chapter 2

Characterization of erythroferrone structural domains relevant to its iron-regulatory function

The contents of this chapter are a version of an article originally submitted to the Journal of Biological Chemistry on July 28, 2023.

Srole DN, Jung G, Waring AJ, Nemeth E, Ganz T. Characterization of erythroferrone structural domains relevant to its iron-regulatory function. *Journal of Biological Chemistry*. In revision.

Abstract

As erythropoiesis consumes most of the circulating plasma iron, iron delivery to the plasma is closely coupled to erythropoiesis. In response to hemorrhage and other erythropoietic stresses, increased erythropoietin stimulates the production of the hormone erythroferrone (ERFE) by erythrocyte precursors (erythroblasts) developing in erythropoietic tissues. ERFE acts on the liver to inhibit bone morphogenetic protein (BMP) signaling and thereby decrease hepcidin production. Decreased circulating hepcidin concentrations then allow the release of iron from stores and increase iron absorption from the diet. Guided by evolutionary analysis and Alphafold2 protein complex modeling, we used targeted ERFE mutations, deletions, and synthetic ERFE segments together with cell-based bioassays and surface plasmon resonance to probe the structural features required for bioactivity and BMP binding. We define the ERFE active domain and multiple structural features that act together to entrap BMP ligands. We

demonstrate that the BMP-ERFE binding interactions are similar to those that bind BMPs to their cognate receptors. Finally, we identify structural determinants of ERFE multimerization that increase the avidity of ERFE for BMP ligands.

1. Introduction

Iron is an essential micronutrient required for many cellular and organismal processes in nearly all living organisms. Experimental studies in humans and laboratory rodents have shown that the absorption, storage, and transport of iron atoms is tightly regulated. Hepcidin—a small peptide hormone produced by the liver—controls the movement of iron into plasma by occluding and internalizing its receptor, the cellular iron exporter ferroportin[1]. Numerous stimuli regulate the transcription of the hepcidin gene *HAMP*, either to induce or to suppress hepcidin production. Iron loading in the liver increases hepcidin secretion by hepatocytes by stimulating sinusoidal endothelial cells to produce bone morphogenetic proteins (BMPs) which act on hepatocytes to induce *HAMP* transcription via the BMP-SMAD pathway[2]. Inflammation induces *HAMP* transcription via IL-6 signaling through the JAK-STAT pathway[3,4]. Hypoxia is sensed in the kidneys to increase HIF-2α and thereby stimulate erythropoietin (EPO) production. EPO then acts on the marrow to stimulate erythropoiesis and to increase the secretion of erythroid factors that act on the liver to lower *HAMP* transcription, decrease hepcidin protein levels, and make iron available for erythropoiesis[5,6].

Erythroferrone (ERFE) is produced by erythroblasts in the marrow or spleen in response to EPO signaling. By inhibition of the hepatic BMP-SMAD signaling axis, ERFE suppresses hepcidin transcription in the liver to decrease circulating hepcidin concentrations and thereby increase iron absorption from the diet and to mobilize iron from stores in hepatocytes and macrophages.

Apart from the physiological role of ERFE in erythropoietic recovery, ERFE also plays a pathological role in anemias with ineffective erythropoiesis (e.g. β-thalassemia) where excessive production of ERFE, as a result of high EPO levels and a greatly expanded population of erythroblasts, contributes to the development of iron overload[7–9].

Regarding the mechanism of action of ERFE, surface plasmon resonance and competition studies have demonstrated that ERFE binds to and neutralizes a subset of BMP ligands[9], and that the N-terminus of ERFE is sufficient for its bioactivity. The post-translational modifications of ERFE that affect its folding, secretion, and multimerization have also been analyzed[10] but the effects of these structural features on ERFE bioactivity have not examined.

In the current study, we performed molecular characterization of the human erythroferrone protein to identify features that are important for its hepcidin-regulating activity and therefore its (patho)physiological role in iron mobilization. Using protein modeling and docking models, mutagenesis, cell-based bioassays, and surface plasmon resonance, we identified the ERFE active domain, structural features and amino acid residues that are key to its function, and generated an updated model of the ERFE structure-function relationship.

2. **Results**

2.1. Structure-function study of the N- and C-terminus of erythroferrone

Like all members of the C1q/TNFα Related Protein family (CTRP), ERFE is predicted to contain a leading signal sequence that directs it for secretion, a variable N-terminal region, and a TNFα-like head at the C-terminus **(Figure 1A)**. We used AlphaFold2 to generate a model of the human ERFE structure. As expected, the algorithm predicts a highly structured C-terminus and

mostly unstructured N-terminus **(Figure 1B)**. Within the N-terminus, the model contains three small alpha helices but no other well-defined structural elements. These helices along with the C-terminal head are predicted with the highest confidence, while the majority of the N-terminus is generated with low or very low confidence suggesting that this portion of the protein is disordered.

The mature human N-terminus is predicted to begin at Glu43 following a RARR PCSK3/furin recognition site which results in cleavage of the upstream region from the mature protein. The alignment of vertebrate ERFE sequences reveals that large parts of the N-terminus and nearly the entire C-terminus are remarkably conserved **(Figure 1C)**. Despite the disordered nature of the N-terminus, several distinct structural features within it—distinguished by charge or polarity—appear to be retained across the range of vertebrate species.

To explore the functional properties of the ERFE domains, we designed constructs representing the N-terminal portion (amino acids 43-148), C-terminal portion corresponding to the globular head (186-354), and a full-length construct that represents the mature molecule (43-354). All three constructs use a pcDNA3.1 backbone and contain the ERFE signal sequence that is cleaved during secretion, followed by a retained FLAG tag upstream of the coding sequence **(Figure 1D, top)**.

To assess bioactivity of the ERFE fragments, we overexpressed full-length, N-terminal, and C-terminal ERFE segments using HEK293T cells **(Figure S-1)**, determined the molar concentration of the proteins by quantitative Western blotting and treated the human hepatocyte Hep3B cell line with serial dilutions of ERFE-containing supernatants **(Figure 1D, bottom)**. Like

full-length ERFE, the N-terminal segment potently suppressed hepcidin transcription, in agreement with published studies[9]. The C-terminal segment alone did not exhibit bioactivity in this assay.

ERFE has previously been shown to interact with BMPs[9,11,12], and sequestration of BMPs from the BMP receptors may be the mechanism of action of hepcidin suppression. We used surface plasmon resonance (SPR) to determine binding avidities for BMP species that are known to be important for hepcidin induction[13]: a heterodimer of BMP2/6 and homodimers of BMP2 and BMP6 **(Figure 1E)**. Mirroring hepcidin suppression, the ERFE N-terminus and the full-length protein bind to these BMPs, whereas the C-terminus does not bind. Our data confirm that the relatively unstructured N-terminal segment but not the highly structured C-terminal portion of ERFE is required for both binding to BMPs and for hepcidin suppression. Nevertheless, while the C-terminus does not interact with any BMP tested, its presence in the full-length protein increases avidity for the ligands as demonstrated by more than an order-of-magnitude higher avidity for BMPs than the N-terminus alone **(Table 1)**.

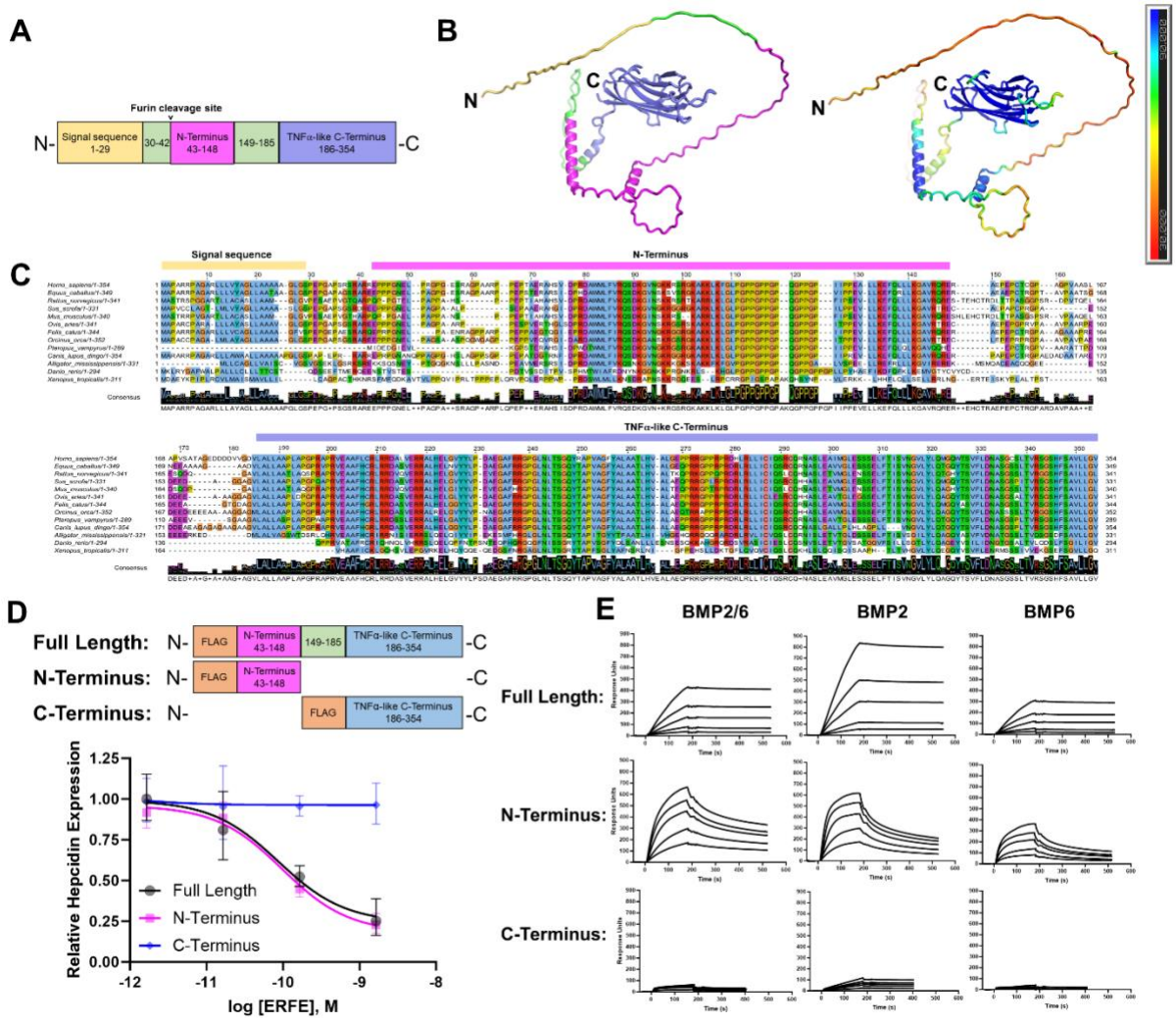

Figure 1: Structure-function study of the N- and C-terminus of ERFE

(A) Diagram of the human ERFE protein showing the signal sequence, N-terminal, and C-terminal domains and their respective amino acid boundaries. (B) AlphaFold2 model of human ERFE structure (left; colors correspond to segments in the diagram A, and right; colored by confidence parameter pLDDT, blue = highest degree of confidence). (C) Amino acid conservation alignments of ERFE N-terminal and C-terminal domains across vertebrate species. (D) Top: Diagrams of full-length, N-terminus, and C-terminus ERFE constructs that were used in bioassay and SPR. Bottom: qPCR expression of hepcidin in Hep3B cells treated with a range of concentrations of ERFE variants for 16 h. Data are normalized to untreated

controls. N = 3 biological replicates. (E) Surface plasmon resonance sensorgrams of full-length, N-terminal, and C-terminal ERFE binding to immobilized BMP2, BMP6, and BMP2/6.

2.2. The N-terminal active domain contains multiple BMP-binding features

We next generated overlapping 18-mer peptides that span the N-terminal domain of human erythroferrone **(Figure S-2A)** and used SPR to detect their binding to BMP2/6, BMP2, or BMP6 **(Figure 2A, S2-B)**. Four of the peptides (73-90, 97-114, 121-138, and 133-150) interacted with BMP ligands, indicating that ERFE may contain multiple potential contact points for BMPs. Based on these four peptides and distinct features of the ERFE protein sequence, we focused on four regions in the N-terminus: the Hydrophobic Segment (81-86), the Cationic Segment (96-107), the Collagen Segment (109-125), and the Helical Segment (126-148) **(Figure 2B)**.

To model how these segments interact with BMPs, we used AlphaFold2 to dock the full-length ERFE protein to a BMP2/6 dimer **(Figure 2C).** BMP2 and BMP6 homodimers interacted with ERFE in a similar manner except for the position of the globular head which was highly variable (**Figure S-2D, E**). In all three situations, two of the four segments were predicted by the model to directly interact with the BMP: the Hydrophobic Segment containing a conserved tryptophan (W82) that appears to interact with two tryptophans of BMP2 (W310 and W313), and the Helical Segment which has a conserved phenylalanine (F136) interacting with two BMP leucines (L372 and L382). In this docking model, the predicted local distance difference test (pLDDT) scores of the local structure are higher at these interaction sites than anywhere else in the N-terminus but the interaction at the Helical Segment appears much more variable **(Figure S-2C, D, E)**.

To validate our findings by an independent method, we generated a second model of the same ERFE-BMP2 dimer interaction using a molecular dynamics refined coordinate set[14].

This second model predicts an identical interaction in the Hydrophobic Segment between the same residues of ERFE and BMP2 as AlphaFold2 **(Figure 2D)**. A second contact between the

ERFE Helical Segment and BMP wing is present in this model, but it does not exactly match the residues identified by AlphaFold2. Neither model predicts the interactions of the Cationic or Collagen Segments with BMP that were detected by our SPR 18-mer peptide scan. The discrepancy is not surprising as the 18-mer peptides are linear sequences that could make more contacts with BMPs than the 3-dimensional folded full-length protein. The AlphaFold2 and molecular dynamics refined models also differ in their positioning of the C-terminus, but both agree with our experimental finding that the region has no direct interaction with BMPs.

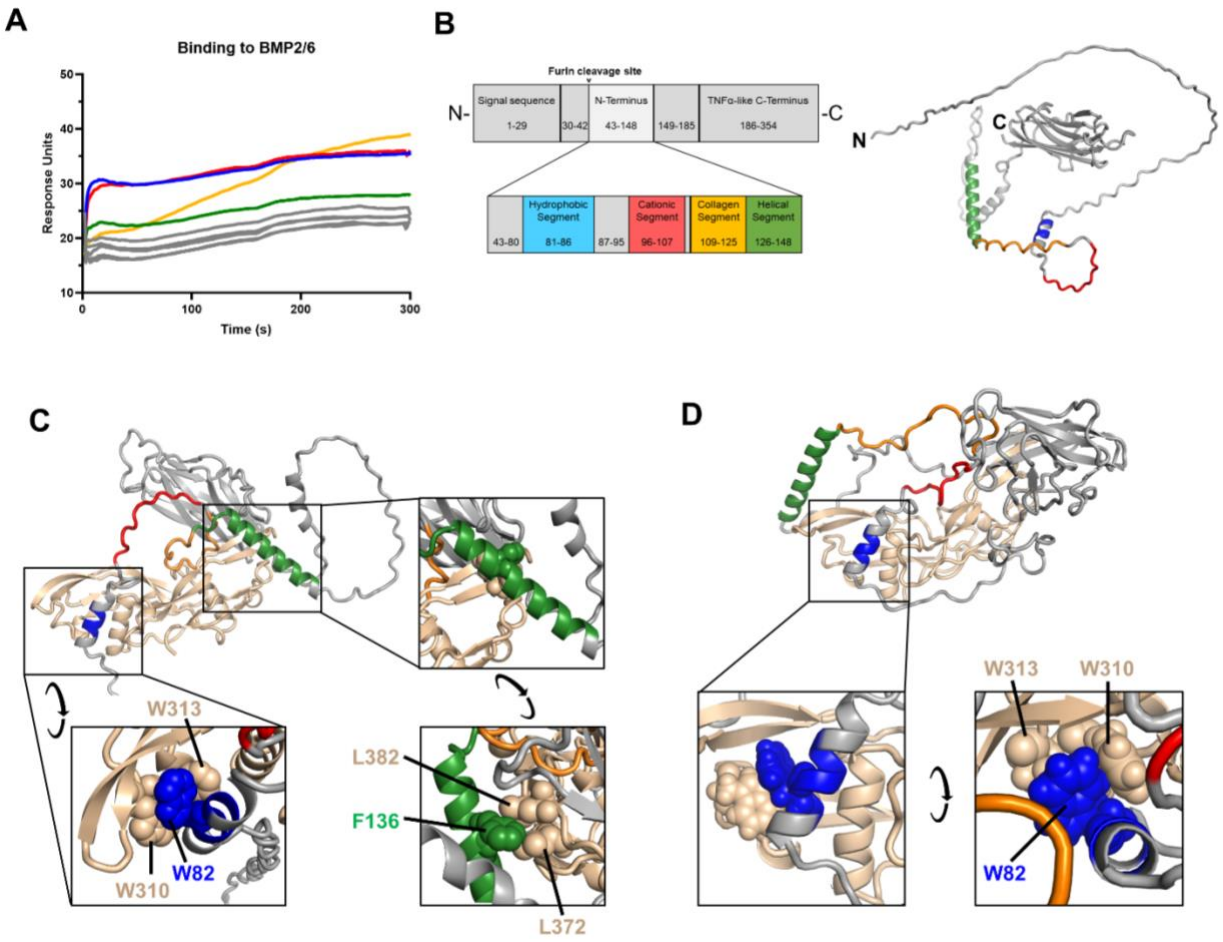

Figure 2: The ERFE N-terminus is comprised of multiple functional segments

(A) Synthetic 18-mer peptides that span the ERFE N-terminus were tested by surface plasmon resonance for binding to BMP2/6. Peptide sequences and color-coding are shown in Figure S-2A. The color corresponds to the specific ERFE structural segments shown in B. (B) Diagram of the ERFE N-terminal structural segments (left) and AlphaFold2 model of ERFE with N-terminal segments indicated by corresponding color (right). (C) AlphaFold2 model of ERFE bound to a BMP2/6 heterodimer colored by segment. Callout boxes show potential interactions using aromatic residues of the ERFE Hydrophobic and Helical Segments. (D) Molecular dynamics refined model of ERFE bound to a BMP2 homodimer. Callout box shows potential interactions involving aromatic residues of the ERFE Hydrophobic Segment.

2.3. The conserved tryptophan in the Hydrophobic Segment is essential for activity

The ERFE vertebrate protein sequence alignment revealed that while a segment very similar to the human ERFE region 81-86 is universally present, only the tryptophan at position 82 (human numbering) is invariable **(Figure 1C)**. To test the function of this segment, we deleted the entire segment (ΔHydrophobic) or introduced a point mutation of this tryptophan to alanine (W82A) **(Figure 3A)**. Both mutants completely lost activity in the hepcidin-suppression assay **(Figure 3B)**, indicating a critical role of the tryptophan residue and the Hydrophobic Segment in ERFE's mechanism of action. Since the tryptophan is predicted by both AlphaFold2 and molecular dynamics refined coordinate set to interact directly with BMPs, we tested how well the W82A mutant binds BMPs. To avoid the confounding effects of ERFE multimerization driven by the TNFα-like globular regions on avidity, we purified bacterially-produced, untagged ERFE N-terminal (43-148) segments—WT and W82A—and measured their binding to BMP2/6, 2, or 6 by SPR **(Figure 3C, S-3A,B)**. The W82A mutant bound BMPs, however its interaction curve showed about 3-fold lower avidity and considerably faster on- and off-rates compared to WT. This implies that strong and persistent binding to BMPs favors the hepcidin-suppressive activity of ERFE.

2.4. Clustered positive charge in the Cationic Segment mediates biological activity and interaction with heparin

We next investigated the Cationic Segment and produced full-length ERFE lacking this region (ΔCationic) **(Figure 4A)**. Like the ΔHydrophobic mutant, the ΔCationic mutant lacks detectable bioactivity **(Figure 4B)**. Despite our SPR finding that the cationic 18-mer peptide that covers this region binds BMPs, neither of our modeling systems predicted a direct interaction of this segment with BMPs, possibly because of constraints imposed by the rest of the protein.

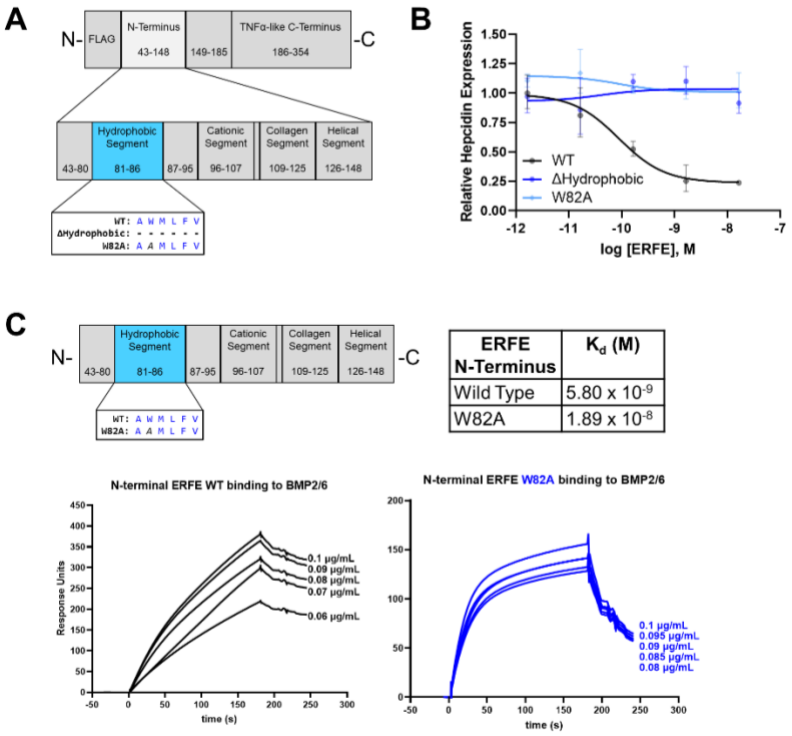

Figure 3: The Hydrophobic Segment of ERFE N-terminus

(A) Diagram of two mutations in the ERFE Hydrophobic Segment used for bioassay: deletion of amino acids 81-86 (ΔHydrophobic) and a single amino acid substitution W82A. (B) qPCR expression of hepcidin in Hep3B cells treated with indicated concentrations of WT, ΔHydrophobic, and W82A ERFE. Data are normalized to untreated controls, N = 3 biological replicates, statistics in Table 2. (C) SPR sensorgrams of ERFE WT and W82A N-terminus binding to BMP2/6, with K_d of each mutant shown on the right, with statistics in Table 1.

We next asked whether the specific sequence rather than the overall cationic character is required for ERFE bioactivity **(Figure 4A)** and generated two additional mutants: the 6KA Mutant changes the six lysines of the domain into alanines, which neutralizes much but not all of the positive charge; and the KR-Switch mutant turns the six lysines into arginines and the two arginines into lysines, retaining the overall charge. Similarly to ΔCationic, the 6KA Mutant lacks hepcidin suppressive activity but the bioactivity of the KR-Switch mutant is comparable to that of WT ERFE **(Figure 4B)**.

To determine which, if any, of the cationic residues is required for hepcidin suppression, we performed alanine scanning through the lysines of the Cationic Segment. Surprisingly, no single alanine substitution had a substantial effect on function. Neutralization of three out of the six lysines was required to impair hepcidin suppression, but the choice of lysines did not appear to be important **(Figure S-4A)**. Thus, overall charge interactions and not individual residues are responsible for the functional contribution of the Cationic Segment.

We next measured the binding of the 6KA Mutant N-terminus to BMP2/6, 2, or 6 **(Figure 4C, S-4B,C)**. The interaction curve shows fast on- and off-rates similar to the W82A mutant which also lacks biological activity, and the KR-Switch mutant binding curve is similar to that of WT **(Figure 4C, S-4D)**.

Based on the sequence of the Cationic Segment, we hypothesized that this region may also function as a heparin-binding domain. Such interactions may be functionally important because the perisinusoidal space (the Space of Disse) where the contact between ERFE and BMPs occurs is particularly rich in sulfated proteoglycans[15], and sulfated proteoglycans have been

strongly implicated in the regulation of iron-related BMP signaling[16,17]. Due to its large number of negatively-charged sulfo and carbonyl groups, heparin has the highest negative charge density of any known biological macromolecule[18], and heparin-binding proteins possess matching positively-charged regions like the Cationic Segment of ERFE to promote their interaction with heparin. We overexpressed full-length ERFE in HEK293T cells and adsorbed it to a HiTrap heparin sepharose affinity column in an FPLC instrument. Elution was performed by an NaCl gradient, and fractions were analyzed by Western blot, with heparin-bound ERFE eluting at about 0.5 M NaCl **(Figure S-5)**, representing a medium-strength binding interaction. ΔCationic eluted at a much lower concentration of NaCl indicative of impaired heparin-binding affinity. The elution pattern of the 6KA Mutant was also impaired similarly to that of ΔCationic. Surprisingly, the KR-Switch mutant bound much stronger to the column than even WT. Our data therefore indicate that positive charge in the Cationic Segment is required for ERFE function and heparin binding.

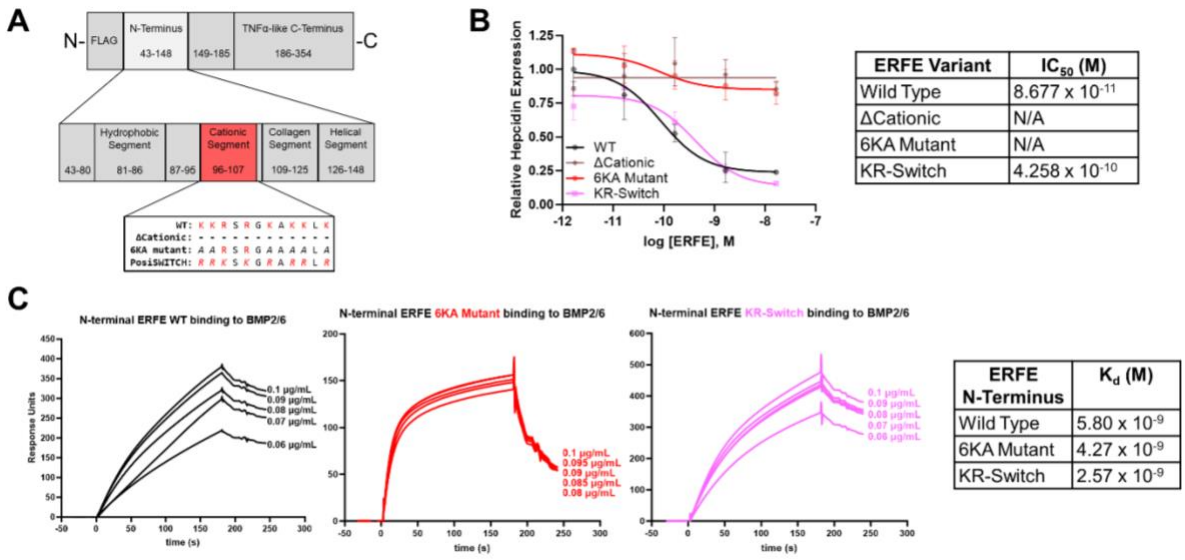

ERFE Variant	IC_{50} (M)
Wild Type	8.677×10^{-11}
ΔCationic	N/A
6KA Mutant	N/A
KR-Switch	4.258×10^{-10}

ERFE N-Terminus	K_d (M)
Wild Type	5.80×10^{-9}
6KA Mutant	4.27×10^{-9}
KR-Switch	2.57×10^{-9}

Figure 4: The Cationic Segment of ERFE N-terminus

(A) Diagram of three mutations in the ERFE Cationic Segment used for biological activity: ΔCationic (deletion of amino acids 96-107); 6KA mutant (substitution of six lysines with alanines); KR-Switch mutant (substitution of six lysines with arginines and two arginines with lysines). (B) qPCR expression of hepcidin in Hep3B cells treated with indicated concentrations of WT, ΔCationic, 6KA Mutant, and KR-Switch ERFE. Data are normalized to untreated controls, N = 3 biological replicates, statistics in Table 2. IC_{50} for hepcidin suppression by each mutant is shown on the right. (C) Surface plasmon resonance of N-terminal ERFE WT, 6KA Mutant, and KR-Switch binding to BMP2/6, with K_d of each mutant shown on the right, with statistics in Table 1.

2.5. The Collagen and Helical Segments make smaller contributions to ERFE bioactivity

We next generated full-length constructs in which the Collagen or Helical Segments were deleted **(Figure 5A)**. When Hep3B cells were treated with these mutants, hepcidin mRNA expression was suppressed to near WT levels but required much higher mutant ERFE concentrations than with the WT form **(Figure 5B** and **Table 2)**, representing more than a 100-fold loss of potency for both ΔCollagen and ΔHelical relative to WT. The avidities of ΔCollagen and ΔHelical for BMPs are comparable to each other and lower than that of WT **(Figure 5C, S-6A,B,C)**. In addition, ΔHelical exhibits comparatively very rapid on- and off-rates.

Collagen-like regions are an important feature of a diverse set of proteins including those found in plasma. Multiple proteins of the CTRP family to which ERFE belongs contain the signature Gly-X-Y repeats, frequently containing proline in the X-position and hydroxyproline in the Y-position[19,20]. The collagen motif in protein multimers forms a triple helix of these domains, although some proteins further assemble into multiples of trimers, such as the collagen hexamer of the C1q subunit of complement[21]. We used AlphaFold2 to generate a model of the full-length mature ERFE trimer **(Figure S-6D)**. Among the top five models, those ranked 1 and 3 show a collagen triple helix with substantial confidence **(Figure S-6F)** but the others do not. The free energies associated with the top five models are very similar which may indicate that the collagen motifs form a triple helix only transiently. We next generated a model of the ERFE trimer bound to a BMP2/6 heterodimer **(Figure S-6E)**. The collagen motif does not form a triple helix in this model, possibly because the ERFE-BMP bound state is more stable than the collagen helix. In summary, the collagen motif may make a small contribution to the forces that favor ERFE trimer formation, but likely does not interact directly with BMPs.

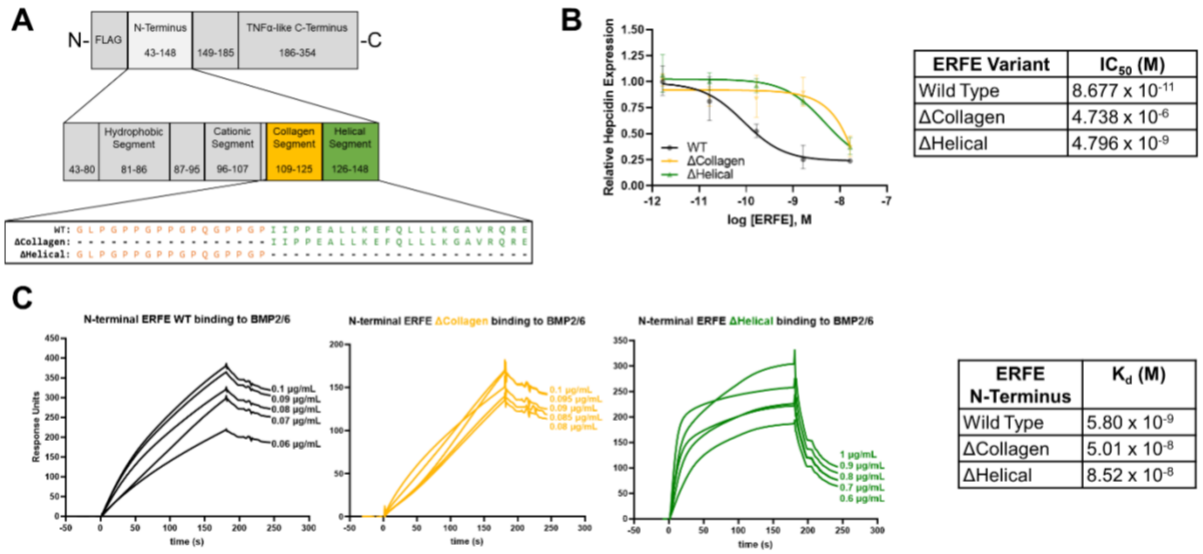

Figure 5: The Collagen and Helical Segments of ERFE N-terminus

(A) Diagram of mutations in the ERFE Collagen and Helical Segments used for bioassays: ΔCollagen (deletion of amino acids 109-125); ΔHelical (deletion of amino acids 126-148). (B) Expression of hepcidin mRNA in Hep3B cells treated with indicated concentrations of WT, ΔCollagen, and ΔHelical ERFE. qPCR generated data are normalized to untreated controls, N = 3 biological replicates per point, statistics in Tables 1 and 2. IC_{50} for hepcidin suppression by each mutant is shown on the right, with statistics in Table 2. (C) Surface plasmon resonance sensorgrams of N-terminal ERFE WT, ΔCollagen, and ΔHelical binding to immobilized BMP2/6, with K_d of each mutant shown on the right, with statistics in Table 1.

2.6. ERFE and BMP receptors bind BMPs in a similar manner

We sought to compare the nature of the ERFE-BMP interaction with other proteins that bind BMP molecules, the BMP receptors themselves. Crystallographic analyses have elucidated the interaction between BMPs and their receptors[22]. BMP dimers form two symmetrical binding grooves, between the α-helix wrist of one molecule and the β-sheet fingers of the other. In the crystal structure of BMP2 bound to type I BMP receptor ALK3, the aromatic residue F108 of the receptor appears to associate with two tryptophan residues of BMP2 (W310 and W313) in one of the BMP binding grooves **(Figure 6A)**. Remarkably, the same two tryptophans are shown interacting with the key W82 of ERFE in our AlphaFold2 docking model **(Figure 6B)**. Both tryptophan and phenylalanine have hydrophobic aromatic sidechains. This feature is likely crucial to binding since the ERFE W82A substitution ablated bioactivity **(Figure 3B)** and weakened binding considerably **(Figure 3C)**. Thus, the BMP-ERFE binding interaction appears to mimic the binding of BMPs to their cognate receptors.

To test whether ERFE can directly compete with BMP receptors for binding to BMPs, we employed an SPR-based competition assay and assessed binding of both BMP2 and BMP6. In this experiment, BMPs alone or mixed with WT or W82A ERFE N-terminal segments were tested for binding to immobilized extracellular portions of BMP receptors ALK2 (Activin RIA), ALK3 (BMPR IA), Activin RIIA, Activin RIIB, and BMPRII **(Figure 6C, S-7)**. WT ERFE dose-dependently interfered with BMP binding to receptors. The W82A mutant, however, competed less effectively, consistent with our bioactivity data.

The ERFE Hydrophobic Segment contains a second aromatic residue, F85. We speculated that ERFE may use its W82 and F85 to emulate the W-X-X-W motif in BMP molecules and bind

directly to BMP receptors—a possible secondary mechanism for blocking activation of the BMP-SMAD pathway. However, the WT ERFE N-terminal segment did not bind to any of the five BMP receptors tested **(Figure 6D)**.

In addition to contact with the W-X-X-W motif, the interaction surface of BMPs with Type II BMP receptors includes a contact between two receptor phenylalanines and two BMP leucines, L372 and L382[23]. Our AlphaFold2 model of BMP dimer interaction with an ERFE monomer indicates that ERFE F136 interacts with the same L372 and L382 **(Figure 2C)** as a potential additional interaction that may help ERFE compete with type II receptors for BMP binding. However, this interaction was not visible in Alphafold2 models of ERFE multimers interacting with BMPs, which appear to be dominated by the interaction of the Hydrophobic Segment with the BMP groove (see further results).

2.7. Charge interactions facilitate ERFE multimerization

Proteins in the CTRP family are known to multimerize. In the case of adiponectin, the distinct oligomeric forms have been shown to exhibit differential activities[24–26]. We wondered if mutations in the ERFE N-terminus could affect multimerization, and if so, if these changes might further explain the effects of mutations on ERFE bioactivity. We used native PAGE Western blotting to analyze a dilution series of ERFE-containing supernatant produced by HEK293T cells **(Figure 7A)**. At high concentrations, the ERFE band appears as a large smear between 117 kDa and 460 kDa molecular weight markers. At lower concentrations, a dominant band can be seen at an estimated mass of 260 kDa, corresponding to a hexamer.

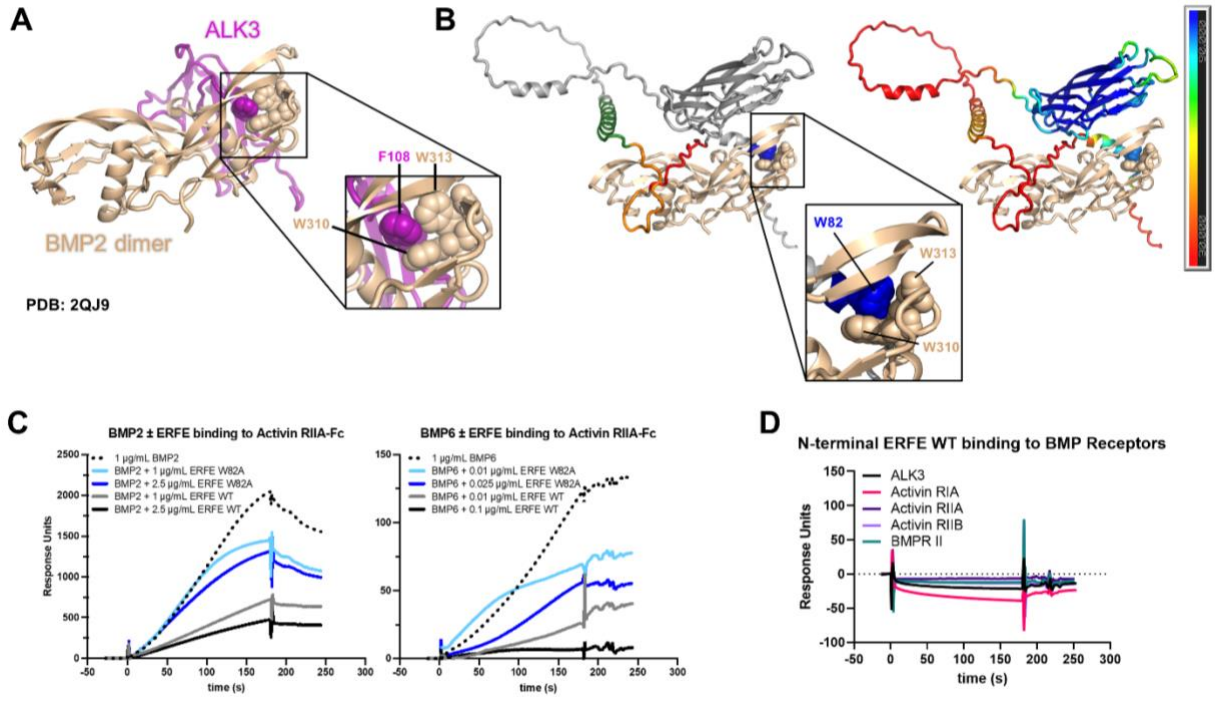

Figure 6: ERFE and BMP receptors bind BMPs in a similar manner

(A) Crystallography-resolved structure of BMP2 homodimer bound to ALK3 (PDB: 2QJ9). Callout box enlarges the interaction and identifies the contacting residues. (B) AlphaFold2 model of a BMP2 homodimer (tan color) bound to ERFE colored by segment (left) and confidence pLDDT (right). Callout box shows the analogous interaction that BMPs have with their receptors. (C) Surface plasmon resonance sensorgrams of competition between WT ERFE, W82A ERFE, and Activin RIIA for BMP2 (left) and BMP6 (right) binding. Extracellular portions of Activin RIIA were immobilized, and BMP analyte flowed over alone or mixed with WT or W82A ERFE N-terminal segments. (D) Surface plasmon resonance of the ERFE N-terminus binding to extracellular portions of five BMP receptors.

We used this non-reducing, non-denaturing native PAGE to analyze the multimeric structures formed by ERFE mutants used in our bioassay **(Figure 7B, top)**. Most of the mutants tested formed a similar smear as WT with a prominent hexamer band. In constructs with larger deletions, this band was appropriately shifted down. Interestingly, the ΔCationic and 6KA Mutants differed from the others, forming two discrete bands that appeared to be the size of a trimer. The distinct multimerization pattern in these mutants may explain why they lack biological activity despite the binding strength of the monomeric N-terminal segment 6KA Mutant to BMPs being comparable to that of WT **(Figure 4B,C)**. The unique banding pattern of these two mutants is confirmed to be due to differences in multimerization since the reduced, denatured forms all migrate at the same apparent size **(Figure 7B, bottom)**.

In addition to these mutations in the Cationic Segment, other amino acid substitutions in the N-terminus have been previously shown to disrupt high order oligomer formation[10]. To determine if this portion of the molecule alone is capable of forming multimers or if the C-terminal head is required, we analyzed N-terminal ERFE samples by native and denaturing PAGE **(Figure 7C)**. WT and all mutants resolve to roughly equal molecular weights in both cases, indicating that the N-terminal segment is not sufficient for multimer assembly.

Based on the estimated size of dominant ERFE multimer, we next used AlphaFold2 to model the ERFE hexamer **(Figure 7D)**. The structure resembles a dimer of trimers with interactions between the trimeric TNFα-like heads. Only the globular head region is predicted with high confidence **(Figure S-8A)**. Additionally, we generated a hexamer model bound to three BMP2/6 dimers **(Figure 7E)**. This model shows consistent interactions of the N-terminal Hydrophobic Segments of ERFE with the BMP dimers but unlike in the monomeric ERFE interaction with

BMP dimers, the Helical Segment does not make contact here. The ERFE TNFα-like heads and Hydrophobic Segments that are in contact with the BMPs are predicted with the highest confidence **(Figure S-8B)**.

Our data therefore indicate that full-length ERFE produced by human cells *in vitro* is predominantly a hexamer, that the Cationic Segment of ERFE is required for this multimerization, but that the N-terminal domain is not sufficient for the multimerization. Although multimerization greatly increases the avidity of ERFE for its BMP ligand by decreasing the off-rate, multimerization is not strictly required for bioactivity since the monomeric N-terminal domain by itself suppresses hepcidin at similar molar concentrations, at least under the greatly simplified *in vitro* conditions.

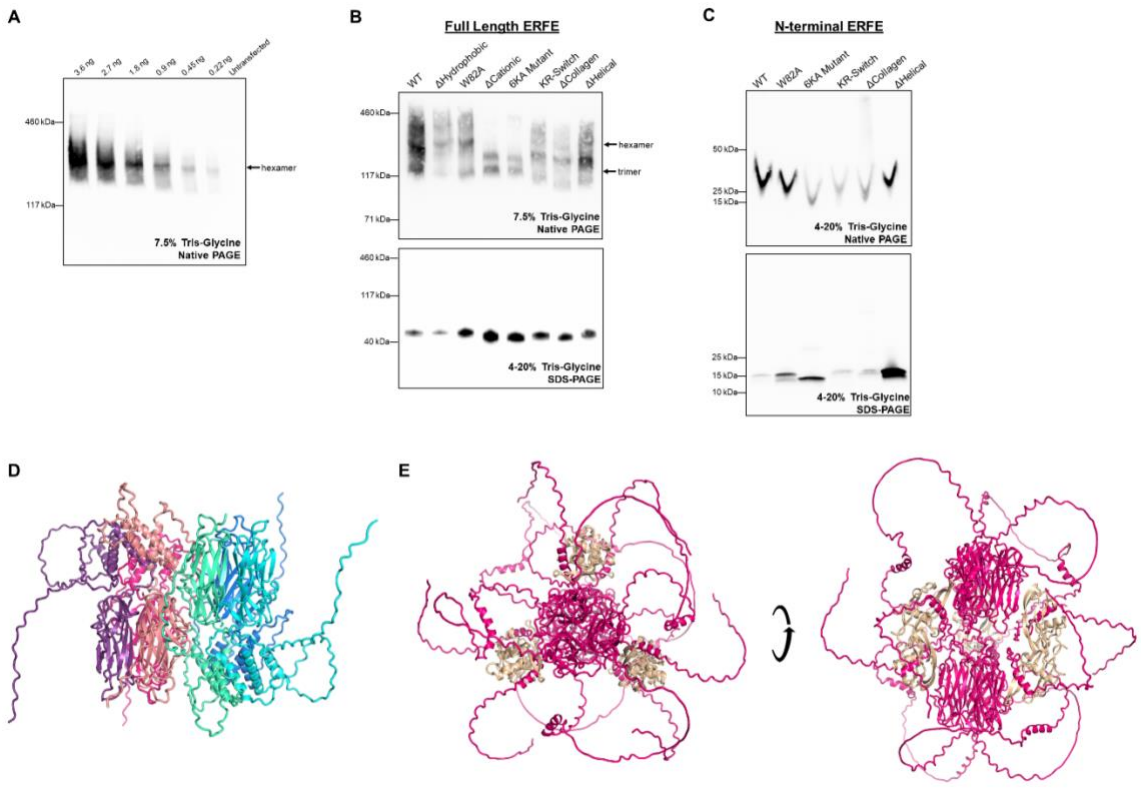

Figure 7: Charge interactions facilitate ERFE multimerization

(A) Dilution series of WT ERFE containing supernatant produced in HEK293T cells revealing the hexamer as the dominant species. (B) Native (top) and denaturing (bottom) Western blots of full-length ERFE WT and mutants showing differential multimerization patterns. (C) Native (top) and denaturing (bottom) Western blots of WT and mutant N-terminal ERFE segments produced in bacteria showing a lack of multimerization. Under native running conditions, SDS which is present only in the sample dye runs unevenly through the gel at low molecular weight, causing distortion of the bands. All Western blots in A and B were probed with anti-FLAG HRP. Blots in C were probed with anti-ERFE. (D) AlphaFold2 docking of hexameric human ERFE colored by chain. (E) AlphaFold2 docking of hexameric human ERFE bound to three BMP2/6 dimers. All ERFE chains are colored magenta, with BMP dimers in cyan-green.

2.8. Truncating the N-terminal domain reverses the activity of erythroferrone

In an effort to identify the minimal region necessary for ERFE function, we used peptide synthesis to produce 53-mer peptides covering the first (amino acids 43-95) and second (96-148) halves of the active N-terminal domain (Segments 1 and 3, respectively), as well as Segment 2 which spans the middle portion of N-terminus (73-125) **(Figure 8A)**. Surprisingly, we found that treatment with either Segment 2 or Segment 3 not only did not suppress hepcidin but did the opposite and increased hepcidin expression in Hep3B cells. Segment 1 had neither a stimulatory nor inhibitory effect on hepcidin transcription **(Figure 8B)**. We found that the induction of hepcidin by Segments 2 and 3 was caused by increased SMAD signaling, as ID1 expression, another BMP-SMAD target gene, was also increased **(Figure S-9A)**. Activation of inflammation can also drive hepcidin, but this pathway was ruled out as mRNA expression of the inflammatory marker serum amyloid A1 was not increased and was below the threshold of our qPCR detection. Next, we tested the binding of the peptide segments to BMP receptors by SPR to rule out the possibility that these segments activate the SMAD pathway directly as receptor agonists. Like the complete N-terminus, these fragments do not associate with any BMP receptor tested **(Figure 8C, S-9B)**. We then measured the binding of these segments to BMPs. Segments 2 and 3 bound **(Figure 8D, S-9C,D)**, however the binding was more than 1,000-fold weaker than the complete N-terminus and almost 30,000-fold weaker than the full-length protein **(Figure 1E** and **Table 1)**. Segment 1 did not bind any BMP (not shown).

Our data therefore indicate that while the entire N-terminal domain (43-148) is required for its suppressive effect on BMP signaling, low affinity BMP binding by its segments may paradoxically facilitate BMP-SMAD signaling.

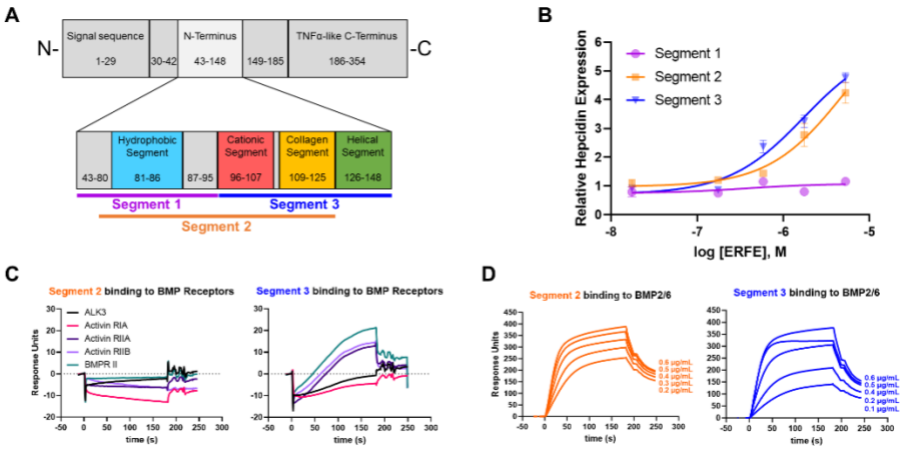

Figure 8: Truncating the N-terminal domain reverses the activity of erythroferrone

(A) Diagram of generated synthetic segments of the ERFE N-terminus. (B) qPCR expression of hepcidin in Hep3B cells treated with indicated concentrations of N-terminal ERFE segments. Data are normalized to untreated controls. N = 3 biological replicates, statistics in Tables 1 and 2. (C) Surface plasmon resonance sensorgrams of N-terminal ERFE Segments 2 (left) and 3 (right) binding to BMP receptors. (D) Surface plasmon resonance sensorgram of N-terminal ERFE Segments 2 (left) and 3 (right) binding to BMP2/6.

3. **Discussion**

In this study, we confirmed that the bioactivity of erythroferrone depends on the N-terminal domain of the protein[9,27], and proceeded to examine the specific structural features that determine ERFE bioactivity. We identified four evolutionarily conserved features within the N-terminal domain and designated them as Hydrophobic, Cationic, Collagen, and Helical Segments. Each short linear domain demonstrated BMP-binding activity on our SPR screen, indicating possible relevance to the mechanism of action. Two independent protein docking algorithms (Alphafold2 and molecular dynamics) predicted direct contact of the W82-containing Hydrophobic Segment of ERFE with a specific moiety of BMP, and both algorithms also predicted interaction at the Helical Segment. Neither model found an interface between the Cationic or Collagen Segments of ERFE and the BMP molecule, despite the implications of our SPR data with linear 18-mer peptides, presumably because in contrast to the linear peptides, the folded full-length protein has buried residues and greater spatial constraints.

In our docking models, the ERFE tryptophan W82 appears to insert between two BMP tryptophans—a state that may be stabilized by hydrophobic or electrostatic forces. We found the ERFE W82 to be essential to its functioning, as mutation to an alanine abolished all activity. The interaction of this key tryptophan is reminiscent of other natural BMP-binding proteins: Type I BMP receptors and certain antagonists such as noggin. In the case of BMP receptors, hydrophobic and aromatic residues like tryptophan, tyrosine, and phenylalanine form critical bonds with hydrophobic BMP side chains. The exact combination of BMP and receptor residues differs depending on the pairing, and these differences strengthen specificity[28]. The BMP antagonist noggin binds BMP7 by inserting a proline residue into a hydrophobic BMP pocket formed by the W-X-X-W motif[29], consistent with our ERFE findings here.

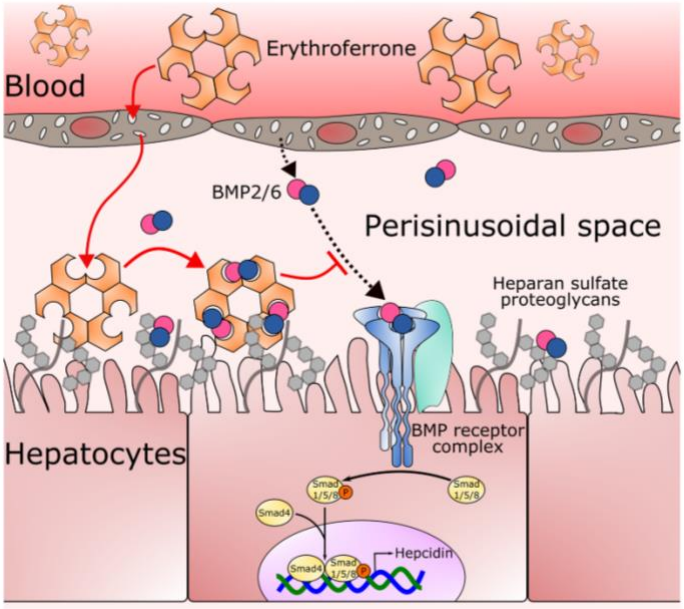

Figure 9: Model of ERFE function in vivo

Circulating erythroferrone diffuses into the perisinusoidal space through fenestrations in liver sinusoidal endothelial cells. Within the perisinusoidal space, ERFE may bind to heparan sulfate proteoglycans to localize to the surface of hepatocytes and bind BMP molecules. This prevents BMP binding to BMP receptors, and results in lower BMP-SMAD signaling, and decreased hepcidin transcription. Figure[27] modified with permission.

Like ERFE, noggin is a heparin-binding protein and is thought to bind heparan sulfate proteoglycans on cells, trapping BMPs at the surface. Interestingly, heparin binding by noggin appears to be independent of its BMP antagonist activity, as a mutant lacking the heparin domain continued to bind BMPs and inhibit BMP signaling in cells[30]. Our measurements by SPR indicate that, like noggin, deletion or partial charge neutralization of the Cationic Segment had no effect on BMP-binding affinity, although the on- and off-rates differed from WT. This may be evidence that BMP binding is necessary but not sufficient for full physiological antagonist activity. Unlike with noggin, these mutations in ERFE ablated hepcidin-suppressing activity, possibly by favoring a shift to a less avid multimerization state. We found the clustered positive charge in the Cationic Segment but not the specific amino acid sequence to be essential for BMP-binding, bioactivity, and multimer assembly since complete K-R exchange in this segment preserved all three functions. The cationic charge of this ERFE region also mediates heparin-binding activity whose function is not yet clear. Like with noggin, it may localize BMP-trapping activity to specific cell types or extracellular spaces with high concentrations of heparin-like molecules. For plasma ERFE, the main site of bioactivity is the hepatic perisinusoidal space (the Space of Disse), known to be enriched in sulfated proteoglycans[15], and sulfated proteoglycans have been strongly implicated in the regulation of iron-related BMP signaling[16]. It is therefore possible that the Cationic Segment of ERFE allows preferential accumulation of this hormone in the proteoglycan-rich perisinusoidal space.

We noted that the deletion of the Collagen Segment from ERFE resulted in low yield of ERFE in the supernatant, an observation also made by others who found that retention within the cell of an immature form of ERFE is responsible for the lower yield[10]. The removal of the Collagen Segment also decreased ERFE potency to suppress hepcidin transcription. Structurally, the

Collagen Segment may promote trimerization by forming a triple helix, but our models suggest that this structure is not formed after the trimer binds its BMP ligand.

Similarly, the deletion of the Helical Segment had a relatively minor impact on ERFE bioactivity. Our modeling indicates a possible but weak interaction between BMP and ERFE at this site. Such an interaction may be more favored in ERFE monomers or isolated N-terminal segments, as the contact is not present in models of higher order multimers. In any case, its contribution to bioactivity is markedly less than that of the W82-containing Hydrophobic Segment. It is interesting to note that the synthetic N-terminal ERFE segment lacking the Helical Segment but retaining the other conserved sections (Segment 2) had greatly decreased affinity for BMPs and manifested hepcidin-inducing bioactivity. Perhaps the contributions to antagonism of some individual features are small or partially redundant in the context of the full protein but become larger when part of shorter peptides. In support of this hypothesis, Segment 3 which similarly contains three out of four N-terminal segments likewise increases hepcidin transcription. When BMP binding capacity was measured in these segments, we found that the strength of association was many-fold less than even inactive ERFE mutants. This relatively weak micromolar binding may be responsible for the switch in activity compared to full-length and N-terminal ERFE. Full-length ERFE acts as a strong trap for BMPs, with its picomolar binding avidity on par with or stronger than the binding between BMPs and receptors[31]. While sometimes weaker than the WT protein, many of our mutants retain sufficiently strong binding to maintain antagonist activity. However, the binding between BMPs and Segments 2 or 3 is weaker than the native interaction between BMPs and their receptors, but possibly stronger than nonspecific interactions of BMPs with other molecules in the environment. Thus, these weaker-binding ERFE segments could act as agonists by chaperoning BMPs to their

physiological receptors.

In summary, we provide evidence for key structural features of ERFE that mediate its function **(Figure S-10)**, allowing it to couple erythropoiesis to iron supply by inhibiting BMP signaling required for the transcription of the iron-regulatory hormone hepcidin. The ability of ERFE to bind and inactivate BMPs is mediated in part by a key hydrophobic/aromatic interaction centered on the region around ERFE W82 interacting with the W-X-X-W motif in BMP molecules, similarly to the interaction that facilitates the binding of the ALK3 receptor to the same region of BMPs. We identified additional regions of the relatively unstructured ERFE N-terminal domain that make detectable contributions to binding BMPs **(Figure S-10)**. We also showed that the multimeric nature of ERFE, driven both by interaction of TNFα-like C-terminal globular domains and by several features of the N-terminal domain, greatly increases the avidity of ERFE binding to BMPs by dramatically decreasing the off-rate of the binding. Finally, the heparin-binding activity mediated by the Cationic Segment in the N-terminal domain may help localize ERFE to its likely site of bioactivity: the perisinusoidal space rich in sulfated proteoglycans **(Figure 9)**. Our structure-function study of ERFE may help inform the design of new therapeutics targeting ERFE or BMPs for the treatment of iron disorders.

4. **Experimental Procedures**

4.1 Cell culture

Hep3B cells were obtained from the American Type Culture Collection (ATCC #HB-8064) and cultured in DMEM (ThermoFisher #10564029) supplemented with 10% FBS (Genesee Scientific #25-514H) and 1% Pen/Strep (ThermoFisher #15070063). Cells were kept in a humidified incubator at 37°C with a 5% CO_2 atmosphere.

4.2 Erythroferrone plasmid construction

For mammalian expression, FLAG-tagged full-length human erythroferrone (43-354) was cloned into the pcDNA3.1(+) backbone (Invitrogen #V790-20) by restriction enzyme cloning. For bacterial expression, the N-terminus (43-148) of ERFE was codon-optimized for prokaryotes and synthesized as a double-strand gene block by Integrated DNA Technologies. The coding sequence was cloned into the 2M-T backbone (Addgene plasmid #29708) using In-Fusion HD (Takara #639650). The result was a TEV-cleavable N-terminal His6-MBP fusion protein. Deletions and mutations were introduced into both plasmid types by round-the-horn cloning using CloneAmp HiFi PCR premix (Takara #639298). Sequences were verified by Sanger sequencing.

4.3 Erythroferrone supernatant production and quantification

Supernatants containing erythroferrone variants were produced in HEK293T cells by transient transfection of the appropriate plasmid using Lipofectamine 3000 (ThermoFisher #L300000) according to the manufacturer's instructions. One day after transfection, the cells were washed and the media was replaced with Opti-MEM (ThermoFisher #51985034). Supernatants were collected 72 hours later, aliquoted, and stored at -80°C until use.

ERFE concentrations in supernatants were determined by Western blot for FLAG using known amounts of recombinant human His10-FLAG-BRD4 (RND Systems #SP-600) as a standard. Standards and samples were separated by SDS-PAGE and transferred to nitrocellulose membranes. Membranes were blocked in 5% w/v nonfat dry milk in TBS with 0.1% Tween-20 and incubated with monoclonal anti-FLAG M2 HRP antibody (Sigma #A8592) at a dilution of

1:20,000 in milk. Blots were visualized by chemiluminescence using the ChemiDoc imaging system and quantified using Image Lab software (Bio-Rad). The apparent size of His10-FLAG-BRD4 on the gel is about 20% larger than ERFE, so an adjustment constant of 0.81 was applied to the ERFE variants in calculating their concentrations.

4.4 Gene expression quantification by RT-qPCR

Hep3Bs were treated overnight in a 1:1 mixture of DMEM:Opti-MEM media containing 5% serum and a dilution series of ERFE. After treatment, cells were lysed in TRIzol Reagent (ThermoFisher #15596018), and total RNA was isolated by chloroform extraction per the manufacturer's instructions. Five hundred nanograms of RNA was reverse-transcribed using the iScript cDNA Synthesis Kit (Bio-Rad #1708891). Quantitative real-time PCR was performed on cDNA using SsoAdvanced SYBR Green Supermix (Bio-Rad # 1725275) on the CFX Real-Time PCR Detection System (Bio-Rad). Samples were measured in technical duplicates, and target genes were normalized to HPRT. Primer sequences are provided in Table 3.

4.5 Expression and purification of N-terminal ERFE for surface plasmon resonance

Expression plasmids containing MBP-fusion proteins were transformed into Rosetta2(DE3)pLysS cells and plated onto ampicillin+chloramphenicol LB-agar plates. Starter cultures of 50 mL were inoculated with single colonies and incubated overnight at 200 rpm and 37°C. In the morning, 1 L of LB with antibiotics was inoculated with the starter culture and allowed to grow to OD_{600} = 0.6-0.8 (mid-log phase). IPTG (GoldBio #I2481) was added to a final concentration of 1 mM, and the cultures were incubated for an additional 4-6 hours. Cultures were spun down, the pellets were washed with PBS and stored at -80°C until purification.

For purification, cell pellets were freeze-thawed three times between 37°C and -80°C and resuspend in 5X volume bacterial lysis buffer (PBS + 0.1% Tween-20 + 1% Trition X). Samples were homogenized by Dounce and then sonicated on ice 10 seconds on and 10 seconds off for 1 minute. Lysates were then cleared at 25,000 x g for 1 hour at 4°C. Lysate pH was adjusted to pH 8 with NaOH and imidazole was added to a final concentration of 10 mM. Lysates were incubated with HisPur Ni-NTA (ThermoFisher #88221), washed and eluted with PBS-based imidazole buffers. Purification was monitored by Imperial Protein Stain (ThermoFisher #24615) on an SDS-PAGE gel of samples taken throughout the process. Appropriate fractions were pooled and concentrated in 30K Spin-X UF molecular weight cutoff concentrators (Corning #431484) overnight at 4°C. The next day, samples were incubated with homemade TEV protease and reaction buffer (50 mM Tris-HCl, 0.5 mM EDTA, 1 mM DTT) at 4°C for 72 hours. Cleaved His-MBP tag and added TEV protease were both removed via reverse IMAC, leaving the purified ERFE in the flowthrough. ERFE was quantified by Imperial Protein Stain on an SDS-PAGE gel and stored in 40% ethylene glycol at -20°C.

4.6 N-terminal ERFE small and large peptide generation

18-mer peptides spanning the N-terminus of human erythroferrone used for SPR along with 53-mer peptides (Segments 1-3) were all synthesized by GenScript at ≥70% purity. All peptides were resuspended to 10 mg/mL with sterile H_2O and frozen at -20°C. Segments 1-3 were thawed and briefly sonicated in a sonicating water bath before use.

4.7 Determination of binding affinities by surface plasmon resonance

Proteins were immobilized on CM5 chips using a Biacore T200 instrument by amine coupling per the manufacturer's instructions, using reagents (N-hydroxysuccinimide, 1-ethyl-3-(3-

aminopropyl)carbodiimide hydrochloride, and ethanolamine hydrochloride) purchased from Cytiva. The analyte buffer, HBS-EP, contained 0.15 M NaCl, 3 mM EDTA, 0.005% (v/v) surfactant P20, and 0.01 M HEPES (pH 7.4). Binding was monitored at 1-s intervals for 5 min with an analyte flow rate of 50 µL/min. Dissociation was monitored at 1-s intervals for 2–4 min. The sensor chips were regenerated by washing with 10 mM HCl, and (if needed) 10 mM NaOH. For the SPR competition assay, Activin RIIA-Fc (#340-RC2-100), BMPRIA/ALK3-Fc (#2406-BR-100), BMPRII-Fc (#811-BR-100), Activin RIA/ALK2-Fc (#637-AR-100), Activin RIIB-Fc (#339-RB-100/CF), human IgG1-Fc for control (#110-HG-100), BMP2/6 (#7145-BP-010/CF), BMP2 (#355-BM-010/CF), and BMP6 (507-BP-020/CF) were all obtained from RND Systems. Data analysis was performed using BIAevaluation 4.1 software from Biacore and GraphPad Prism.

4.8 Erythroferrone multimerization analysis

Samples were mixed with 6X non-reducing SDS loading buffer (Boston BioProducts #BP-111NR) and separated on 7.5% tris-glycine gels (Bio-Rad #4561024). Electrophoresis and transfer were both carried out using a tris-glycine native buffer lacking both SDS and methanol (ThermoFisher #LC2672). After transfer, the nitrocellulose membranes were blocked, probed, and developed as described above. For the untagged N-terminal segments, we used monoclonal rabbit primary antibody against ERFE mAb #9 at 1:1000 that we previously developed for the detection of human serum ERFE by ELISA[32]. HRP-conjugated anti-rabbit IgG (Cell Signaling Technology #7074) was used at 1:5000 as secondary.

4.9 Erythroferrone modeling and docking by AlphaFold2

To model ERFE structures with or without interacting BMP, we used ColabFold v1.5.2: Alphafold2-multimer using MMseqs2 software on Google Colab Pro server, as described[33,34].

The template mode was none, the number of recycles was 20, the number of seeds (num_seeds) was 1, and the sequence alignment mode (msa_mode) was mmseqs_uniref_env. Amber relaxation was not used. The top ranking PDB file was displayed using Pymol 2.5.3 (Schrodinger, LLC). BMP numbering is based on the full, unprocessed sequence including pro-protein elements. UniProt accession numbers: BMP2 (P12643), BMP6 (P22004).

4.10 Prediction of erythroferrone molecular complexes using neural network assisted docking and structural refinement with molecular dynamics (Charmm)

The initial structures for the protein complexes were determined using artificial intelligence (AI), neural network – machine learning based approach with AlphaFold[34,35]. The AlphaFold program was run through the Chimera X (version 1.5) molecular modeling system environment[36] available at https://www.cgl.ucsf.edu/chimera/docs/relnotes.html. These initial predicted protein complex structures were then refined using molecular dynamics to provide a more accurate representation of the complex in aqueous environments.

The protein complex was uploaded to the Charmm Solution Builder (http://www.charmm-gui.org)[37–39] and placed into a rectangular 120.0 x 120.0 x 120.0 Å simulation box with the protein complex positioned at 10 Å from the edge of the box. The system then was hydrated with TIP3 waters[40] and potassium and chloride ions were then added to render the ensemble electrically neutral. The simulation box was then downloaded from the Charmm GUI website server using the Gromacs simulation option to set up the system for the equilibration and production runs. Molecular dynamic simulations were carried out using the Charmm 36m all atom force field implementation for aqueous solvents and proteins in the Gromacs (Version 2022.4) environment (http://www.gromacs.org). The system was first minimized using a steepest descent strategy followed by a six-step equilibration process at 311 K for a total of 500 ns. This included both NVT (constant number, volume, temperature) and NPT (constant

number, pressure, temperature) equilibration phases to allow water molecules to reorient around the lipid headgroups and any exposed parts of the peptide, as well as permitting lipids to optimize their orientation around the peptide. Equilibration protocols employed a PME (Particle Mesh Ewald) strategy for Coulombic long-range interactions and Berendsen temperature coupling. A Berendsen strategy was also used for pressure coupling in a semi-isotropic mode to emulate bilayer motion. After equilibration, the system was subjected to a dynamics production run at the same temperature using the Nose-Hoover protocol and pressure (Parrinello-Rahman) values used in the pre-run steps The Verlet cut-off scheme was employed for all minimization, equilibration, and production steps. Detailed script and parameter files for this solution simulation were generated by the Charmm-GUI website: (http://www.charmm-gui.org). The output of the production run simulations was analyzed with the Gromacs suite of analysis tools. The coordinates for the lowest energy conformers of the protein complexes as well as detailed dynamics refinement protocols are in the Supplemental Materials.

4.11 Statistical analysis

Gene expression data are presented as XY plots with symbols indicating the geometric mean, and the error bars indicating geometric standard deviation. Surface plasmon resonance data are presented as single-point XY plots with points recorded at 1-second intervals. Table 1 contains log association constants log Ka analyzed from n = 5 plasmon resonance curves using Biacore statistical package and presented as mean ± standard deviation of log Ka. Table 2 contains means and 90% confidence limits calculated from sigmoid nonlinear fits to dose response data (n = 3 biological replicates per data point). Statistical analysis was performed using GraphPad Prism (San Diego, CA).

Table 1. ERFE-BMP equilibrium dissociation constant (K_d) and log association constant (log K_a, mean ± SD)

	BMP2/6	**BMP2**	**BMP6**
Full Length	2.77×10^{-10} M 9.6 ± 0.3	4.45×10^{-10} M 9.5 ± 0.4	8.17×10^{-10} M 9.5 ± 0.6
N-Terminus (mammalian)	5.38×10^{-9} M 8.3 ± 0.2	7.84×10^{-9} M 8.1 ± 0.2	5.46×10^{-9} M 8.3 ± 0.3
N-Terminus (bacterial)	5.8×10^{-9} M 8.3 ± 0.2	3.41×10^{-8} M 7.5 ± 0.1	2.49×10^{-8} M 8.8 ± 0.4
W82A	1.89×10^{-8} M 7.7 ± 0.1	8.99×10^{-8} M 7.1 ± 0.2	1.84×10^{-7} M 6.7 ± 0.1
6KA Mutant	4.27×10^{-9} M 8.37 ± 0.02	2.42×10^{-7} M 6.62 ± 0.04	6.56×10^{-9} M 8.2 ± 0.1
KR-Switch	2.57×10^{-9} M 8.6 ± 0.1	5.04×10^{-8} M 7.3 ± 0.2	1.84×10^{-9} M 8.8 ± 0.2
ΔCollagen	5.01×10^{-8} M 7.30 ± 0.03	3.13×10^{-9} M 8.7 ± 0.5	7.56×10^{-10} M 9.2 ± 0.2
ΔHelical	8.52×10^{-8} M 7.1 ± 0.3	7.50×10^{-8} M 7.1 ± 0.2	1.16×10^{-7} M 7.0 ± 0.1
Segment 1	no binding	no binding	no binding
Segment 2	6.61×10^{-6} M 5.2 ± 0.3	1.96×10^{-6} M 5.8 ± 0.4	1.67×10^{-7} M 6.78 ± 0.01
Segment 3	7.75×10^{-6} M 5.4 ± 0.6	1.48×10^{-5} M 4.9 ± 0.3	5.03×10^{-7} M 6.4 ± 0.3

4.12 Table 2. Bioactivity Assays: summary of ERFE IC_{50} (90% confidence limits) values

ERFE Variant	IC_{50}
WT	89 pM (29-229)
∆Hydrophobic	inactive
W82A	inactive
∆Cationic	inactive
6KA Mutant	inactive
KR-Switch	426 pM (213-860)
∆Collagen	10 nM (3-20)
∆Helical	5 nM (2-11)

4.13 Table 3. Human RT-qPCR Primers

Gene	Forward 5' – 3'	Reverse 5' – 3'
HPRT	GCCCTGGCGTCGTGATTAGT	AGCAAGACGTTCAGTCCTGTC
HAMP	GACCAGTGGCTCTGTTTTCC	AGATGGGGAAGTGGGTGTCT
ID1	TCAACGGCGAGATCAGCG	CTTCAGCGACACAAGATGCG
SAA1	GAGCACACCAAGGAGTGATTT	GAAGCTTCATGGTGCTCTCT

5. **Data Availability**

All data are contained within the article and its supporting information.

6. **Supporting Information**

This article contains supporting information.

7. Conflict of Interest

TG and EN are shareholders and scientific advisors of Intrinsic LifeSciences and Silarus Therapeutics, and consultants for Ionis Pharmaceuticals, Protagonist, Disc Medicine, and Vifor. TG is a consultant for Akebia. Other authors declare that they have no conflicts of interest with the contents of this article.

8. Acknowledgments

We thank Mark Arbing and the UCLA Protein Expression Technology Core for fractionating samples by FPLC for the heparin-binding analysis. We also thank Thomas Thompson and Jacob Mast at the University of Cincinnati for several helpful discussions. The content is solely the responsibility of the authors and does not necessarily represent the official views of the National Institutes of Health.

9. Author Contributions

Conceptualization and formal analysis: DNS, EN, and TG. Investigation: DNS, GJ, AJW, and TG. Methodology: DNS, GJ, AJW, EN, and TG. Writing—original draft: DNS. Writing—review and editing: GJ, AJW, EN, and TG. Supervision: EN and TG. Funding acquisition: DNS and TG. Project administration: TG.

10. Funding Information

This study was supported by the National Institutes of Health grant R01 DK126680 (TG) and training grants TL1 DK132768 & U2C DK129496 (DNS).

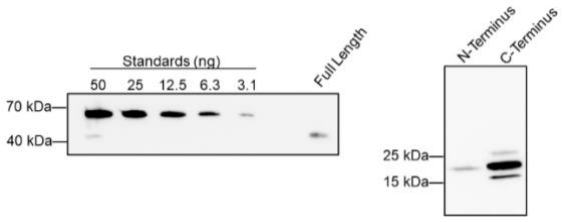

Figure S-1

Quantitative Western blots of supernatants from HEK293T cells expressing full-length, N-terminal, and C-terminal ERFE. All samples were analyzed alongside a range of amounts of FLAG-tagged standard (recombinant human His10-FLAG-BRD4, RnD Systems #SP-600). 4-20% reducing tris-glycine PAGE. Probed with anti-FLAG HRP. The apparent size of His10-FLAG-BRD4 on the gel is about 20% larger than ERFE, so an adjustment constant of 0.81 was applied to the ERFE variants in calculating their concentrations.

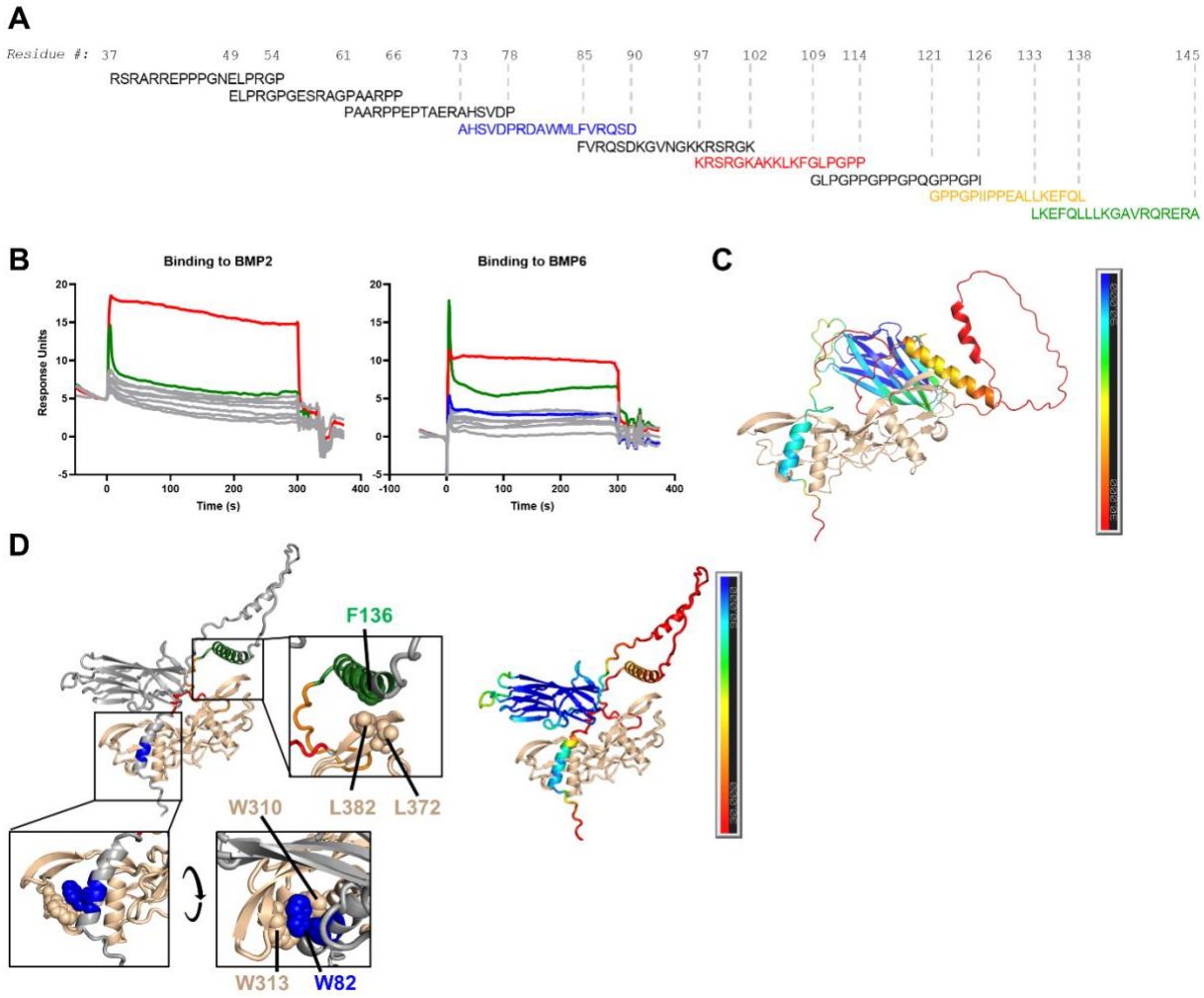

Figure S-2

(A) Diagram of overlapping synthetic 18-mer peptides used to scan the ERFE N-terminus for BMP-binding interactions. Color coding corresponds to the structural segments outlined in Figure 2B. (B) Surface plasmon resonance sensorgrams of 18-mer peptides binding to BMP2 and BMP6. (C) AlphaFold2 model of ERFE bound to a BMP2/6 heterodimer colored by confidence pLDDT (blue = high confidence). (D) AlphaFold2 model of ERFE bound to a BMP2 homodimer colored by structural segment (left) and confidence (right).

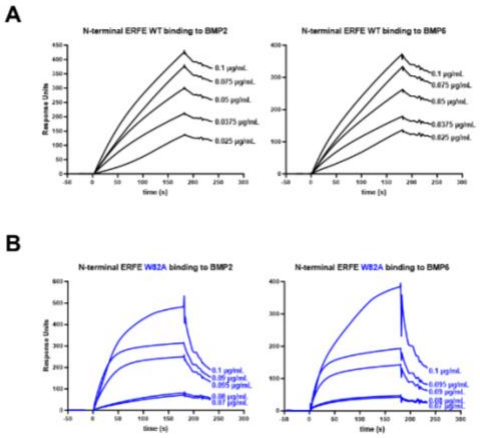

Figure S-3

Surface plasmon resonance sensorgrams of N-terminal ERFE (A) WT and (B) W82A binding to BMP2 and BMP6.

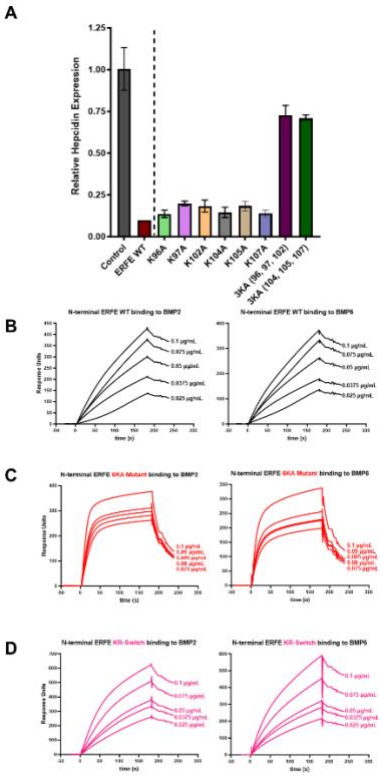

Figure S-4

(A) Expression of hepcidin mRNA in Hep3B cells treated with high concentrations of each indicated ERFE variant (10^{-8} M). The qPCR generated data are normalized to untreated controls. N = 2 biological replicates. Surface plasmon resonance sensorgrams of N-terminal ERFE (B) WT, (C) 6KA Mutant, and (D) KR-Switch binding to immobilized BMP2 and BMP6.

Figure S-5

WT, ΔCationic, 6KA Mutant, and KR-Switch ERFE fractions were bound to a heparin sulfate column and eluted with increasing concentrations of NaCl. Western blots of eluted fractions are shown. ERFE was detected using anti-FLAG HRP antibody.

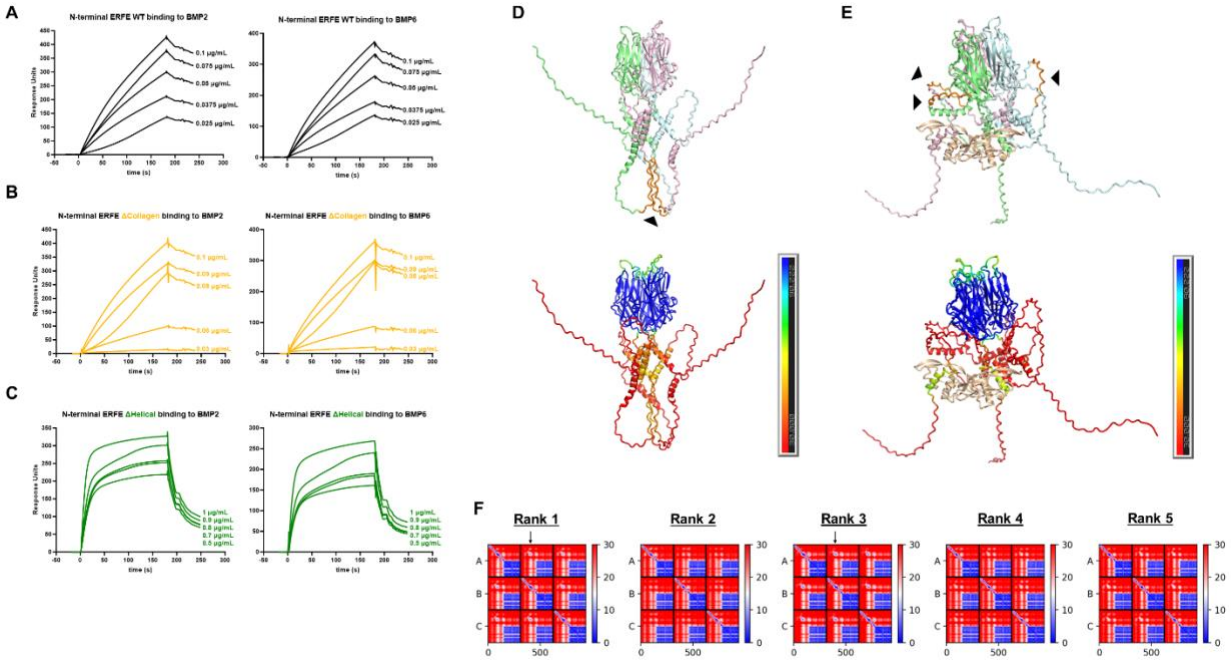

Figure S-6

Surface plasmon resonance sensorgrams of N-terminal ERFE (A) WT, (B) ΔCollagen, and (C) ΔHelical binding to immobilized BMP2 and BMP6. (D) AlphaFold2 rank 1 model of ERFE homotrimer colored by chain (top). Collagen Segments are shown in orange and indicated by the black arrowhead. The same model colored by confidence (bottom). (E) AlphaFold2 model of ERFE homotrimer bound to a BMP2/6 heterodimer colored by chain (top) and confidence (bottom). Arrows and orange color indicate Collagen Segments. (F) Predicted alignment error plots of ERFE homotrimer models (blue = small predicted error of alignment). The formation of a collagen triple helix was predicted strongly in model ranks 1 and 3 as indicated with arrows.

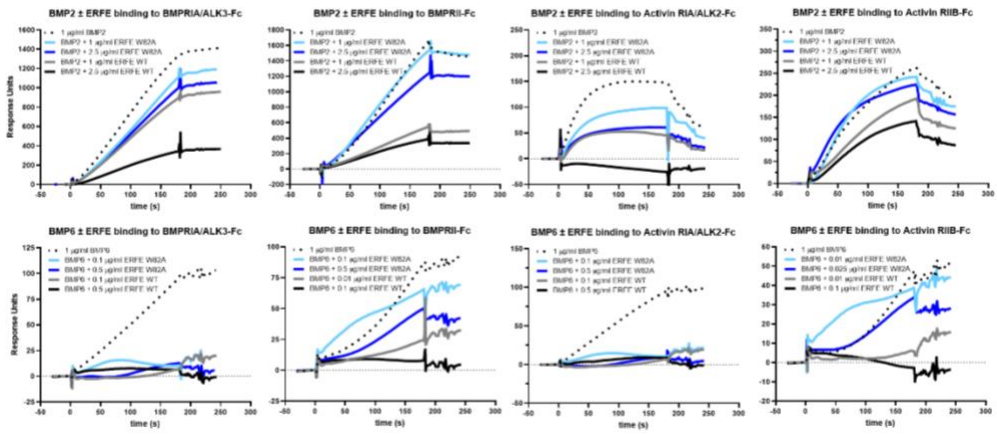

Figure S-7

Surface plasmon resonance sensorgrams of competition between ERFE and BMP receptors for binding to BMPs. Extracellular portions of different BMP receptor were immobilized and BMP2 (top) or BMP6 (bottom) flowed over alone or mixed with WT or W82A ERFE.

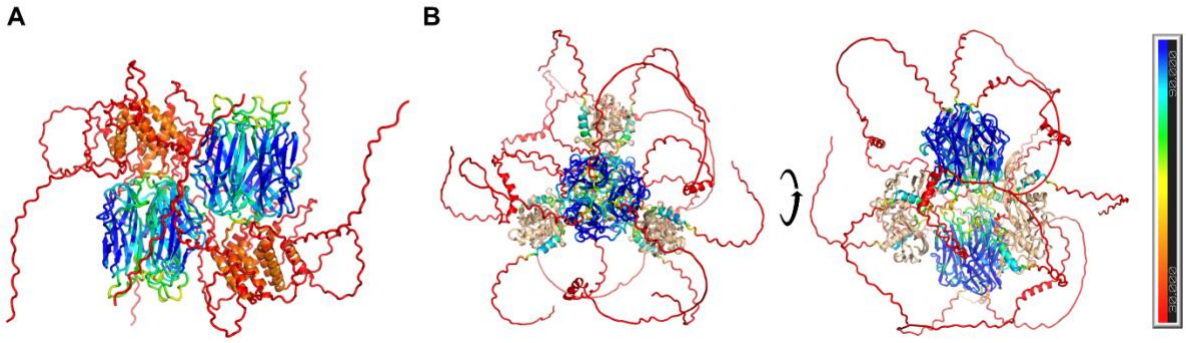

Figure S-8

(A) AlphaFold2 docking of hexameric human ERFE colored by confidence (blue = high confidence). (B) AlphaFold2 docking of hexameric human ERFE bound to three BMP2/6 dimers colored by confidence. BMP2/6 are shown in beige.

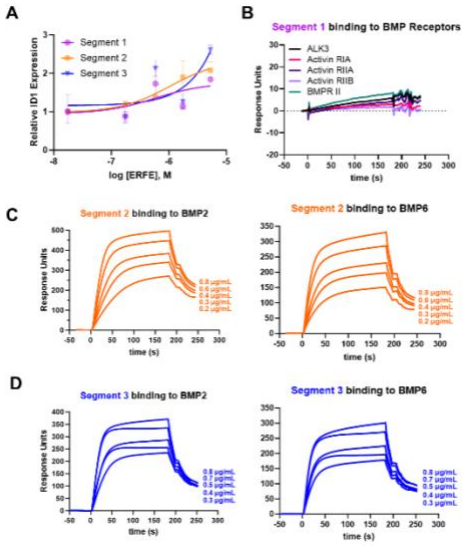

Figure S-9

(A) Expression of ID1 mRNA in Hep3B cells treated with indicated concentrations of N-terminal ERFE segments. qPCR data are normalized to untreated controls. N = 3 biological replicates. (B) Surface plasmon resonance sensorgram of N-terminal ERFE Segment 1 binding to BMP receptors. (C) SPR sensorgrams of N-terminal ERFE Segment 2 binding to BMP2 (left) and BMP6 (right). (D) SPR sensorgrams of N-terminal ERFE Segment 3 binding to BMP2 (left) and BMP6 (right).

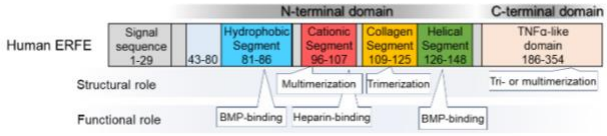

Figure S-10

Diagram of experimentally-determined roles of ERFE domains and features.

References

1. Nemeth, E. Hepcidin Regulates Cellular Iron Efflux by Binding to Ferroportin and Inducing Its Internalization. *Science* **306**, 2090–2093 (2004).

2. Wang, C.-Y. *et al.* Smad1/5 is required for erythropoietin-mediated suppression of hepcidin in mice. *Blood* **130**, 73–83 (2017).

3. Nemeth, E. *et al.* Hepcidin, a putative mediator of anemia of inflammation, is a type II acute-phase protein. *Blood* **101**, 2461–2463 (2003).

4. Wrighting, D. M. & Andrews, N. C. Interleukin-6 induces hepcidin expression through STAT3. *Blood* **108**, 3204–3209 (2006).

5. Haase, V. H. Regulation of erythropoiesis by hypoxia-inducible factors. *Blood Rev.* **27**, 41–53 (2013).

6. Hodges, V. M., Rainey, S., Lappin, T. R. & Maxwell, A. P. Pathophysiology of anemia and erythrocytosis. *Crit. Rev. Oncol. Hematol.* **64**, 139–158 (2007).

7. Kautz, L. *et al.* Erythroferrone contributes to hepcidin suppression and iron overload in a mouse model of β-thalassemia. *Blood* **126**, 2031–2037 (2015).

8. Olivera, J. D., Zhang, V., Nemeth, E. & Ganz, T. Erythroferrone exacerbates iron overload and ineffective extramedullary erythropoiesis in a mouse model of β-thalassemia. *Blood Adv.* bloodadvances.2022009307 (2023) doi:10.1182/bloodadvances.2022009307.

9. Arezes, J. *et al.* Antibodies against the erythroferrone N-terminal domain prevent hepcidin suppression and ameliorate murine thalassemia. *Blood* **135**, 547–557 (2020).

10. Stewart, A. N., Little, H. C., Clark, D. J., Zhang, H. & Wong, G. W. Protein Modifications Critical for Myonectin/Erythroferrone Secretion and Oligomer Assembly. *Biochemistry* **59**, 2684–2697 (2020).

11. Arezes, J. *et al.* Erythroferrone inhibits the induction of hepcidin by BMP6. *Blood* **132**, 1473–1477 (2018).

12. Wang, C.-Y. *et al.* Erythroferrone lowers hepcidin by sequestering BMP2/6 heterodimer from binding to the BMP type I receptor ALK3. *Blood* **135**, 453–456 (2020).

13. Fisher, A. L. & Babitt, J. L. Coordination of iron homeostasis by bone morphogenetic proteins: Current understanding and unanswered questions. *Dev. Dyn.* **251**, 26–46 (2022).

14. Bjelkmar, P., Larsson, P., Cuendet, M. A., Hess, B. & Lindahl, E. Implementation of the CHARMM Force Field in GROMACS: Analysis of Protein Stability Effects from Correction Maps, Virtual Interaction Sites, and Water Models. *J. Chem. Theory Comput.* **6**, 459–466 (2010).

15. Foley, E. M. & Esko, J. D. Hepatic Heparan Sulfate Proteoglycans and Endocytic Clearance of Triglyceride-Rich Lipoproteins. in *Progress in Molecular Biology and Translational Science* vol. 93 213–233 (Elsevier, 2010).

16. Asperti, M., Denardo, A., Gryzik, M., Arosio, P. & Poli, M. The role of heparin, heparanase and heparan sulfates in hepcidin regulation. in *Vitamins and Hormones* vol. 110 157–188 (Elsevier, 2019).

17. Poli, M. *et al.* Hepatic heparan sulfate is a master regulator of hepcidin expression and iron homeostasis in human hepatocytes and mice. *J. Biol. Chem.* **294**, 13292–13303 (2019).

18. Capila, I. & Linhardt, R. J. Heparin-Protein Interactions. *Angew. Chem. Int. Ed.* **41**, 390–412 (2002).

19. Wong, G. W., Wang, J., Hug, C., Tsao, T.-S. & Lodish, H. F. A family of Acrp30/adiponectin structural and functional paralogs. *Proc. Natl. Acad. Sci.* **101**, 10302–10307 (2004).

20. Wong, G. W. *et al.* Molecular, biochemical and functional characterizations of C1q/TNF family members: adipose-tissue-selective expression patterns, regulation by PPAR-γ agonist, cysteine-mediated oligomerizations, combinatorial associations and metabolic functions. *Biochem. J.* **416**, 161–177 (2008).

21. Brodsky, B. & Persikov, A. V. Molecular Structure of the Collagen Triple Helix. in *Advances in Protein Chemistry* vol. 70 301–339 (Elsevier, 2005).

22. Kotzsch, A. *et al.* Structure Analysis of Bone Morphogenetic Protein-2 Type I Receptor Complexes Reveals a Mechanism of Receptor Inactivation in Juvenile Polyposis Syndrome. *J. Biol. Chem.* **283**, 5876–5887 (2008).

23. Greenwald, J. *et al.* The BMP7/ActRII Extracellular Domain Complex Provides New Insights into the Cooperative Nature of Receptor Assembly. *Mol. Cell* **11**, 605–617 (2003).

24. Pajvani, U. B. *et al.* Structure-Function Studies of the Adipocyte-secreted Hormone Acrp30/Adiponectin: IMPLICATIONS FOR METABOLIC REGULATION AND BIOACTIVITY. *J. Biol. Chem.* **278**, 9073–9085 (2003).

25. Tsao, T.-S. *et al.* Role of Disulfide Bonds in Acrp30/Adiponectin Structure and Signaling Specificity: DIFFERENT OLIGOMERS ACTIVATE DIFFERENT SIGNAL TRANSDUCTION PATHWAYS. *J. Biol. Chem.* **278**, 50810–50817 (2003).

26. Wang, Y., Lam, K. S. L., Yau, M. & Xu, A. Post-translational modifications of adiponectin: mechanisms and functional implications. *Biochem. J.* **409**, 623–633 (2008).

27. Srole, D. N. & Ganz, T. Erythroferrone structure, function, and physiology: Iron homeostasis and beyond. *J. Cell. Physiol.* **236**, 4888–4901 (2021).

28. Yadin, D., Knaus, P. & Mueller, T. D. Structural insights into BMP receptors: Specificity, activation and inhibition. *Cytokine Growth Factor Rev.* **27**, 13–34 (2016).

29. Groppe, J. *et al.* Structural basis of BMP signalling inhibition by the cystine knot protein Noggin. *Nature* **420**, 636–642 (2002).

30. Paine-Saunders, S., Viviano, B. L., Economides, A. N. & Saunders, S. Heparan Sulfate Proteoglycans Retain Noggin at the Cell Surface. *J. Biol. Chem.* **277**, 2089–2096 (2002).

31. Allendorph, G. P., Isaacs, M. J., Kawakami, Y., Izpisua Belmonte, J. C. & Choe, S. BMP-3 and BMP-6 Structures Illuminate the Nature of Binding Specificity with Receptors † , ‡. *Biochemistry* **46**, 12238–12247 (2007).

32. Ganz, T. *et al.* Immunoassay for human serum erythroferrone. *Blood* **130**, 1243–1246 (2017).

33. Mirdita, M. *et al.* ColabFold: making protein folding accessible to all. *Nat. Methods* **19**, 679–682 (2022).

34. Jumper, J. *et al.* Highly accurate protein structure prediction with AlphaFold. *Nature* **596**, 583–589 (2021).

35. Bryant, P. *et al.* Predicting the structure of large protein complexes using AlphaFold and Monte Carlo tree search. *Nat. Commun.* **13**, 6028 (2022).

36. Pettersen, E. F. *et al.* UCSF Chimera?A visualization system for exploratory research and analysis. *J. Comput. Chem.* **25**, 1605–1612 (2004).

37. Jo, S., Kim, T., Iyer, V. G. & Im, W. CHARMM-GUI: A web-based graphical user interface for CHARMM. *J. Comput. Chem.* **29**, 1859–1865 (2008).

38. Lee, J. *et al.* CHARMM-GUI Input Generator for NAMD, GROMACS, AMBER, OpenMM, and CHARMM/OpenMM Simulations Using the CHARMM36 Additive Force Field. *J. Chem. Theory Comput.* **12**, 405–413 (2016).

39. Lee, J. *et al.* CHARMM-GUI supports the Amber force fields. *J. Chem. Phys.* **153**, 035103 (2020).

40. MacKerell, A. D. *et al.* All-Atom Empirical Potential for Molecular Modeling and Dynamics Studies of Proteins. *J. Phys. Chem. B* **102**, 3586–3616 (1998).

Chapter 3

Iron loading induces cholesterol synthesis and sensitizes endothelial cells to TNFα-mediated apoptosis

The contents of this chapter were originally published in the Journal of Biological Chemistry on September 2, 2021.

Fisher AL, **Srole DN**, Palaskas NJ, Meriwether D, Reddy ST, Ganz T, *et al.* Iron loading induces cholesterol synthesis and sensitizes endothelial cells to TNFα-mediated apoptosis. *Journal of Biological Chemistry* 2021:101156. https://doi.org/10.1016/j.jbc.2021.101156.

Abstract

In plasma, iron is normally bound to transferrin, the principal protein in blood responsible for binding and transporting iron throughout the body. However, in conditions of iron overload when the iron-binding capacity of transferrin is exceeded, non–transferrin-bound iron (NTBI) appears in plasma. NTBI is taken up by hepatocytes and other parenchymal cells *via* NTBI transporters and can cause cellular damage by promoting the generation of reactive oxygen species. However, how NTBI affects endothelial cells, the most proximal cell type exposed to circulating NTBI, has not been explored. We modeled *in vitro* the effects of systemic iron overload on endothelial cells by treating primary human umbilical vein endothelial cells (HUVECs) with NTBI (ferric

ammonium citrate [FAC]). We showed by RNA-Seq that iron loading alters lipid homeostasis in HUVECs by inducing sterol regulatory element-binding protein 2–mediated cholesterol biosynthesis. We also determined that FAC increased the susceptibility of HUVECs to apoptosis induced by tumor necrosis factor-α (TNFα). Moreover, we showed that cholesterol biosynthesis contributes to iron-potentiated apoptosis. Treating HUVECs with a cholesterol chelator hydroxypropyl-β-cyclodextrin demonstrated that depletion of cholesterol was sufficient to rescue HUVECs from TNFα-induced apoptosis, even in the presence of FAC. Finally, we showed that FAC or cholesterol treatment modulated the TNFα pathway by inducing novel proteolytic processing of TNFR1 to a short isoform that localizes to lipid rafts. Our study raises the possibility that iron-mediated toxicity in human iron overload disorders is at least in part dependent on alterations in cholesterol metabolism in endothelial cells, increasing their susceptibility to apoptosis.

Introduction

Iron is an essential micronutrient but can cause tissue damage when in excess. In healthy humans and animals, iron in plasma is bound to the protein transferrin. When the iron-carrying capacity of transferrin is exceeded, such as in iron overload conditions, iron appears in plasma complexed with low molecular weight molecules, collectively referred to as non-transferrin bound iron (NTBI) (1). The exact chemical composition of NTBI in the blood plasma is unknown but ferric citrate is thought to be the predominant NTBI species (2,3). NTBI is thought to contribute to organ dysfunction in iron overload conditions through the generation of reactive oxygen species that damage cellular lipids, proteins, and DNA (4), and can also promote susceptibility to certain infections (5). Since humans lack compensatory mechanisms to excrete excess iron, iron absorption is tightly regulated by the hormone hepcidin, which is produced in the liver. Hepcidin acts by binding to its receptor and only known iron exporter, ferroportin, blocking iron transport into plasma, and lowering plasma iron levels (6). Hepcidin deficiency results in iron overload in subjects with hereditary iron disorders and ineffective erythropoiesis. Iron overload can also occur in people with repeated blood transfusions, or excessive iron supplementation. Milder iron excess has been linked to metabolic disorders including diabetes (7-10) and nonalcoholic fatty liver disease (11-13).

NTBI accumulation in cells leads to their dysfunction, with specific tissue toxicities dependent on both the rate and extent of NTBI accumulation. The liver is the main storage organ for iron, but also the organ most commonly affected by chronic iron overload. Iron uptake pathways in hepatocytes include the classical transferrin-

transferrin receptor mediated uptake, as well as uptake of NTBI through specific transporters. Compared to transferrin-bound iron, hepatocytes take up NTBI at a rapid rate that exceeds their capacity for iron export, resulting in the net accumulation of excess iron when NTBI is chronically elevated (14). Iron accumulation in the liver in iron overload diseases increases the risk of hepatic fibrosis, cirrhosis, and hepatocellular carcinoma (15). Although most NTBI in plasma is cleared by the liver, NTBI can also be taken up by the pancreas, kidney, and heart (16). Thus, apart from the liver damage, severe iron overload is also known to cause cardiomyopathy, diabetes and other endocrinopathies (17,18). How different cell types take up NTBI is an area of active investigation (19), but ZIP14 was shown to be the NTBI transporter in hepatocytes and pancreatic acinar cells (20,21).

In patients with iron overload, circulating NTBI would contact endothelial cells first, yet the effect of NTBI on endothelial cell function has not been explored. In the liver, endothelial cells have emerged as a cell type with essential roles in iron homeostasis (22,23). In response to liver iron loading, hepatic sinusoidal endothelial cells produce bone morphogenetic proteins, which exert paracrine effects on hepatocytes to induce hepcidin production and thereby modulate systemic iron homeostasis (23). However, how endothelial cells take up and sense iron remains poorly understood.

In this study, we explored how NTBI accumulation affects cultured endothelial cells. Using unbiased RNA-Seq, we determined that iron loading of human umbilical vein endothelial cells (HUVECs) by ferric ammonium citrate (FAC) potently induced lipid biosynthesis through the sterol regulatory element-binding protein (SREBP) pathways, predominantly affecting SREBP2-mediated cholesterol metabolism. We further found

that cellular iron loading sensitized HUVECs to apoptotic cell death induced by TNFα and that iron loading augmented the TNFα pathway by generating a short isoform of TNFR1 through novel proteolytic cleavage. Evaluating the contribution of cholesterol biosynthesis and TNFR1 cleavage to iron-potentiated apoptosis, pharmacological depletion of cholesterol was sufficient to rescue the apoptotic phenotype even in the presence of excess iron and the presence of the short TNFR1 isoform. Thus, we provide specific evidence that iron loading alters endothelial cell cholesterol homeostasis and propose that the TNFR1 isoform acts as a biomarker for susceptibility to this new form of iron-dependent cell death.

Results

Iron induces cholesterol biosynthesis

We used a cell culture system to model the effects of systemic iron overload on endothelial cells by treating primary human umbilical vein endothelial cells (HUVECs) with non-transferrin-bound iron (NTBI) in the form of ferric ammonium citrate (FAC). We chose prolonged exposures (30-40 h of NTBI) based on preliminary experiments assessing HUVECs rate of iron loading and evidence of cellular damage. To identify global transcriptome changes in endothelial cells in response to NTBI, we performed RNA-Seq analysis of HUVECs treated with FAC for 30 h. Principal component analysis of RNA-Seq data showed that solvent- and FAC-treated groups were in distinct clusters, and indicated that the first principal component explains almost 40% of the variability among samples **(Figure 1A)**. Volcano plot analysis showed 816 differentially expressed genes, including both downregulated and upregulated genes, between solvent and FAC-treated HUVECs **(Figure 1B)**. Gene for transferrin receptor 1 (*TFRC*) was among

those with highly significant suppression **(Figure 1B)**, confirming that cells were effectively iron loaded. In the enriched gene set, ingenuity pathway analysis of FAC- and solvent-treated cells revealed that FAC primarily stimulates cholesterol biosynthesis pathways **(Figure 1C)**. We validated the RNA-Seq findings by measuring mRNA expression of genes involved in cholesterol biosynthesis by qRT-PCR in a separate set of HUVECs, treated with 100 μM FAC for 40 h. The cells were effectively iron-loaded, as reflected by the decrease in *TFRC* mRNA expression (P<0.001, *t*-test, **Figure 1D**). We confirmed increased expression of sterol regulatory element-binding protein 2 (*SREBP2*), transcription factor that is a master regulator of cholesterol synthesis (P=0.008, Mann-Whitney *U*). Expression of SREBP2 target genes was likewise upregulated: mevalonate pyrophosphate decarboxylase (*MVD*) (P=0.008, Mann-Whitney *U*), low-density lipoprotein receptor *(LDLR*) (P=0.008, Mann-Whitney *U*), and 3-Hydroxy-3-Methylglutaryl-CoA Reductase (*HMGCR*) (P<0.001, *t*-test) **(Figure 1E-H)**. Furthermore, we measured *SREBP2* mRNA expression in HUVECs treated with different forms of iron, including NTBI (FAC, ferrous ammonium sulfate, ferric chloride), transferrin-bound iron, holo-ferritin, hemin, or with triammonium citrate as a control **(Supplemental Figure 1A)**. Most of the iron treatments induced *SREBP2* mRNA whereas triammonium citrate (lacking iron) did not. Expression of *SREBP2* correlated with the degree of cellular iron loading as measured by ferritin heavy chain immunoblotting (r=0.826, P=0.012, **Supplemental Figure 1B**). This result demonstrated that it is the cellular iron loading as opposed to the specific form of NTBI that induces cholesterol synthesis.

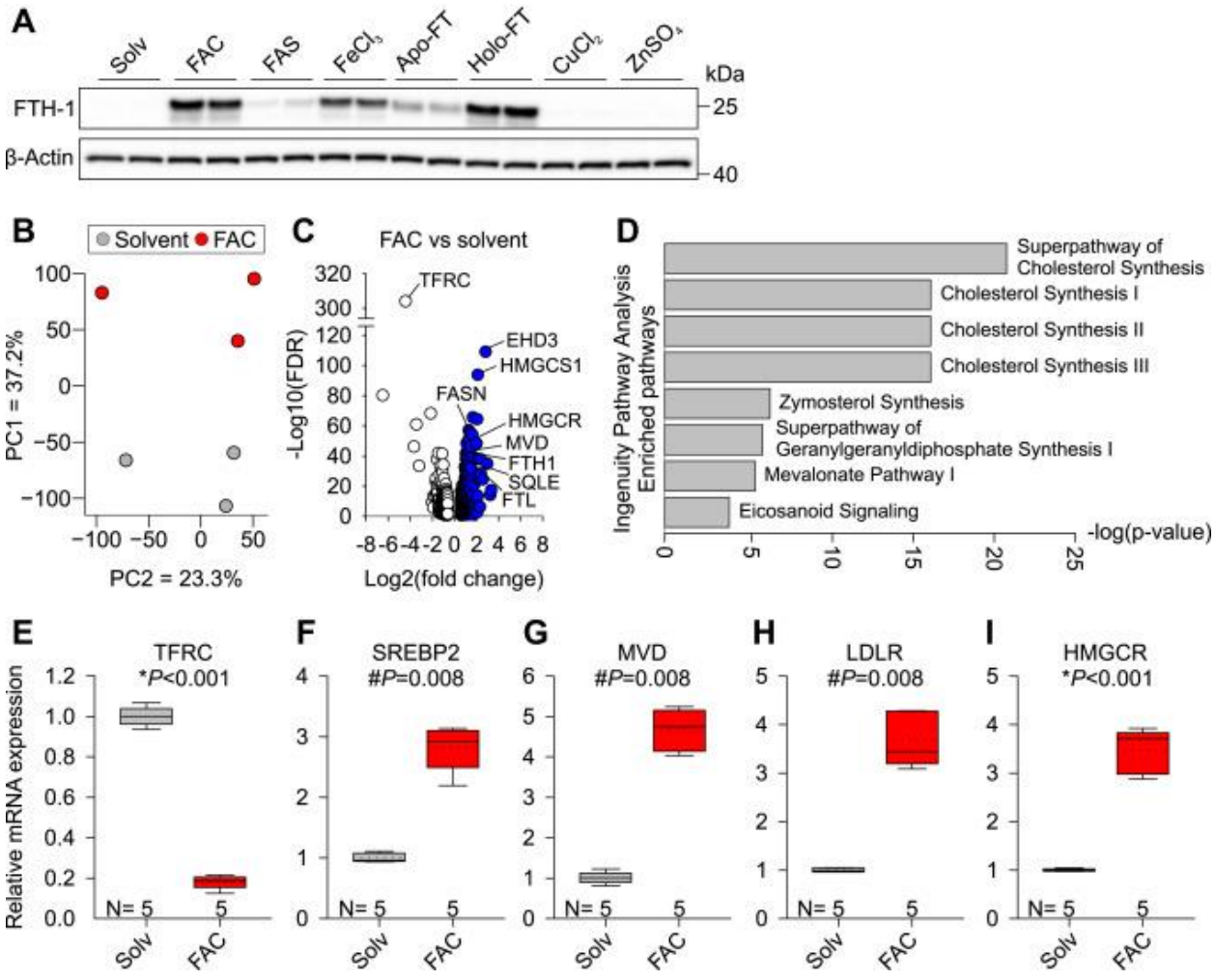

Figure 1. Iron induces cholesterol biosynthesis in primary HUVECs.

A, Western blot for iron storage protein FTH1 in HUVECs treated with solvent (water) or 100 μM FAC, ferric ammonium sulfate (FAS, 100 μM), ferric chloride ($FeCl_3$, 100 μM), apoferritin (FT, 2 mg/ml), holo-FT (2 mg/ml), copper chloride ($CuCl_2$, 100 μM), or zinc sulfate ($ZnSO_4$, 100 μM) for 24 h. β-Actin was used as a loading control. *B–D*, to induce cellular iron loading, primary HUVECs were treated with solvent (water) or 100 μM FAC for 30 h, and total RNA was collected for RNA-Seq. *B*, principal component scatter plot of gene expression in FAC-treated (*red circles*) *versus* solvent-treated (*gray circles*) HUVECs. The percentages of each axis represent the percentage of variation explained

by the principal components. *C*, volcano plot of 816 differentially expressed genes comparing FAC- *versus* solvent-treated HUVECs. Differentially expressed genes were identified by fold change of greater or less than ±1.5 and $p < 0.05$. *White circles* represent downregulated genes, and *blue circles* represent upregulated genes. *D*, ingenuity pathway analysis identifying significantly enriched categories between FAC- and solvent-treated HUVECs (top hits shown, based on $p < 0.001$ and *z*-score > 2). *E*–*I*, primary HUVECs were treated with solvent (water, *gray*) or 100 μM FAC (*red*) for 40 h. qPCR analysis of (*E*) iron importer *TFRC* and (*F*–*I*) cholesterol biosynthesis genes *SREBP2*, *MVD*, *LDLR*, and *HMGCR*. Data are shown as $2^{-\Delta\Delta Ct}$. The number of biological replicates is indicated above the *x*-axis. Statistical differences between groups were determined by Student's *t* test for normally distributed values (denoted by $*$) or Mann–Whitney *U* for non-normally distributed values (denoted by #). FAC, ferric ammonium citrate; HUVECs, human umbilical vein endothelial cells.

We further measured mRNA expression of SREBP transcription factors that control fatty acid biosynthetic pathways. FAC treatment of HUVECs increased expression of *SREBP1* isoforms a and c (both $P<0.001$, *t*-test) and their gene targets acetyl-CoA carboxylase (*ACCA*) ($P=0.002$, *t*-test), and fatty acid synthase (*FASN*) ($P<0.001$, *t*-test) **(Supplemental Figure 2A-E)**, suggesting that iron plays a broader role in lipid homeostasis. Taken together, these findings demonstrate that iron loading of endothelial cells induces expression of the SREBP pathway genes that control sterol and fatty acid synthesis.

To assess the effect on lipid synthesis, HUVECs were labeled with [U^{13}C]-D-glucose and treated with FAC for 30 and 40 h, the two time-points used for transcriptional analysis in Figure 1. Using isotopomer spectral analysis we did not detect any changes in the synthesis of saturated fatty acids myristic acid (14:0) or stearic acid (18:0) with FAC treatment **(Figure 2A and B)**. FAC treatment mildly increased synthesis of palmitic acid (16:0) ($P=0.030$, one-way ANOVA) and oleic acid (18:1) ($P=0.034$, one-way ANOVA) after 40h **(Figure 2C and D),** and strongly induced synthesis of unsaturated fatty acid palmitoleic acid (16:1) at both time points ($P=0.002$ at 30 h, and $P<0.001$ at 40 h, one-way ANOVA) **(Figure 2E)**. FAC had the strongest effect on cholesterol biosynthesis, with 4-fold induction achieved by 40 h (**Figure 2F**; $P=0.002$ at 30 h and $P<0.001$ at 40 h, one-way ANOVA). Increases in cellular cholesterol were also confirmed by staining of HUVECs with a fluorescent cholesterol probe filipin after FAC treatment **(Figure 2G),** which revealed cytoplasmic rather than cell surface distribution. Cholesterol-treated HUVECs were used as a control for filipin staining.

We considered whether cellular membrane damage mediates inductions in cholesterol biosynthesis and measured oxidized phospholipid composition in FAC-treated HUVECs. We did not detect any major iron-dependent changes in the cellular composition of 1-palmitoyl-2-(5-oxovaleroyl)-sn-glycero-3-phosphocholine (POVPC), 1-palmitoyl-2-glutaroyl-sn-glycero-3-phosphocholine (PGPC), 1-palmitoyl-2-arachidonoyl-sn-glycero-3-phosphocholine (PAPC), or 1-(palmitoyl)-2-(5-keto-6-octene-dioyl)phosphatidylcholine (KOdiA-PC) **(Figure 2H-K)**. Taken together, our data suggests that iron stimulates cholesterol biosynthesis independent of membrane damage.

To identify whether iron loading of other cell types alters their *SREBP2* mRNA, human cell lines Hep3B (hepatocellular carcinoma) and immortalized endothelial line teloHAEC were treated with 100 μM FAC for 40 h. FAC decreased *TFRC* expression in both Hep3B and teloHAEC, confirming that these cell lines efficiently load FAC **(Supplemental Figure 3A)**. Despite this, neither Hep3B nor teloHAEC induced *SREBP2* expression, and Hep3Bs even moderately reduced *SREBP2* expression **(Supplemental Figure 3B)**. This result suggests that although iron-dependent changes in cholesterol homeostasis occur in primary endothelial cells, such cellular response to iron loading is not universal.

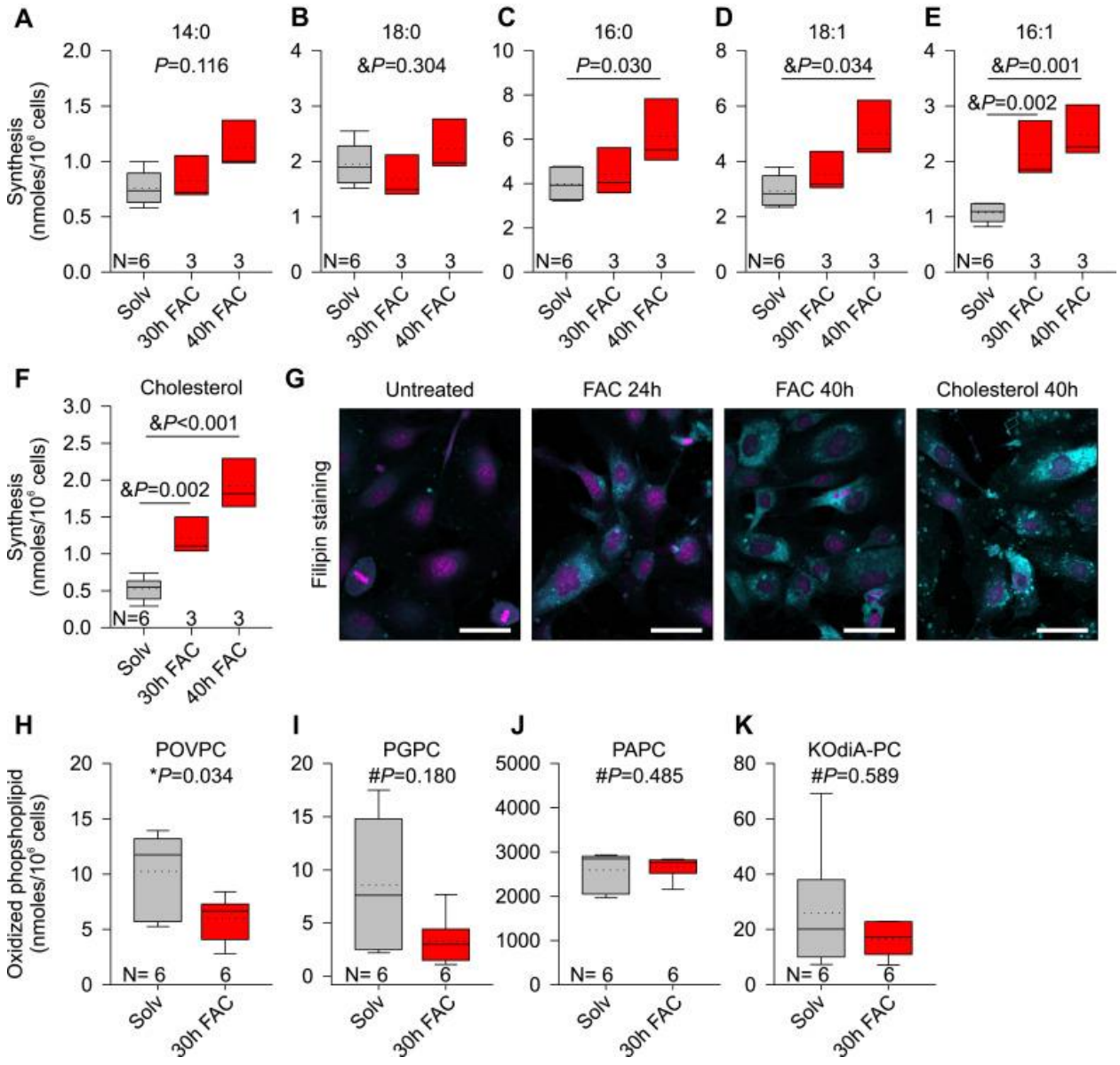

Figure 2. Lipid composition in control and iron-loaded HUVECs.

A–*F*, isotopic spectral analysis of HUVECs treated with solvent (water, *gray*) or 100 μM FAC (*red*) for 30 or 40 h in the presence of 5 mM [U^{13}C]-D-glucose. Lipid synthesis is expressed as nanomoles/million cells: cellular (*A*) myristic acid (14:0), (*B*) stearic acid (18:0), (*C*) palmitic acid (16:0), (*D*) oleic acid (18:1), (*E*) palmitoleic acid (16:1), and (*F*) cholesterol. *G*, confocal microscopy of filipin fluorescence staining of cholesterol (*turquoise* pseudo color) of HUVECs treated with 100 μM FAC for 24 or 40 h. HUVECs

treated with 50 μM cholesterol-methyl-β-cyclodextrin (MβCD) were used as a positive control. Nuclear stain (*violet* pseudo color) = SYTOX green. The scale bar represents 50 μm. *H–K*, LC-MS analysis of oxidized phospholipids in HUVECs treated with solvent (water) or 100 μM FAC for 30 h. *H*, 1-palmitoyl-2-(5-oxovaleroyl)-sn-glycero-3-phosphocholine (POVPC), (*I*) 1-palmitoyl-2-glutaroyl-sn-glycero-3-phosphocholine (PGPC), (*J*) 1-palmitoyl-2-arachidonoyl-sn-glycero-3-phosphocholine (PAPC), and (*K*) 1-(palmitoyl)-2-(5-keto-6-octene-dioyl)phosphatidylcholine (KOdiA-PC). The number of replicates is indicated above the *x*-axis. Statistical differences between groups were determined by one-way ANOVA on ranks with Dunn's method of multiple comparison for non-normally distributed values, one-way ANOVA followed by Holm–Sidak method of multiple comparisons for normally distributed values (denoted by &), Student's *t* test (denoted by ∗), or Mann–Whitney *U* for non-normally distributed values (denoted by #). FAC, ferric ammonium citrate; HUVECs, human umbilical vein endothelial cells.

Cellular iron loading potentiates apoptosis

In iron overload conditions, NTBI causes toxicity through promoting the formation of free radicals in tissues in which it accumulates. We next evaluated the sensitivity of endothelial cells to iron-mediated cytotoxicity. Caspase-3 is known to be a critical executioner of apoptosis, and its activation requires proteolytic processing of the proenzyme (24,25). We therefore determined the levels of cleaved caspase-3 as a marker of apoptosis in HUVECs treated with 100μM FAC for 30 h, but FAC treatment alone did not cause apoptosis (**Figure 3**). We then assessed the effect of iron loading on the apoptosis caused by TNFα, a stimulus known to potentiate apoptotic cell death. TNFα treatment (5 and 50 ng/ml for 6 h) by itself mildly increased cleaved caspase-3. However, we observed a strong interaction between iron and inflammation, where FAC treatment significantly potentiated cleaved caspase-3 induced by TNFα **(Figure 3).** The result indicates that iron loading increases the susceptibility of endothelial cells to inflammatory damage. We did not observe any FAC-dependent potentiation of cleaved caspase-3 by TNFα in immortalized Hep3B or teloHAEC **(Supplemental Figure 4**), suggesting that primary endothelial cells are most susceptible to iron-potentiated apoptosis.

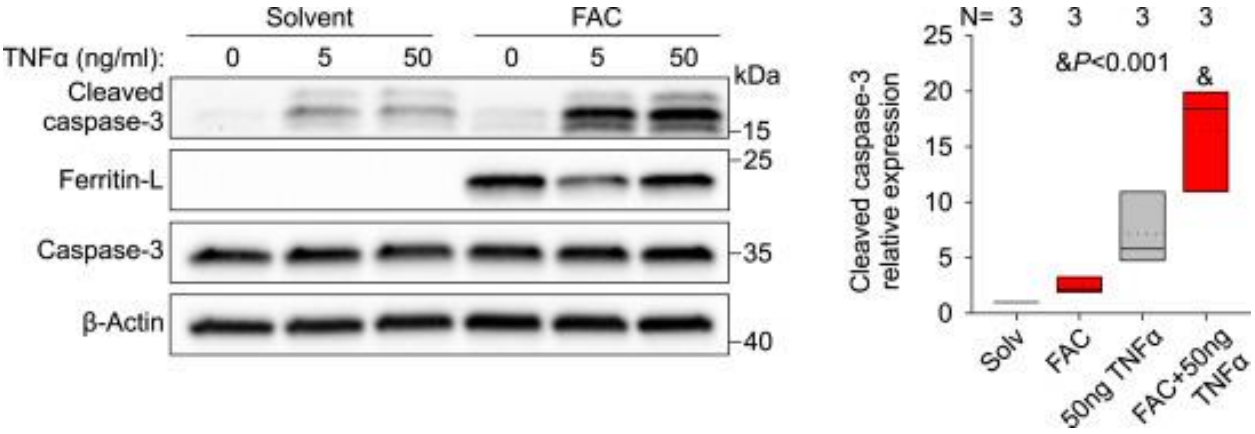

Figure 3. Iron loading of HUVECs sensitizes them to apoptosis.

Primary HUVECs were treated with solvent (water, *gray*) or 100 μM FAC (*red*) for 24 h before stimulation with 5 or 50 ng/ml TNFα in normal or FAC-supplemented media for 6 h. Western blot for cleaved caspase-3. Representative image of N = 3 independent experiments. Quantification of cleaved caspase-3 normalized to β-actin is shown for the 50 ng/ml dose. Statistical differences between groups were determined by one-way ANOVA for normally distributed values. HUVECs, human umbilical vein endothelial cells; TNFα, tumor necrosis factor-α.

Iron modulates TNFR1 proteolytic processing

We next evaluated whether iron alters signaling downstream of TNFα, which could increase susceptibility to cell death. TNFα has two main receptors, TNFR1 (or p55) and TNFR2 (or p75), which are expressed on many cell types but belong to different subgroups of the TNFR family. TNFR1 is a death receptor and harbors a death domain in its cytoplasmic portion, which links TNFR1 to apoptosis and necroptosis (26). In comparison, TNFR2 does not contain a death domain. TNFR1 is a 55-kDa transmembrane protein that is shed into circulation as 27- to 30-kDa soluble proteins after extracellular cleavage (27,28), and can inhibit TNFα by competing for TNFα binding. Thus, we evaluated the effect of iron excess on TNFR1 expression. HUVECs were treated with FAC over a time-course between 0-48 hours and we assessed TNFR1 mRNA and protein expression. FAC treatment did not significantly alter *TNFRSF1A* mRNA expression **(Figure 4A)**. However, FAC treatment strongly affected TNFR1 protein composition. Although the longest isoform (55-kDa) was relatively stable with FAC treatment, a novel shorter isoform (35-kDa) was induced 10-fold at 24 and 48 h (P<0.001, one-way ANOVA) **(Figure 4B)**. To ensure that the 35-kDa isoform is TNFR1 rather than a result of nonspecific antibody interaction with another protein, we validated the finding by depleting HUVECs of endogenous TNFR1 using control siRNA (siNC) or siRNA targeting TNFR1 (siTNFR1) for 48 h and treating the cells with FAC or solvent for 24 h. Treatment with siTNFR1 reduced the mRNA levels ~5-fold, and reduced protein expression of both the full length and shorter isoform of TNFR1 **(Supplemental Figure 5A-B)**, confirming the specificity of the antibody.

We next tested whether the induction of the smaller 35-kD isoform was specifically caused by cellular iron loading. We treated HUVECs with FAC, ferrous ammonium sulfate (FAS), ferric chloride ($FeCl_3$), apo-ferritin (apo-FT, ferritin lacking iron), holo-ferritin (holo-FT, ferritin containing iron), copper chloride ($CuCl_2$), or zinc sulfate ($ZnSO_4$) for 24 h. Induction of the short TNFR1 isoform was strongest with FAC treatment, occurred to a lesser extent with $FeCl_3$ and holo-FT, and was not induced by FAS, apo-FT, copper, or zinc **(Figure 4C)**. In agreement, the levels of the short TNFR1 isoform correlated with the degree of iron loading as measured by FTH1 expression, with an apparent threshold at FTH1/β-actin of about 30 **(Figure 4D)**, whereas the levels of the full-length isoform did not correlate with FTH1 expression **(Supplemental Figure 6)**.

To determine the cellular localization of the short TNFR1 isoform, we performed membrane enrichment assays. In view of the reported recruitment of TNFR1 to lipid rafts (29), we determined the localization of the short TNFR1 isoform in membrane fractions from HUVECs treated with solvent or FAC for 24 h. Using density-gradient centrifugation, we found that FAC treatment upregulates expression of the short form of TNFR1 in the lipid rafts fractions, as defined by the enrichment of flotillin-1 and ganglioside GM-1 **(Figure 4E)**.

We next examined whether iron induces proteolytic processing of TNFR1 to generate the shorter isoform. HUVECs were transduced with lentivirus expressing TNFR1 (pLX304-TNFR1) prior to FAC treatment. Since the lentivirus contains TNFR1 cDNA, any change in TNFR1 would be from post-translational modifications rather than generation of new mRNA isoforms. FAC treatment of HUVECs overexpressing TNFR1 resulted in a strong induction in the short but not full-length TNFR1 isoform **(Figure 5A)**,

confirming that TNFR1 regulation by iron is a result of proteolytic processing rather than generation of a new mRNA isoform. Considering this, we first evaluated the role of the canonical TNFR1 cleavage pathways in the induction of the short TNFR1 isoform. These pathways have been previously shown to generate a 27-30 kDa soluble fragment (30) and 26-30 kDa cell-associated fragment of TNFR1 (27,31). Treatment of FAC-loaded HUVECs with TAPI2, an ADAM17 (TNFα converting enzyme, TACE) and matrix metalloprotease inhibitor in combination with FAC did not change the amount of the lower TNFR1 isoform despite a reduction in soluble TNFR1 in supernatants **(Figure 5B)**. Furthermore, treatment of HUVECs with DAPT, a γ-secretase inhibitor, prior to iron loading did not alter expression of the short TNFR1 isoform **(Figure 5C)**, suggesting that generation of the 35-kDa isoform is independent of the canonical TNFR1 cleavage processes. Further evaluation of proteolytic processing using a panel of protease inhibitors in HUVECs showed that protease inhibitors antipain (serine inhibitor) and leupeptin (serine & thiol inhibitor) increased expression of the short TNFR1 isoform similarly as FAC treatment or treatment with a protease inhibitor cocktail (containing aprotinin, bestatin, E-64, leupeptin, and pepstatin A) **(Figure 5D)**, demonstrating that FAC treatment mimics the action of protease inhibitors and thereby suggesting that FAC may antagonize or inactivate one or more serine proteases.

In addition to the known *N*-linked glycosylation sites on TNFR1 (asparagine 54, 145, and 151), we considered whether the 35-kDa isoform may be a result of glycosylation of an even smaller fragment, by treating HUVECs with FAC for 30 h and evaluating *N*- and *O*-linked glycosylation. As expected, the full-length TNFR1 isoform was *N*-linked glycosylated, as treatment with PNGaseF resulted in a downward shift in the molecular

weight of full-length TNFR1 compared to untreated and *O*-glycosidase treated lysates **(Supplemental Figure 7)**. However, the molecular weight of the short TNFR1 isoform was similar between untreated, *N*- and *O*-deglycosylated lysates **(Supplemental Figure 7)**, indicating that the short isoform is not glycosylated. We similarly detected induction of the short TNFR1 isoform with FAC loading in Hep3B and teloHAEC **(Supplemental Figure 8)**, suggesting a more common role of iron in TNFR1 processing.

Our data show that iron alters lipid homeostasis and proteolytic processing of TNFR1 in endothelial cells. We next asked whether altered lipid homeostasis or TNFR1 expression contributes to iron-potentiation of apoptosis.

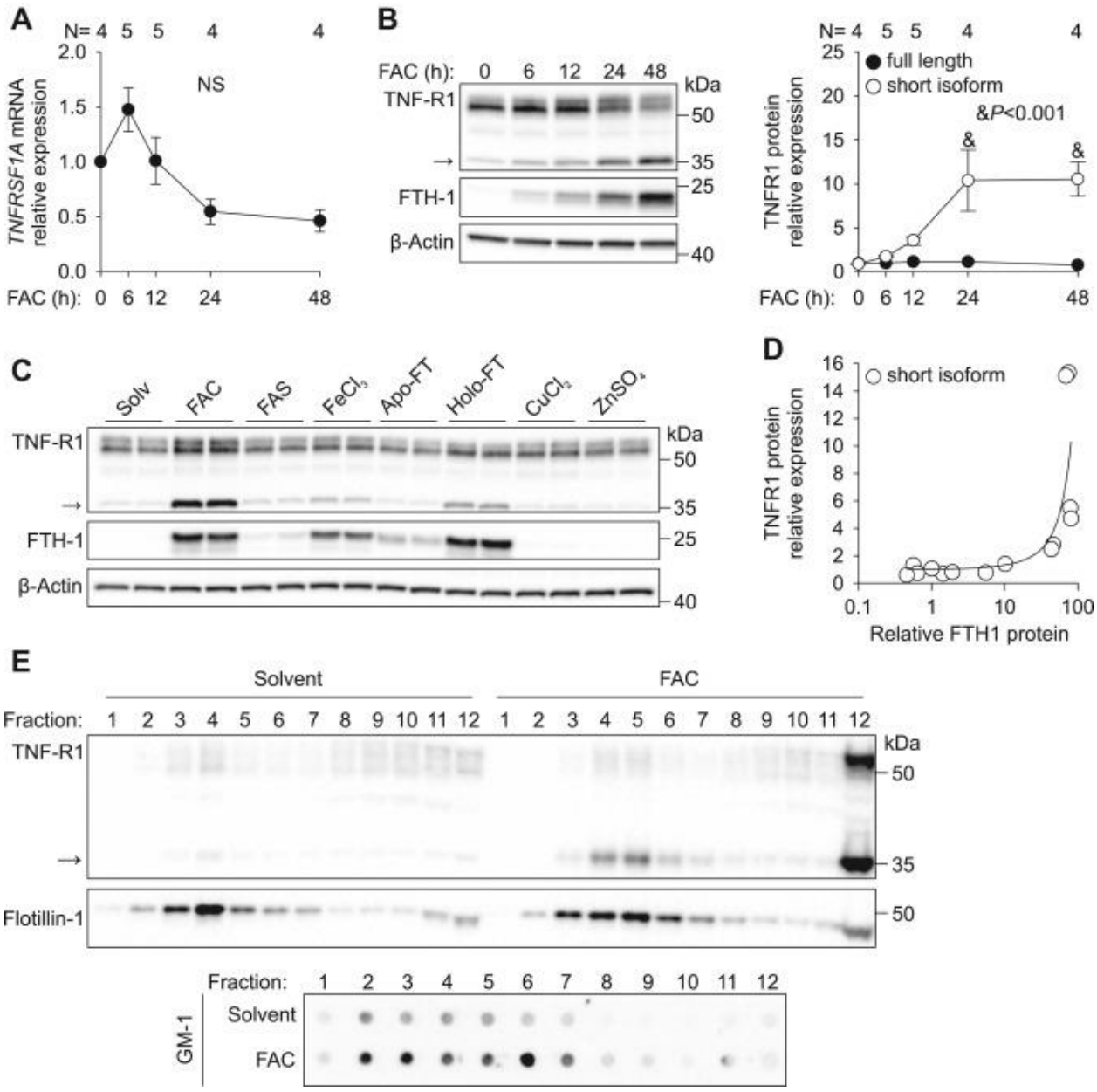

Figure 4. In HUVECs, iron loading induces expression of a short isoform of TNFR1 that localizes to lipid rafts.

A, primary HUVECs were treated with 100 μM FAC for 0 to 48 h. *TNFRSF1A* mRNA analysis by qRT-PCR normalized to *HPRT* and expressed as $2^{-\Delta\Delta Ct}$. *B*, Western blot and protein quantification of the full-length (55 kDa) and short TNFR1 isoform (35 kDa, indicated by an *arrow*) normalized to β-actin. *C*, Western blot for TNFR1 in HUVECs

treated with solvent (water) or 100 μM FAC, ferric ammonium sulfate (FAS, 100 μM), ferric chloride ($FeCl_3$, 100 μM), apoferritin (FT, 2 mg/ml), holo-FT (2 mg/ml), copper chloride ($CuCl_2$, 100 μM), or zinc sulfate ($ZnSO_4$, 100 μM) for 24 h. The FTH1 and β-actin blots are replicated from Figure 1*A* but are provided here for clarity. *D*, correlation between FTH1 and short TNFR1 isoform normalized to β-actin. *E*, HUVECs treated with solvent (water) or 100 μM FAC for 24 h were subjected to sucrose density gradient centrifugation to isolate lipid rafts. Proteins from equal volume of collected fractions were separated by SDS-PAGE and analyzed by Western blotting. To analyze the distribution of GM-1, each fraction was dot-blotted onto a nitrocellulose membrane and detected using CTx^{HRP}. Statistical differences were determined by one-way ANOVA with the Holm–Sidak method of multiple comparisons. FAC, ferric ammonium citrate; HUVECs, human umbilical vein endothelial cells; NS, not significant.

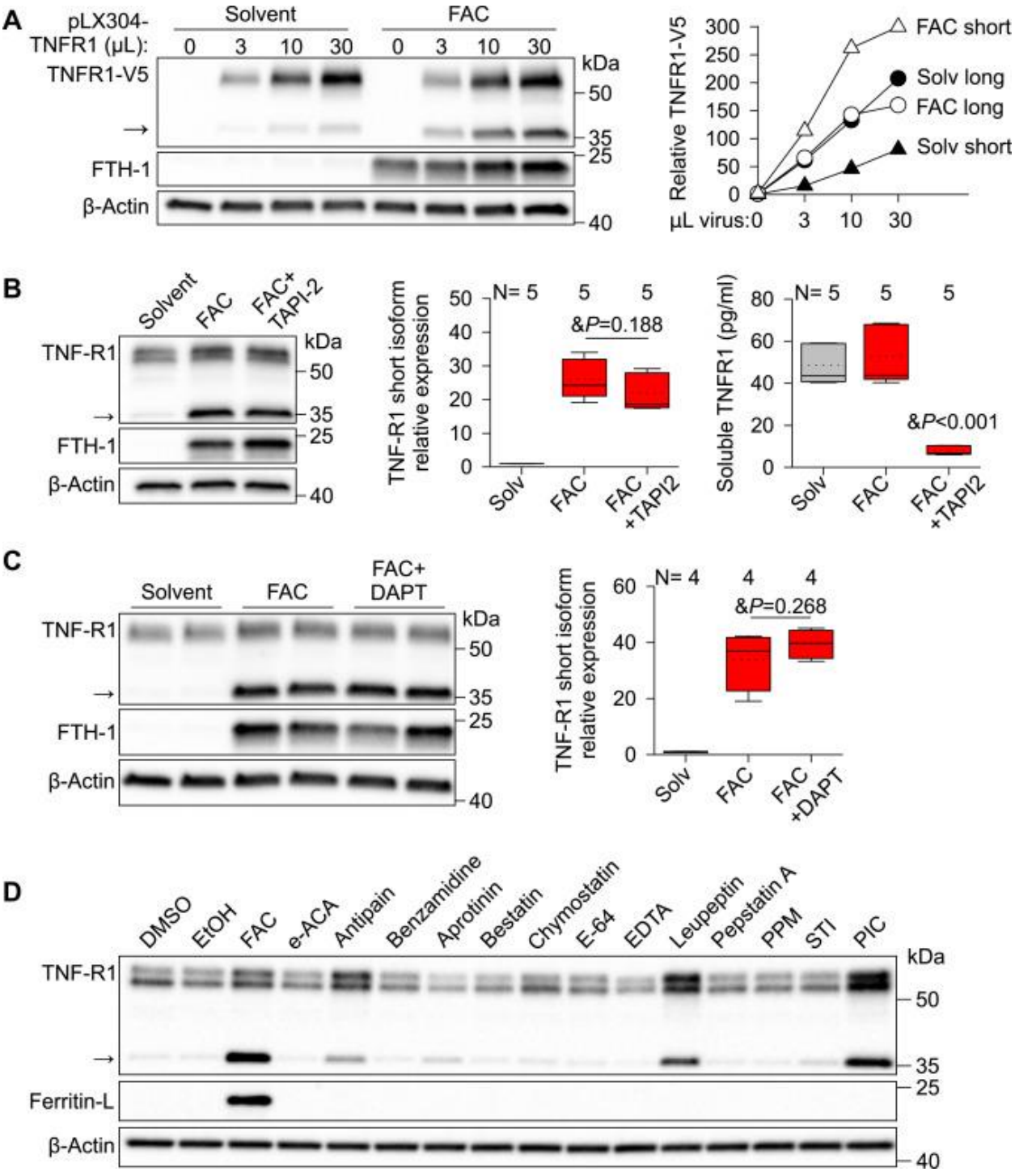

Figure 5. Iron induces post-translational modifications of TNFR1.

A, HUVECs were transduced with increasing volume of lentivirus expressing human TNFR1 with a C-terminal V5 tag for 10 h before incubation with solvent (water) or

100 μM ferric ammonium citrate (FAC) for 24 h. Western blot using anti-V5 antibody; the short isoform indicated by an *arrow*. *B*, HUVECs were treated with solvent (water, *gray*) or 100 μM FAC (*red*) with and without 25 μM TAPI-2 inhibitor for 24 h and Western blot performed for TNFR1. Representative image showing endogenous TNFR1 (*left*), quantification of the small TNFR1 isoform (*middle*), and quantification of soluble TNFR1 in HUVEC supernatants (*right*). *C*, Western blot and quantification of small TNFR1 isoform after HUVECs were treated with solvent (water) or 100 μM FAC with and without 1 μM DAPT inhibitor. *D*, Western blot for TNFR1 in HUVECs treated with solvents DMSO or ethanol, or a panel of protease inhibitors: 6-aminohexanoic acid (E-ACA, 40 mM), antipain (100 μM), benzamidine HCl (4 mM), aprotinin (1 μM), bestatin (40 μM), chymostatin (100 μM), E-64 (10 μM), EDTA (1 mM), leupeptin (100 μM), pepstatin A (1 μM), phosphoramidon (PPM, 10 μM), soybean trypsin inhibitor (STI, 5 μM), or protease inhibitor cocktail (PIC, 1:200) for 24 h. FAC was used as a positive control. β-Actin was used as a loading control. The number of replicates is indicated above the *x*-axis. Statistical differences between groups were determined by one-way ANOVA with the Holm–Sidak method for multiple comparisons for normally distributed values. FAC, ferric ammonium citrate; HUVECs, human umbilical vein endothelial cells.

Cellular cholesterol loading potentiates apoptosis and promotes TNFR1 processing

We tested the contribution of high cellular cholesterol on apoptosis by treating HUVECs with 50 μM cholesterol-methyl-β-cyclodextrin (MβCD) for 24 h prior to stimulation with 50 ng/ml TNFα for 16 h, and compared the apoptotic response seen with the combination of FAC and TNFα. Cholesterol-MβCD by itself had no effect on cleaved caspase-3, but co-treatment with TNFα did potentiate cleaved caspase-3 (P=0.008, one-way ANOVA), to a similar level as FAC **(Figure 6A)**. Interestingly, cholesterol-MβCD also induced expression of the shorter TNFR1 isoform (P=0.002, one-way ANOVA) **(Figure 6B)**.

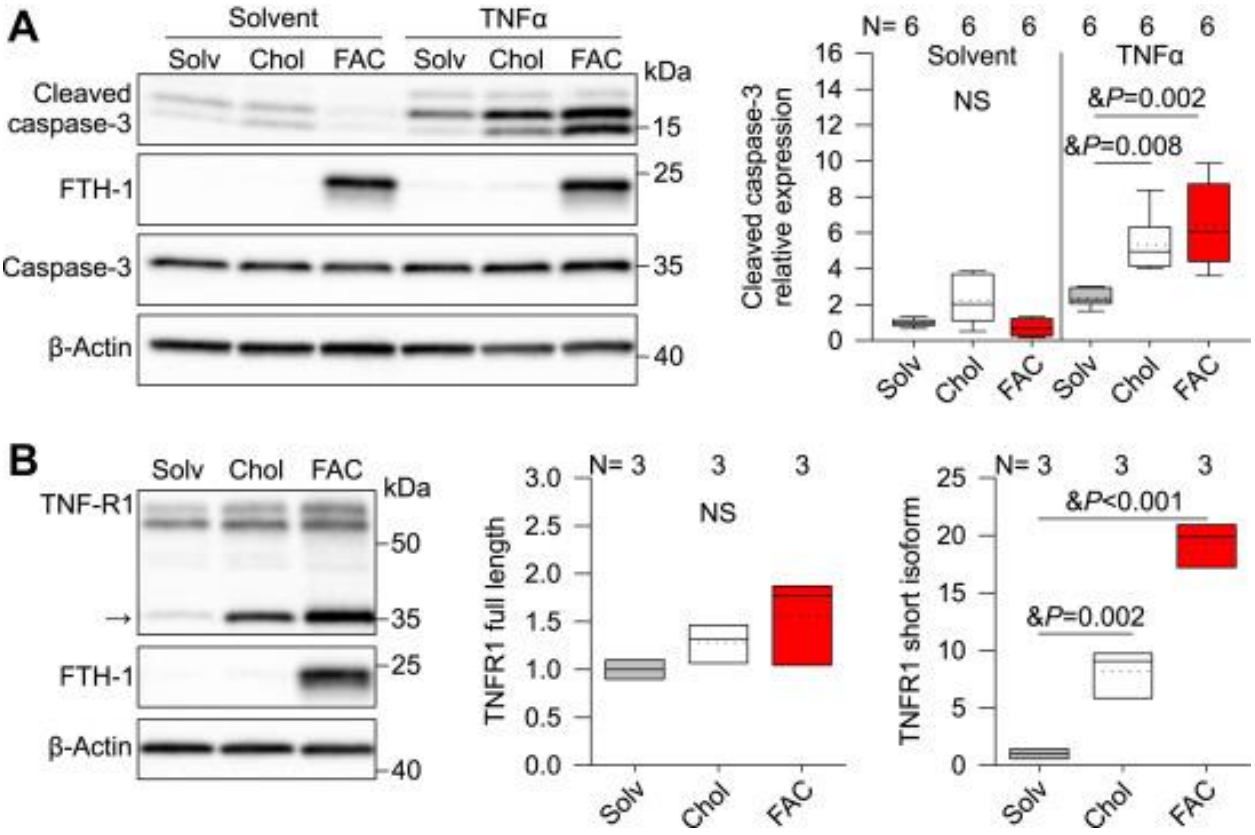

Figure 6. Cholesterol treatment potentiates apoptosis and increases TNFR1 short isoform in HUVECs.

A, cleaved caspase-3 Western blot of HUVECs treated with solvent (water, *gray*), 50 µM cholesterol-MβCD (*white*), or 100 µM FAC (*red*) followed by stimulation with 50 ng/ml TNFα for 16 h. *B*, Western blot and protein quantification of full-length and TNFR1 short isoform (indicated by an *arrow*) in HUVECs treated with solvent (water, *gray*), 50 µM cholesterol-MβCD (*white*), or 100 µM FAC (*red*) for 40 h. Representative images of N = 3 independent experiments. β-Actin was used as a loading control. Statistical differences between groups were determined by one-way ANOVA with the Holm–Sidak method for multiple comparisons for normally distributed values. FAC, ferric ammonium citrate; HUVECs, human umbilical vein endothelial cells; MβCD, cholesterol-methyl-β-cyclodextrin.

Modulation of cholesterol metabolism rescues iron-dependent apoptosis

To evaluate the role of lipid metabolism in FAC-potentiated apoptosis, HUVECs were treated with different drugs that alter cellular cholesterol content, then treated with 100 μM FAC and 50 ng/ml TNFα. U18666A (1 μM) was used to inhibit cholesterol movement out of lysosomes, whereas (2-hydroxypropyl)-β-cyclodextrin (HPCD, 0.3%) and methyl-β-cyclodextrin (MCD, 50 μM) were used to deplete cholesterol. As expected, FAC strongly potentiated cleaved caspase-3 expression induced by TNFα **(Figure 7A)**. Neither treatment of FAC-loaded cells with U18666A nor MCD was sufficient to rescue apoptosis **(Figure 7A)**. However, treatment with HPCD was protective against FAC-potentiated apoptosis **(Figure 7A)**. Although MCD and HPCD are both reported to remove membrane cholesterol, it is likely that the MCD dose we used (50 μM) was not sufficient to disrupt cholesterol levels, as removal of cholesterol with MCD requires mM concentrations (32,33). Using lipid raft isolation, we evaluated the changes in TNFR1 isoforms after pharmacological lowering of cellular cholesterol. As expected, TNFR1 short isoform expression was strongly potentiated by FAC in the lipid raft fractions; however, neither U18666A, MCD, nor HPCD altered TNFR1 expression **(Figure 7B)**. Considering that apoptosis was rescued with HPCD despite prominent TNFR1 short isoform expression, our data suggest that altered lipid metabolism rather than TNFR1 isoform expression is the adverse mediator of iron-potentiated apoptosis.

Taken together, our data suggest that iron loading of endothelial cells alters lipid metabolism, which sensitizes cells to apoptotic death by TNFα. Iron loading also induces accumulation of a short isoform of TNFR1, which does not contribute to

increased apoptosis, but may be a marker of the susceptibility of endothelial cells to this new form of iron-dependent cell death.

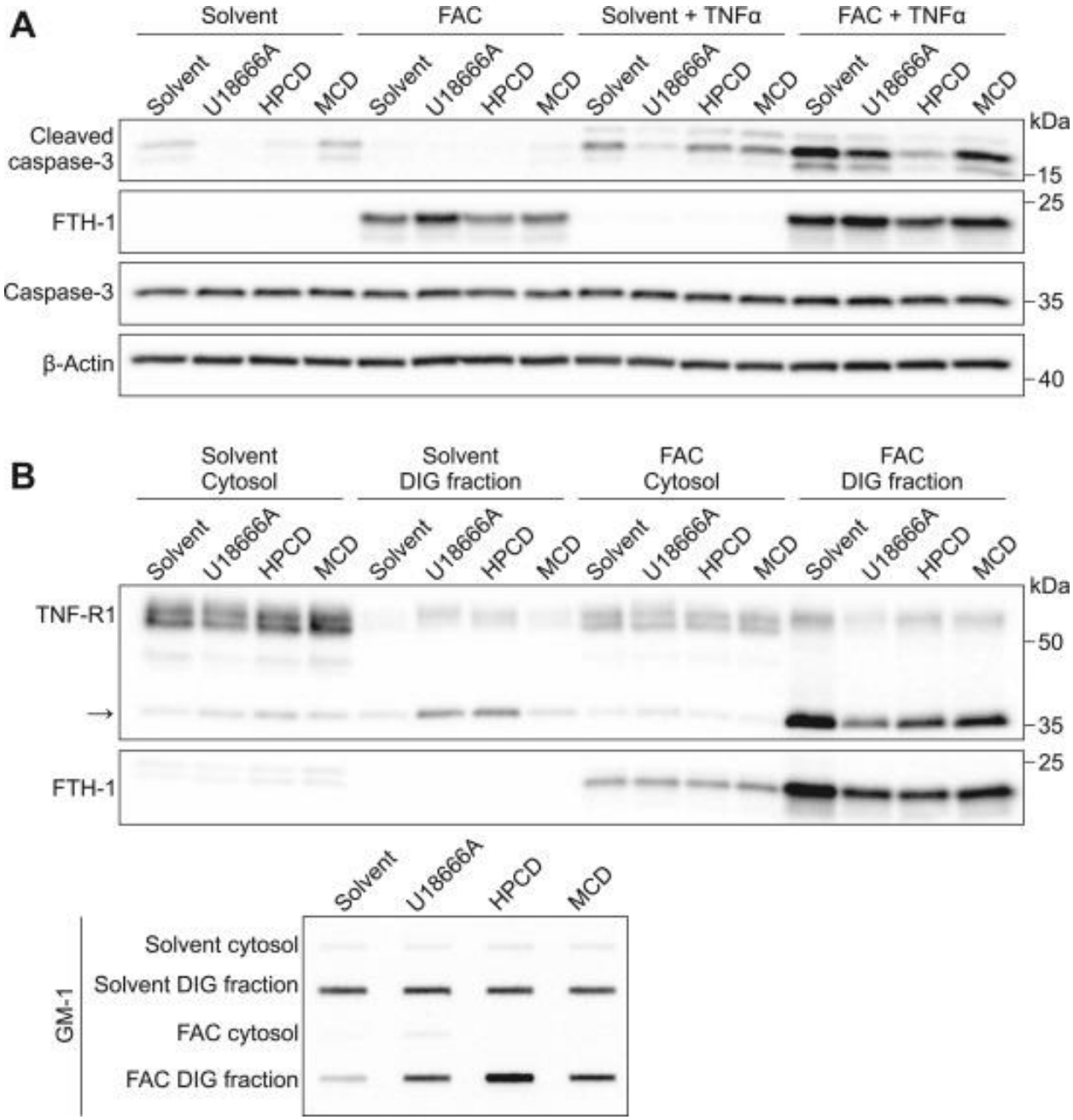

Figure 7. Cholesterol depletion rescues apoptosis of HUVECs induced by excess iron independently of TNFR1 short isoform.

A, HUVECs were treated with solvent (DMSO) or pharmacologically depleted of cholesterol by treating with 1 μM U18666A, 0.3% HPCD, or 50 μM MCD in the presence of 100 μM FAC for 24 h before stimulation with 50 ng/ml TNFα for 16 h. Western blot for

cleaved caspase-3. β-Actin was used as a loading control. *B*, HUVECs were treated with solvent (DMSO), 1 μM U18666A, 0.3% HPCD, or 50 μM MCD in the presence or absence of 100 μM FAC for 40 h. Detergent soluble (cytosol) and insoluble glycosphingolipid (DIG) fractions were isolated by centrifugation. Proteins from equal volume of collected fractions were separated by SDS-PAGE and analyzed by Western blotting. To analyze the distribution of GM-1, each fraction was dot-blotted onto a nitrocellulose membrane and detected using CTx^{HRP}. FAC, ferric ammonium citrate; HPCD, (2-hydroxypropyl)-β-cyclodextrin; HUVECs, human umbilical vein endothelial cells; MCD, methyl-β-cyclodextrin; TNFα, tumor necrosis factor-α.

Discussion

In diseases of iron overload, the iron-binding capacity of transferrin is exceeded, and non-transferrin-bound iron appears in circulation. Utilizing the ZIP14 transporter, the liver rapidly clears NTBI from plasma to store iron in hepatocytes, but with chronic exposure to NTBI, the liver becomes iron-overloaded, resulting in an increased risk for hepatic fibrosis, cirrhosis, and hepatocellular carcinoma (15). Apart from hepatocytes, several other cell types including cardiomyocytes, pancreatic and pituitary cells can take up NTBI and become iron-overloaded, with consequent organ dysfunction. Before reaching any of those cell types, however, NTBI will first contact endothelial cells, but how iron excess affects endothelial cells has not been explored. We used a primary endothelial cell culture model to mimic the exposure of endothelial cells to NTBI in diseases with systemic iron overload. Using RNA-Seq to determine how endothelial cells respond to iron excess, we first found that iron excess in HUVECs induces cholesterol biosynthesis. Cholesterol has essential functions in mammalian systems and its availability is regulated through homeostatic mechanisms to prevent the pathologic consequences of deficient or excessive cholesterol (34). The SREBPs are transcription factors that have well-defined roles in lipid homeostasis (35). Three SREBP isoforms, SREBP-1a, -1c, and -2, have been identified in mammals. SREBP-1a controls both cholesterol and fatty acid biosynthetic pathways by potently activating all SREBP-responsive genes. SREBP1c preferentially regulates transcription of genes involved in fatty acid synthesis (36), whereas SREBP2 preferentially activates genes involved in cholesterol synthesis (37), although a moderate induction in genes involved in fatty acid synthesis also occurs (38). In our study, we found that iron loading induced

mRNA expression of *SREBP1a, c* and *SREBP2,* their gene targets, as well as synthesis of palmitoleic acid and cholesterol, indicating a broader role of iron in modulating lipid homeostasis.

The interaction between iron and cholesterol is not well understood, but increasing evidence associates high iron status with altered cholesterol metabolism, although the data are occasionally conflicting. An early study in rats correlated hepatic iron content with circulating cholesterol levels, although hepatic iron retention was induced by dietary copper deficiency rather than dietary iron loading (39). A more direct comparison was made in dietary iron-loaded rats, where hepatic iron loading correlated with circulating cholesterol, but reduced expression of genes involved in sterol synthesis (40). In contrast, in mice with dietary iron overload, hepatic iron content positively correlated with hepatic cholesterol content but not circulating cholesterol levels, and positively correlated with genes involved in cholesterol biosynthesis (41). Similarly, dietary iron and iron-dextran loaded mice had increased mRNA and enzyme activity of stearoyl-CoA desaturase-1, an enzyme involved in fatty acid metabolism (42). In agreement, we also detected changes in lipid homeostasis in mouse livers after iron perturbation. We had access to microarray data from a published cohort of transferrin receptor 2 (TFR2)-mutant mice susceptible to spontaneous iron overload. The mice were iron-depleted (using iron-deficient diet in combination with phlebotomy) and refed for 1 or 21 days with an iron-sufficient diet (43). Microarray analysis of the liver mRNA showed an increase in cholesterol and fatty acid biosynthesis genes with iron-repletion. Specifically, the microarray MOE 430 2.0 array (Affymetrix) included 25915 unique genes, of which 2254 were annotated as belonging to a biochemical pathway. Out of the annotated pathway

genes, 44 increased robustly with iron refeeding, and of those 8 belonged to the cholesterol synthesis pathway ($p<0.000001$). Further studies in iron-loaded mouse models that utilize cell sorting or single-cell RNA-Seq are needed to determine which cell types increase cholesterol biosynthesis in vivo. In our in vitro study, we saw a strong induction of cholesterol biosynthesis genes by iron loading in HUVECs, but not in the hepatic cell line Hep3B, suggesting that endothelial cells rather than hepatocytes may be responsible for the changes observed in rodent models.

Importantly, we showed that iron interacts with the TNFα pathway. Iron excess worsened TNF□-induced apoptosis, as evidenced by increased levels of cleaved caspase-3. Iron loading further affected the TNFα pathway by inducing novel proteolytic processing of TNFR1 to promote accumulation of a shorter TNFR1 isoform in lipid rafts. In agreement, aberrations in cholesterol-rich lipid rafts are shown to promote apoptosis through TNFR1 (29). Similar to the adverse effects of iron and TNFα co-treatment of HUVECs, we noted increased cleaved caspase-3 after co-treatment of HUVECs with cholesterol and TNFα. Examining the interaction of cholesterol and iron excess in HUVECs, we determined that cholesterol depletion was sufficient to rescue iron-potentiated apoptosis, but this occurred even in the presence of the shorter TNFR1 isoform. Interestingly, Hep3Bs and teloHAECs did not show altered susceptibility to apoptosis or cholesterol homeostasis with FAC loading but did demonstrate conservation of the TNFR1 processing mechanism. We speculate that susceptibility to iron-potentiated apoptosis requires both induction of cholesterol biosynthesis and alterations in the TNFR1 pathway manifested as processing of the short TNFR1 isoform, with endothelial cells being particularly sensitive to iron excess. We propose

that the presence of the shorter TNFR1 isoform may act as a biomarker of the risk of iron-potentiated cell death. Although there is a large body of evidence demonstrating that disease susceptibility and response to infection worsens with elevated iron stores (44-46), any interaction between iron and cytokine-driven apoptosis has not previously been reported. Future studies are needed to determine the contribution of iron loading to endothelial apoptosis in inflammatory conditions in vivo, particularly those characterized by increased TNFα.

In this study, we demonstrate how NTBI accumulation affects cultured endothelial cells. Iron loading induces cholesterol biosynthesis, promotes novel TNFR1 proteolytic processing, and sensitizes cells to TNFα-mediated apoptosis. We determined that during iron excess, the contribution of altered cholesterol homeostasis is the driving pathogenic mediator of apoptosis. Our findings have important implications for iron loading conditions, especially when inflammation is present. Altered cholesterol metabolism by iron excess in endothelial cells may contribute to iron-mediated toxicity in human iron overload disorders.

Materials & methods

Cell culture

Primary human umbilical vein endothelial cells (HUVECs) pooled from 10 donors were obtained from the American Type Culture Collection (ATCC #PCS-100-013). HUVECs were cultured in complete endothelial cell growth media (Cell Applications #211-500) at 37°C in a 5% CO_2 95% air atmosphere. For experiments, HUVECs were plated on collagen and experiments were performed from passages 3-6.

Reagents

Unless otherwise specified, all chemicals were obtained from Sigma-Aldrich. For iron loading studies, HUVECs were treated with 100 μM ferric ammonium citrate (FAC, MP biomedicals #158040), 100 μM ferrous ammonium sulfate (F-1543), 100 μM ferric chloride (#157740), 2 mg/ml apoferritin (#A-3641), 2 mg/ml holoferritin (#F-4503), 100 μM cupric chloride (#C-6917), or 100 μM zinc sulfate (Fisher #Z-58) for the indicated times.

Cholesterol-methylβcyclodextrin complexes were prepared as follows: a 5% w/v solution of methyl-β-cyclodextrin (#C4555) was prepared in water by heating to 70°C and 10 mg/ml cholesterol (#C8667) in 100% ethanol was added dropwise. Cholesterol-MβCD was stirred until the solution was clear, solvent was evaporated overnight by speed-vac, and cholesterol-MβCD was reconstituted in milliQ water to 2.5 mM, filtered, and stored at 4°C. HUVECs were treated with 0-50 μM cholesterol-MβCD for 40 h. For cholesterol depletion studies, HUVECs were treated with 1 μM U18666A (Cayman Chemicals #10009085), 0.3% 2-hydroxypropyl-beta-cyclodextrin (#H107), or 50 μM

methylβcyclodextrin for the indicated times. For inflammation studies, HUVECs were treated with 50 ng/ml recombinant human TNFα (Biolegend #570104) for 6 or 16 h. The optimal time of culture with TNFα was based on preliminary studies testing concentration and time-dependence.

For protease inhibitor experiments, HUVECs were treated with 25 μM TAPI2 (Calbiochem, #579052), 1 μM DAPT (Calbiochem, #565770), or protease inhibitors (from Sigma #INHIB1) 6-aminohexanoic acid (E-ACA, 40 mM), antipain (100 μM), benzamidine HCl (4 mM), aprotinin (1 μM), bestatin (40 μM), chymostatin (100 μM), E-64 (10 μM), EDTA (1 mM), leupeptin (100 μM), pepstatin A (1 μM), phosphoramidon (10 μM), soybean trypsin inhibitor (STI, 5 μM), or protease inhibitor cocktail (PIC, 1:200, Sigma P1860) for 24 h.

The specific time of culture with FAC for cholesterol biosynthesis analysis, apoptosis, and TNFR1 processing was based on preliminary time-course experiments to determine iron loading of HUVECs and their susceptibility to apoptosis (see Figure 4B as an example).

RNA sequencing

RNA sequencing was performed by the UCLA Technology Center for Genomics and Bioinformatics Core Facility. Libraries for RNA-seq were prepared with Kapa Standard kit, and data were sequenced on Illumina HiSeq 3000 for a single-read 50bp run. Data quality check was done on Illumina SAV. Demultiplexing was performed with Illumina Bcl2fastq2 v 2.17 program. Total RNA from primary HUVECs was extracted using a RNeasy Micro kit (Qiagen) following the manufacturer’s instructions. The reads were

mapped to the latest UCSC transcript set using Bowtie2 version 2.1.0[1] and the gene expression level was estimated using RSEM v1.2.15 Trimmed mean of M-values were used to normalize gene expression. Differentially expressed genes were identified using the edgeR program. Expression data were analyzed by comparing control cells treated with solvent (N=3) to cells treated with 100 μM FAC (N=3) for 30 h. Genes identified by RNA sequencing were validated by quantitative real-time PCR.

Gene Expression Quantification by RT-PCR

HUVECs were lysed in TRIzol Reagent (Life Technologies) and total RNA was isolated by chloroform extraction. Five hundred ng of RNA was reverse transcribed using the iScript cDNA Synthesis Kit (Bio-RAD). Quantitative real-time PCR was performed on cDNA using Sso Advance SYBER Green Supermix (Bio-RAD) on the CFX Real-Time PCR Detection System (Bio-RAD). Samples were measured in duplicate and target genes were normalized to *HPRT*. Data are expressed as $2^{-\Delta\Delta Ct}$. Primer sequences are provided in **Table 1**.

Lipid analysis

Lipid compositional analysis was performed by the UCLA Lipidomics Core Facility. For stable isotope labeling, HUVECs were cultured in endothelial cell growth media supplemented with 5 mM [$U^{13}C$]-D-glucose with and without 100 μM FAC for 30 or 40 h to assess the time course of cholesterol synthesis. Analysis of fatty acid and cholesterol synthesis in normal and iron-loaded HUVECs were performed on an Agilent 7890B/5977A GC-MS instrument. Data are presented as nmol synthesis/million cells and was estimated using isotopic spectral analysis.

Oxidized phospholipids were extracted from HUVECs treated with 100 μM FAC for 30 h, to determine whether membrane damage precedes cholesterol synthesis, using a biphasic butanol extraction. Cells were washed in PBS and collected in 1-butanol and transferred to a glass tube. 10% NaCl was added to each tube and centrifuged at 2,000 x g for 10-min at room temperature. The upper organic phase was evaporated under argon gas in a 37°C water bath and contents were solubilized in 150 μL methanol. Sample was centrifuged and clear supernatant was stored at -80°C until analysis. Oxidized phospholipids were measured by LC-MS using an internal oxPAPC standard.

Lipid raft isolation

Lipid rafts were isolated using discontinuous sucrose gradient centrifugation as previously described (47). Two 150 mm dishes of cultured HUVECs were combined for each treatment group. Detergent-insoluble membrane (DIG) fractionation was performed as described (48), using HUVECs cultured on 150 mm dishes. Equal volumes of proteins from each fraction were resolved by SDS-PAGE. To identify the lipid raft and DIG fractions, equal volumes of proteins were dot blotted onto nitrocellulose and probed for ganglioside GM1.

Western Blotting

HUVECs were lysed by mechanical disruption in RIPA lysis buffer with freshly added protease inhibitors (Santa Cruz #SC-24948). Cell lysates were centrifuged at 21,000 x g for 15 min at 4°C and protein concentration was measured by the bicinchoninic acid assay using bovine serum albumin as a standard. Proteins (20 μg/lane) were separated by SDS-PAGE and transferred to nitrocellulose membranes. Membranes were blocked

for 1 hr in 5% w/v dried nonfat milk or bovine serum albumin in TBS with 0.1% Tween-20 and incubated with primary antibodies in blocking buffer overnight at 4°C: cleaved caspase 3 (rabbit, 1:2,000, Cell Signaling Technology #9664), total caspase 3 (rabbit, 1:5,000, Cell Signaling Technology #9662), ferritin light chain (goat, 1:5,000, Novus Biologicals #NBP1-06986), ferritin heavy chain 1 (rabbit, 1:25,000, Cell Signaling Technology #4393), TNFR1 (rabbit, 1:5,000, Cell Signaling Technology #3736), Cholera Toxin B subunit peroxidase conjugate (1:10,000, Sigma #C3741) and β-Actin-peroxidase (1:50,000, Sigma A3854). The secondary reaction was performed using HRP-conjugated anti-rabbit or anti-goat IgG diluted 1:5,000 in blocking buffer. Protein blots were visualized by chemiluminescence using the ChemiDoc XRS+ imaging system and quantified using Image Lab software (Bio-RAD).

Filipin staining

Filipin staining was performed using a cholesterol cell-based assay kit following the manufacturer's instructions (Cayman Chemicals 10009779). Sytox green was used as a nuclear counterstain. Images were captured using a Zeiss LSM700 confocal microscope.

Lentivirus generation

Hek293t cells were grown to 70% confluence in 150 mm poly-D-lysine coated plates in 10% FCS with antibiotics. Hek293t cells were transfected with 2 μg c-terminal V5-tagged TNFR1 pLX304 (DNasu #HsCD00438626), 5 μg pMD2.G (Addgene #12259), 7.5 μg pMDLg/pRRE (Addgene #12251), and 7.5 μg pRSV-REV (Addgene #12253) using lipofectamine 2000 (ThermoFisher) for 16 h. Supernatant was replaced with fresh

DMEM with 10% FCS. Viral supernatant was harvested after 24 and 48 h, pooled, and centrifuged at 300 x g for 5 min to pellet cells. Supernatant was filtered through a 0.45 µM low protein binding filter and stored at 4°C until plasmid digestion. To digest plasmid DNA, supernatant was treated with DNase-1 (Sigma D4527, 10 U per 10 µg of total plasmid DNA) at room temperature for 30 min followed by 4 h at 4°C. Virus was concentrated by ultracentrifugation at 70,000 x g for 2 h at 12°C. Viral pellets resuspended in HBSS were layered on 20% sucrose and centrifuged at 50,000 x g for 2 h at 12°C. Supernatant was snap frozen in liquid nitrogen and stored at -80°C.

For transduction experiments, HUVECs were treated with increasing volume of lentivirus for 10 h prior to incubation with solvent or 100 µM FAC for 24 h. Cell lysates were resolved by SDS-PAGE and probed for the transduced V5-tag.

Statistical Analysis

Data are presented as box and whisker plots, where the box plot indicates the upper 75th and lower 25th percentile, the whiskers indicate the 90th and tenth percentile. Within the box, the solid line indicates the median and the dotted line the mean. Statistical analysis was performed using SigmaPlot version 12.5 (Systat Software). Principal component analysis was performed using R. Statistical differences between groups were determined by one-way ANOVA followed by Holm-Sidak for multiple comparisons for normally distributed values, one-way ANOVA on ranks followed by Dunn's method for multiple comparisons of nonparametric values, two-tailed Student's *t*-test for normally distributed values, or Mann-Whitney *U* test for non-parametric values. Statistical test, number of biological replicates, and *P*-value are indicated in each figure panel. A *P*-value of <0.05 was considered significant.

Data availability

All data are contained within the article and its supporting information. RNA-Seq data have been deposited in NCBI's Gene Expression Omnibus and are accessible through the GEO Series accession number GSE168534 (https://www.ncbi.nlm.nih.gov/geo/query/acc.cgi?acc=GSE168534).

Conflict of interest

T. G. and E. N. are shareholders and scientific advisors of Intrinsic LifeSciences and Silarus Therapeutics, and consultants for Ionis Pharmaceuticals, Protagonist, Disc Medicine, and Vifor. T. G. is a consultant for Akebia. Other authors declare that they have no conflicts of interest with the contents of this article.

Acknowledgments

The authors thank the UCLA Lipidomics core for running the lipid compositional assays; Jeremy Papesh for performing the oxidized phospholipid assays; the UCLA Broad Stem Cell Center Microscopy Core for providing access to and training on confocal microscopes; and Veena Sangkhae for assisting with confocal microscopy.

Author contributions

A. L. F., T. G., and E. N. conceptualization; A. L. F., D. N. S., N. J. P., D. M., S. T. R., T. G., and E. N. formal analysis; A. L. F., D. N. S., and T. G. investigation; A. L. F., D. N. S., D. M., S. T. R., and T. G. methodology; A. L. F. writing–original draft; N. J. P., D. M., S. T. R., T. G., and E. N. writing–review and editing; T. G. and E. N. supervision; E. N. funding acquisition; E. N. project administration.

Funding and additional information

This study was supported by National Center for Advancing Translational Sciences UCLA Clinical and Translational Science Institute grants UL1TR000124, UL1TR001881, and R01HD096863 (to E. N.), NIH Ruth L. Kirschstein National Research Service Awards T32GM065823 and F31HD097931 (to A. L. F.). The content is solely the responsibility of the authors and does not necessarily represent the official views of the National Institutes of Health.

Table 1. List of human primers for qRT-PCR

Gene name	Primer sequences
HPRT	Forward: 5'- GCC CTG GCG TCG TG ATTA GT -3' Reverse: 5'- AGC AAG ACG TTC AGT CCT GTC -3'
SREBP2	Forward: 5'- AGG AGA ACA TGG TGC TGA -3' Reverse: 5'- TAA AGG AGA GGC ACA GGA -3'
MVD	Forward: 5'- ATC AAG TAC TGG GGC AAG CG -3' Reverse: 5'- TTC AGC CAA ATC CGG TCC TC -3'
LDLR	Forward: 5'- GGG CTC TGT CCA TTG TCC TC -3' Reverse: 5'- ACC ATC TGT CTC GAG GGG TAG -3'
HMGCR	Forward: 5'- TTC GGT GGC CTC TAG TGA GAT -3' Reverse: 5'- GTC ACT GCT CAA AAC ATC CTC TTC -3'
TFRC	Forward: 5'- AGT TGA ACA AAG TGG CAC GAG -3' Reverse: 5'- AGC AGT TGG CTG TTG TAC CTC -3'
TNFRSF1A	Forward: 5'- CGC TAC CAA CGG TGG AAG TC -3' Reverse: 5'- CAA GCT CCC CCT CTT TTT CAG -3'
SREBP1a	Forward: 5'- TGC TGA CCG ACA TCG AAG AC -3' Reverse: 5'- CCA GCA TAG GGT GGG TCA AA -3'
SREBP1c	Forward: 5'- CCA TGG ATT GCA CTT TCG AA -3' Reverse: 5'- CCA GCA TAG GGT GGG TCA AA -3'
ACCA	Forward: 5'- CTG TAG AAA CCC GGA CAG TAG AAC -3' Reverse: 5'- GGT CAG CAT ACA TCT CCA TGT G -3'
FASN	Forward: 5'- TCG TGG GCT ACA GCA TGG T -3' Reverse: 5'- GCC CTC TGA AGT CGA AGA AGA A -3'

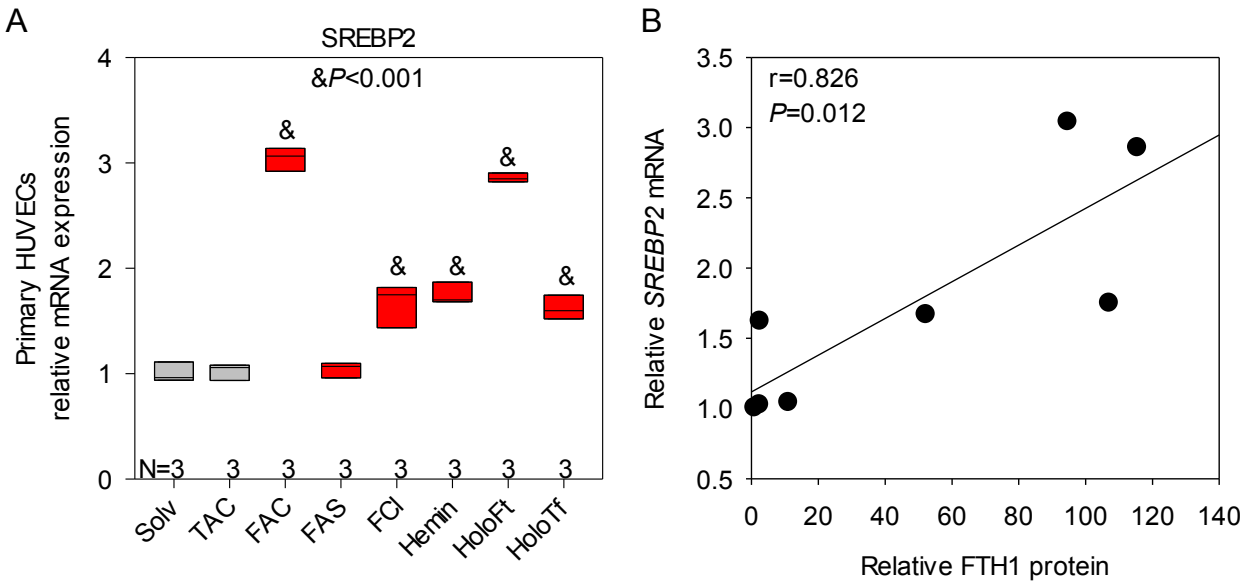

Supplemental Figure 1. Cellular iron loading induces SREBP2 mRNA expression. Primary HUVECs were treated with solvent (water) or triammonium citrate (TAC, 100 μM) (grey) or different forms of iron (red) including ferric ammonium citrate (FAC, 100 μM), ferric ammonium sulfate (FAS, 100 μM), ferric chloride (FCl, 100 μM), hemin chloride (20 μM), holo-ferritin (Ft, 2 mg/ml) or holo-transferrin (Tf, 100 μM) for 40 h. N=3 biological replicates per condition. (A) SREBP2 mRNA expression relative to solvent. Data are expressed as $2^{-\Delta\Delta Ct}$. (B) Pearson correlation between SREBP2 mRNA and ferritin heavy chain 1 (FTH1) protein in HUVECs. Statistical differences between groups were determined by one-way ANOVA with Holm-Sidak method for multiple comparisons for normally distributed values (denoted by &).

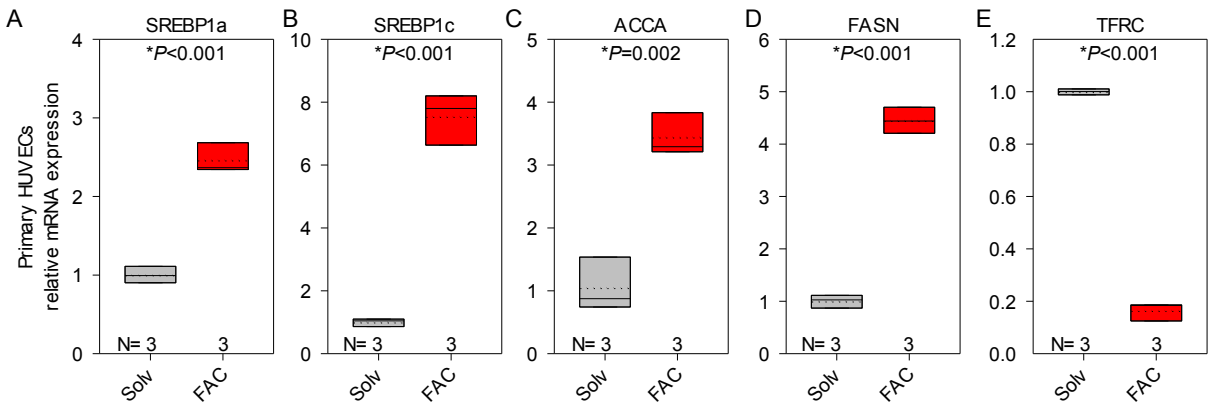

Supplemental Figure 2. Iron induces SREBP-1 target genes in HUVECs.

Primary HUVECs were treated with solvent (water, grey) or 100 μM ferric ammonium citrate (FAC, red) for 40 h. (A-E) qPCR analysis of fatty acid biosynthesis genes SREBP1a, SREBP1c, ACCA, FASN, and iron importer TFRC. Data are expressed as $2^{-\Delta\Delta Ct}$. Number of biological replicates are indicated above the x-axis. Statistical differences between groups were determined by Student's t-test for normally distributed values (denoted by *).

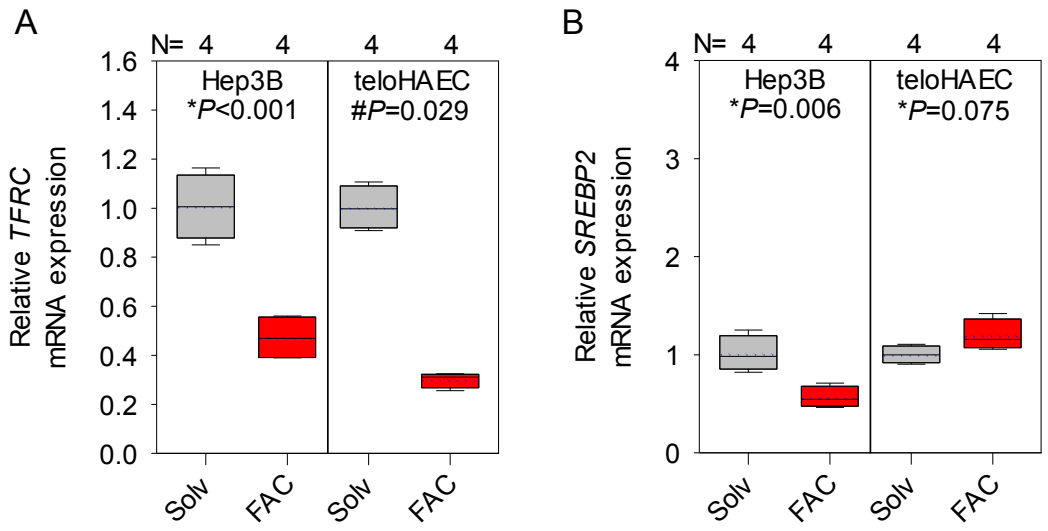

Supplemental Figure 3. Cell panel for induction of SREBP2 by iron loading.

Human hepatic cell line Hep3B and immortalized endothelial cells teloHAEC were treated with solvent (water, grey) or 100 µM FAC (red) for 40 h. (A) TFRC and (B) SREBP2 mRNA expression was determined by qRT-PCR and data are shown as $2^{-\Delta\Delta Ct}$. Number of replicates are indicated above the x-axis. Statistical differences between groups were determined by Student's t-test for normally distributed values (denoted by *) or Mann-Whitney U for non-normally distributed values (denoted by #).

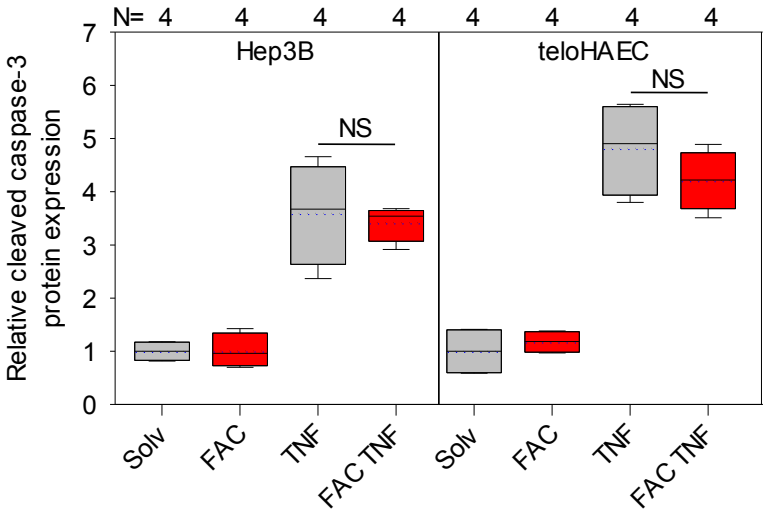

Supplemental Figure 4. Cell panel for potentiation of TNFα-induced apoptosis by iron loading.

Human cell lines Hep3B and immortalized endothelial teloHAECs were treated with solvent (water, grey) or 100 μM FAC (red) for 24 h following stimulation with 50 ng/ml TNFα for 16 h in normal or FAC-supplemented media. Cleaved caspase-3 protein expression was determined by Western blotting and normalized to β-actin. Number of replicates are indicated above the x-axis. Statistical differences between groups were determined by one-way ANOVA.

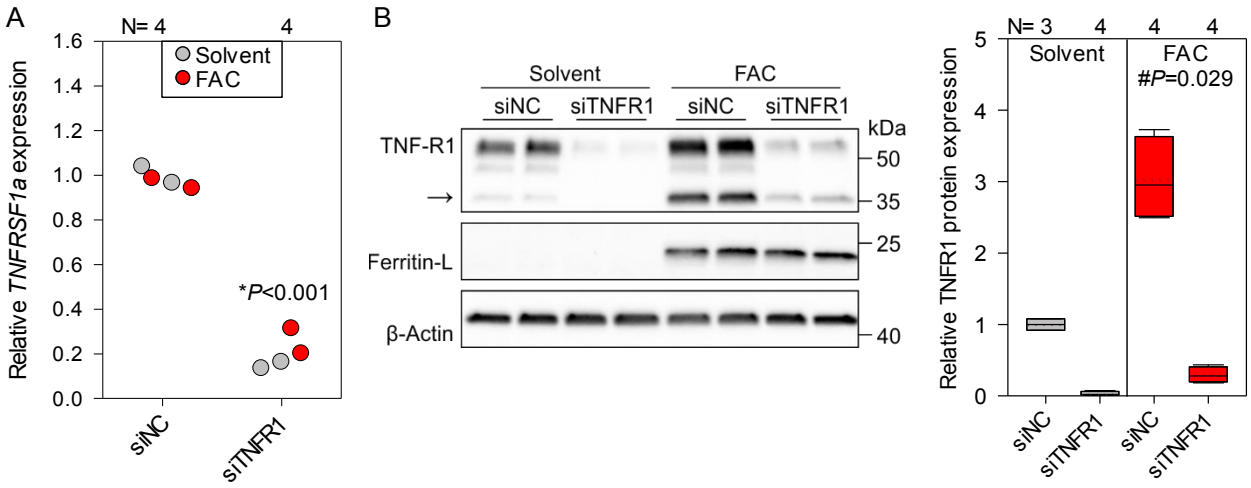

Supplemental Figure 5. Validation of TNFR1 antibody in HUVECs.

HUVECs were reverse transfected with 12.5 pmol negative control siRNA or siRNA targeting TNFR1 for 48 h and treated with solvent (water, grey) or 100 μM FAC (red) for 24h. (A) TNFRSF1A mRNA expressed as $2^{-\Delta\Delta Ct}$ and (B) TNFR1 protein expression by Western blotting. β-actin was used as a loading control. Representative image from N=4 independent experiments. Number of replicates are indicated above the figure panels. Statistical differences between groups were determined by Student's t-test for normally distributed values (denoted by *) or Mann-Whitney U for non-normally distributed values (denoted by #).

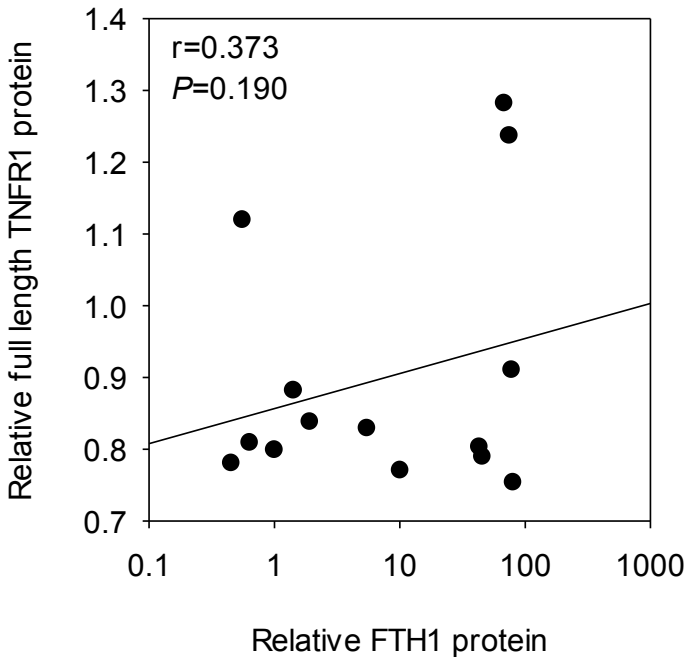

Supplemental Figure 6. Full length TNFR1 does not correlate with cellular iron loading in HUVECs.

HUVECs were treated with solvent (water) or 100 μM FAC, ferric ammonium sulfate (FAS, 100 μM), ferric chloride ($FeCl_3$, 100 μM), apo-ferritin (FT, 2 mg/ml), holo-FT (2 mg/ml), copper chloride ($CuCl_2$, 100 μM), or zinc sulfate ($ZnSO_4$, 100 μM) for 24 h. Pearson correlation between ferritin heavy chain (FTH1) and TNFR1 protein by Western blotting and normalized to β-actin.

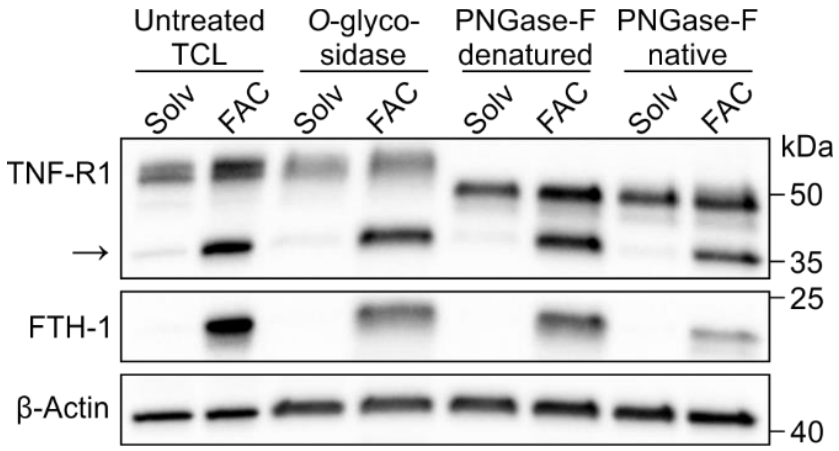

Supplemental Figure 7. TNFR1 glycosylation in HUVECs.

HUVECs were treated with water solvent or 100 μM FAC for 30 h. Western blot for full-length and short TNFR1 isoform (indicated by arrow) of solvent and FAC-treated lysates after incubation with or without *O*-glycosidase or PNGase F. β-actin was used as a loading control.

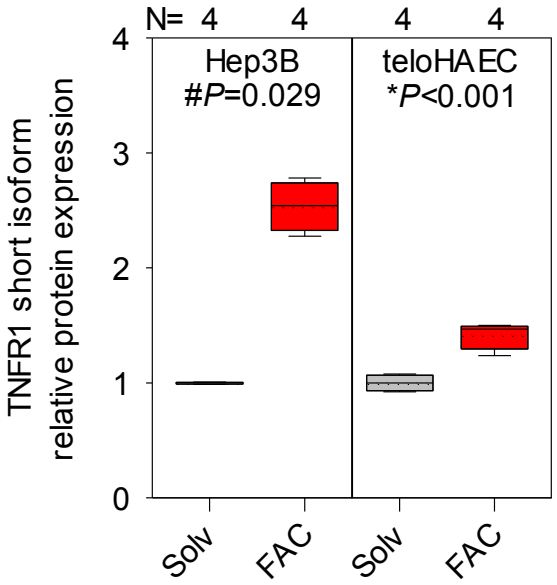

Supplemental Figure 8. Induction of a short isoform of TNFR1 with iron loading in different cell lines.

Human hepatic cell line Hep3B and immortalized endothelial teloHAECs were treated with solvent (water, grey) or 100 μM FAC (red) for 40 h. TNFR1 short isoform protein levels were determined by Western blotting and normalized to β-actin. Number of replicates are indicated above the x-axis. Statistical differences between groups were determined by Student's t-test for normally distributed values (denoted by *) or Mann-Whitney U for non-normally distributed values (denoted by #).

Supplemental materials & methods

Cell culture

HUVECs were cultured in complete endothelial cell growth media (Cell Applications #211-500). Hep3B cells were cultured in DMEM supplemented with 10% FBS. TeloHAECs were cultured in complete MCDB-131 media (VEC Technologies). Cells were cultured at 37°C in a 5% CO2 95% air atmosphere.

Reagents

Unless otherwise specified, all chemicals were obtained from Sigma-Aldrich. For the indicated times, cells were treated with ferric ammonium citrate (FAC, 100 μM), ferrous ammonium sulfate (100 μM), ferric chloride (100 μM), hemin chloride (20 μM, #H-1652), holoferritin (2 mg/ml), holotransferrin (100 μM, Serologicals Corporation #4455-01), or triammonium citrate (100 μM , #A1332) as a control. For inflammation experiments, cells were treated with 50 ng/ml recombinant human TNFα (Biolegend #570104) for the indicated times.

siRNA knockdown of TNFR1

SMARTPool siRNA targeting human TNFR1 (Dharmacon SMARTPool L-005197-00-0005) was used to suppress TNFRSF1A expression. Non-targeting siRNA was used as a control (Dharmacon D-001810-10-05). Reverse transfection was performed using Lipofectamine RNAiMAX (ThermoFisher) in Opti-MEM media following the manufacturer's protocol to yield a final concentration of 12.5 pmol siRNA per well. HUVECs were reverse transfected for 48 h and treated with 100 μM FAC for 24 h.

Knockdown was confirmed by qRT-PCR and immunoblotting.

TNFR1 deglycosylation HUVECs were treated with 100 μM FAC for 30 h. Cell lysates were digested with *O*-glycosidase to cleave *O*-glycans or PNGase F to cleave *N*-linked glycans following the manufacturer's protocol (New England Biolabs #E0540S). *N*-linked deglycoslyation was performed under denaturing and non-denaturing conditions.

References

1. Brissot, P., Ropert, M., Le Lan, C., and Loréal, O. (2012) Non-transferrin bound iron: A key role in iron overload and iron toxicity. *Biochimica et Biophysica Acta (BBA) - General Subjects* **1820**, 403-410

2. Evans, R. W., Rafique, R., Zarea, A., Rapisarda, C., Cammack, R., Evans, P. J., Porter, J. B., and Hider, R. C. (2008) Nature of non-transferrin-bound iron: studies on iron citrate complexes and thalassemic sera. *J Biol Inorg Chem* **13**, 57-74

3. Grootveld, M., Bell, J. D., Halliwell, B., Aruoma, O. I., Bomford, A., and Sadler, P. J. (1989) Non-transferrin-bound iron in plasma or serum from patients with idiopathic hemochromatosis. Characterization by high performance liquid chromatography and nuclear magnetic resonance spectroscopy. *J Biol Chem* **264**, 4417-4422

4. Emerit, J., Beaumont, C., and Trivin, F. (2001) Iron metabolism, free radicals, and oxidative injury. *Biomed Pharmacother* **55**, 333-339

5. Ganz, T. (2018) Iron and infection. *Int J Hematol* **107**, 7-15

6. Nemeth, E., Tuttle, M. S., Powelson, J., Vaughn, M. B., Donovan, A., Ward, D. M., Ganz, T., and Kaplan, J. (2004) Hepcidin Regulates Cellular Iron Efflux by Binding to Ferroportin and Inducing Its Internalization. *Science* **306**, 2090-2093

7. Kishimoto, M., Endo, H., Hagiwara, S., Miwa, A., and Noda, M. (2010) Immunohistochemical findings in the pancreatic islets of a patient with transfusional iron overload and diabetes: case report. *J Med Invest* **57**, 345-349

8. Lu, J. P., and Hayashi, K. (1994) Selective iron deposition in pancreatic islet B cells of transfusional iron-overloaded autopsy cases. *Pathol Int* **44**, 194-199

9. Simcox, J. A., and McClain, D. A. (2013) Iron and diabetes risk. *Cell Metab* **17**, 329-341

10. Ford, E. S., and Cogswell, M. E. (1999) Diabetes and serum ferritin concentration among U.S. adults. *Diabetes Care* **22**, 1978-1983

11. MacDonald, G. A., Bridle, K. R., Ward, P. J., Walker, N. I., Houglum, K., George, D. K., Smith, J. L., Powell, L. W., Crawford, D. H., and Ramm, G. A. (2001) Lipid peroxidation in hepatic steatosis in humans is associated with hepatic fibrosis and occurs predominately in acinar zone 3. *J Gastroenterol Hepatol* **16**, 599-606

12. Fujita, N., Miyachi, H., Tanaka, H., Takeo, M., Nakagawa, N., Kobayashi, Y., Iwasa, M., Watanabe, S., and Takei, Y. (2009) Iron overload is associated with hepatic oxidative damage to DNA in nonalcoholic steatohepatitis. *Cancer Epidemiol Biomarkers Prev* **18**, 424-432

13. Minamiyama, Y., Takemura, S., Kodai, S., Shinkawa, H., Tsukioka, T., Ichikawa, H., Naito, Y., Yoshikawa, T., and Okada, S. (2010) Iron restriction improves type 2 diabetes mellitus in Otsuka Long-Evans Tokushima fatty rats. *Am J Physiol Endocrinol Metab* **298**, E1140-1149

14. Chua, A. C., Drake, S. F., Herbison, C. E., Olynyk, J. K., Leedman, P. J., and Trinder, D. (2006) Limited iron export by hepatocytes contributes to hepatic iron-loading in the Hfe knockout mouse. *J Hepatol* **44**, 176-182

15. Kew, M. C. (2014) Hepatic iron overload and hepatocellular carcinoma. *Liver Cancer* **3**, 31-40

16. Wang, C. Y., and Knutson, M. D. (2013) Hepatocyte divalent metal-ion transporter-1 is dispensable for hepatic iron accumulation and non-transferrin-bound iron uptake in mice. *Hepatology* **58**, 788-798

17. Swaminathan, S., Fonseca, V. A., Alam, M. G., and Shah, S. V. (2007) The Role of Iron in Diabetes and Its Complications. *Diabetes Care* **30**, 1926

18. Gujja, P., Rosing, D. R., Tripodi, D. J., and Shizukuda, Y. (2010) Iron overload cardiomyopathy: better understanding of an increasing disorder. *J Am Coll Cardiol* **56**, 1001-1012

19. Knutson, M. D. (2019) Non-transferrin-bound iron transporters. *Free Radical Biology and Medicine* **133**, 101-111

20. Jenkitkasemwong, S., Wang, C. Y., Coffey, R., Zhang, W., Chan, A., Biel, T., Kim, J. S., Hojyo, S., Fukada, T., and Knutson, M. D. (2015) SLC39A14 is required for the development of hepatocellular iron overload in murine models of hereditary hemochromatosis. *Cell Metab* **22**, 138-150

21. Liuzzi, J. P., Aydemir, F., Nam, H., Knutson, M. D., and Cousins, R. J. (2006) Zip14 (Slc39a14) mediates non-transferrin-bound iron uptake into cells. *Proc Natl Acad Sci U S A* **103**, 13612-13617

22. Canali, S., Wang, C. Y., Zumbrennen-Bullough, K. B., Bayer, A., and Babitt, J. L. (2017) Bone morphogenetic protein 2 controls iron homeostasis in mice independent of Bmp6. *Am J Hematol* **92**, 1204-1213

23. Canali, S., Zumbrennen-Bullough, K. B., Core, A. B., Wang, C. Y., Nairz, M., Bouley, R., Swirski, F. K., and Babitt, J. L. (2017) Endothelial cells produce bone morphogenetic protein 6 required for iron homeostasis in mice. *Blood* **129**, 405-414

24. Wolf, B. B., Schuler, M., Echeverri, F., and Green, D. R. (1999) Caspase-3 Is the Primary Activator of Apoptotic DNA Fragmentation via DNA Fragmentation Factor-45/Inhibitor of Caspase-activated DNase Inactivation. *Journal of Biological Chemistry* **274**, 30651-30656

25. Porter, A. G., and Janicke, R. U. (1999) Emerging roles of caspase-3 in apoptosis. *Cell Death Differ* **6**, 99-104

26. Tartaglia, L. A., Ayres, T. M., Wong, G. H., and Goeddel, D. V. (1993) A novel domain within the 55 kd TNF receptor signals cell death. *Cell* **74**, 845-853

27. Reddy, P., Slack, J. L., Davis, R., Cerretti, D. P., Kozlosky, C. J., Blanton, R. A., Shows, D., Peschon, J. J., and Black, R. A. (2000) Functional analysis of the domain structure of tumor necrosis factor-alpha converting enzyme. *J Biol Chem* **275**, 14608-14614

28. Mullberg, J., Durie, F. H., Otten-Evans, C., Alderson, M. R., Rose-John, S., Cosman, D., Black, R. A., and Mohler, K. M. (1995) A metalloprotease inhibitor blocks shedding of the IL-6 receptor and the p60 TNF receptor. *J Immunol* **155**, 5198-5205

29. Legler, D. F., Micheau, O., Doucey, M. A., Tschopp, J., and Bron, C. (2003) Recruitment of TNF receptor 1 to lipid rafts is essential for TNFalpha-mediated NF-kappaB activation. *Immunity* **18**, 655-664

30. Engelmann, H., Aderka, D., Rubinstein, M., Rotman, D., and Wallach, D. (1989) A tumor necrosis factor-binding protein purified to homogeneity from human urine protects cells from tumor necrosis factor toxicity. *Journal of Biological Chemistry* **264**, 11974-11980

31. Chhibber-Goel, J., Coleman-Vaughan, C., Agrawal, V., Sawhney, N., Hickey, E., Powell, J. C., and McCarthy, J. V. (2016) γ-Secretase Activity Is Required for Regulated Intramembrane Proteolysis of Tumor Necrosis Factor (TNF) Receptor 1 and TNF-mediated Pro-apoptotic Signaling. *Journal of Biological Chemistry* **291**, 5971-5985

32. Resnik, N., Repnik, U., Kreft, M. E., Sepčić, K., Maček, P., Turk, B., and Veranič, P. (2015) Highly Selective Anti-Cancer Activity of Cholesterol-Interacting Agents Methyl-β-Cyclodextrin and Ostreolysin A/Pleurotolysin B Protein Complex on Urothelial Cancer Cells. *PLOS ONE* **10**, e0137878

33. Barman, S., and Nayak, D. P. (2007) Lipid raft disruption by cholesterol depletion enhances influenza A virus budding from MDCK cells. *J Virol* **81**, 12169-12178

34. Tabas, I. (2002) Consequences of cellular cholesterol accumulation: basic concepts and physiological implications. *The Journal of clinical investigation* **110**, 905-911

35. Horton, J. D., Goldstein, J. L., and Brown, M. S. (2002) SREBPs: activators of the complete program of cholesterol and fatty acid synthesis in the liver. *The Journal of Clinical Investigation* **109**, 1125-1131

36. Shimano, H., Horton, J. D., Shimomura, I., Hammer, R. E., Brown, M. S., and Goldstein, J. L. (1997) Isoform 1c of sterol regulatory element binding protein is less active than isoform 1a in livers of transgenic mice and in cultured cells. *The Journal of Clinical Investigation* **99**, 846-854

37. Horton, J. D., Shimomura, I., Brown, M. S., Hammer, R. E., Goldstein, J. L., and Shimano, H. (1998) Activation of cholesterol synthesis in preference to fatty acid synthesis in liver and adipose tissue of transgenic mice overproducing sterol regulatory element-binding protein-2. *The Journal of Clinical Investigation* **101**, 2331-2339

38. Horton, J. D., Shah, N. A., Warrington, J. A., Anderson, N. N., Park, S. W., Brown, M. S., and Goldstein, J. L. (2003) Combined analysis of oligonucleotide microarray data from transgenic and knockout mice identifies direct SREBP target genes. *Proceedings of the National Academy of Sciences* **100**, 12027

39. Fields, M., and Lewis, C. G. (1999) Cholesterol-lowering nature of unsaturated fat in rats may be due to its inability to increase hepatic iron. *Metabolism* **48**, 200-204

40. Brunet, S., Thibault, L., Delvin, E., Yotov, W., Bendayan, M., and Levy, E. (1999) Dietary iron overload and induced lipid peroxidation are associated with impaired plasma lipid transport and hepatic sterol metabolism in rats. *Hepatology* **29**, 1809-1817

41. Graham, R. M., Chua, A. C. G., Carter, K. W., Delima, R. D., Johnstone, D., Herbison, C. E., Firth, M. J., O'Leary, R., Milward, E. A., Olynyk, J. K., and Trinder, D.

(2010) Hepatic iron loading in mice increases cholesterol biosynthesis. *Hepatology* **52**, 462-471

42. Pigeon, C., Legrand, P., Leroyer, P., Bouriel, M., Turlin, B., Brissot, P., and Loreal, O. (2001) Stearoyl coenzyme A desaturase 1 expression and activity are increased in the liver during iron overload. *Biochim Biophys Acta* **1535**, 275-284

43. Ramos, E., Kautz, L., Rodriguez, R., Hansen, M., Gabayan, V., Ginzburg, Y., Roth, M.-P., Nemeth, E., and Ganz, T. (2011) Evidence for distinct pathways of hepcidin regulation by acute and chronic iron loading in mice. *Hepatology* **53**, 1333-1341

44. Drakesmith, H., and Prentice, A. (2008) Viral infection and iron metabolism. *Nat Rev Microbiol* **6**, 541-552

45. Stefanova, D., Raychev, A., Arezes, J., Ruchala, P., Gabayan, V., Skurnik, M., Dillon, B. J., Horwitz, M. A., Ganz, T., Bulut, Y., and Nemeth, E. (2017) Endogenous hepcidin and its agonist mediate resistance to selected infections by clearing non-transferrin-bound iron. *Blood* **130**, 245-257

46. Arezes, J., Jung, G., Gabayan, V., Valore, E., Ruchala, P., Gulig, P. A., Ganz, T., Nemeth, E., and Bulut, Y. (2015) Hepcidin-induced hypoferremia is a critical host defense mechanism against the siderophilic bacterium Vibrio vulnificus. *Cell Host Microbe* **17**, 47-57

47. Gajate, C., and Mollinedo, F. (2017) Isolation of Lipid Rafts Through Discontinuous Sucrose Gradient Centrifugation and Fas/CD95 Death Receptor Localization in Raft Fractions. in *CD95: Methods and Protocols* (Legembre, P. ed.), Springer New York, New York, NY. pp 125-138

48. LEGLER, D. F., DOUCEY, M.-A., CEROTTINI, J.-C., BRON, C., and LUESCHER, I. F. (2001) Selective inhibition of CTL activation by a dipalmitoyl-phospholipid that prevents the recruitment of signaling molecules to lipid rafts. *The FASEB Journal* **15**, 1601-1603

Concluding Remarks

In this dissertation, we proposed an updated model of the mechanism of action that erythroferrone uses to couple systemic iron availability to erythropoiesis. Using protein modeling algorithms, surface plasmon resonance, molecular biology, and cell-based bioassays, we discovered important molecular features of the human erythroferrone protein that mediate its hepcidin-suppressive function. As part of this discovery, we defined regions of the protein conserved by evolution to promote proper assembly and BMP binding, as well as ones that may play roles in localization and protein complex stability. Understanding these molecular details will be crucial to the development of ERFE-targeted therapeutics. High-burden diseases such as β-thalassemia and chronic kidney disease both implicate dysregulated ERFE in their respective pathophysiologies, albeit in opposite ways. Therefore, the inhibition, enhancement, mimicry, or modulation of erythroferrone activity could have future therapeutic potential. The studies outlined here will provide a base for pre-clinical development.

Classical techniques for the visualization of protein structure often rely on the crystallization, solubilization, and/or other stabilization of the desired protein(s). These requirements present a challenge even under the best of circumstances. The ERFE protein contains both structured and highly unstructured portions, the latter making immobilization very difficult. Activity data contained in this dissertation and elsewhere indicate that the disordered N-terminus of the molecule is the functional region, therefore atomic structure information on the C-terminus alone would be unlikely to provide insights into the mechanism of hepcidin suppression. In this dissertation, we

used AI-assisted protein and complex modeling (AlphaFold2) to help generate testable hypotheses for how the ERFE N-terminus interacts with its BMP ligands.

The computer modeling used here was a powerful tool, for not only the planning of experiments, but also helping to explain established findings. In our study, the value of these models was inexorably linked to our ability to validate their conclusions using experimental data. Future structure-function studies—especially of proteins whose structures cannot be solved—are sure to benefit from careful generation and consideration of AlphaFold or other algorithmic models as well.

Our study of erythroferrone enhanced our understanding of the hormone's molecular mechanism and allowed us to clarify the context in which it operates. The study may also stimulate new investigations into the fundamental biology of C1q/TNFα-related protein family members as well as the translational potential of their manipulation. Transformational gene therapy treatments and even cures for high-burden hematopoietic diseases like β-thalassemia are on the horizon. Even as they reach approval, some patients may not have access to these promising interventions or may not choose such treatments due to their novelty. Patients with anemia of inflammation or other diseases that result in high hepcidin may benefit from ERFE activators or mimetics. The potential to address erythropoietic disorders of multiple types makes further study of ERFE a practical and translatable endeavor. This reality of multiple disease areas and therapeutic needs underscores the continued importance of small molecule and biologics development for these diseases. The information presented in this dissertation will be invaluable to such drug discovery efforts.